Dissertation

Optical Control of Neuronal Signaling with Organic Bioelectronics

submitted by

Tony Schmidt

MSc, BSc

for the Academic Degree of

Doctor of Philosophy (PhD)

at the

Medical University of Graz

Gottfried Schatz Research Center for Cell Signaling, Metabolism and Aging

Division of Biophysics

under the Supervision of

Assoz. Prof. Priv.-Doz. Dipl.-Ing. Dr.techn. Rainer SCHINDL

2022

Statutory Declaration

I, Tony Christian Schmidt, hereby declare that this thesis is my own original work and that I have fully acknowledged by name all of the individuals and organizations that have contributed to the research for this thesis. Due acknowledgement has been made in the text to all other material used. Throughout this thesis and in all related publications I followed the “Guidelines of the Medical University of Graz on Good Scientific Practice“.

Graz, 12.08.2022

Disclosures

Parts of this thesis have been published in:

2022 **Light Stimulation of Neurons on Organic Photocapacitors Induces Action Potentials with Millisecond Precision**
Tony Schmidt[1,2], Marie Jakešová[3,4], Vedran Đerek[4,5], Karin Kornmueller[1,2], Oleksandra Tiapko[1], Helmut Bischof[6,7], Sandra Burgstaller[6,7,8], Linda Waldherr[1], Marta Nowakowska[9], Christian Baumgartner[2,10], Muammer Üçal[2,9], Gerd Leitinger[2,11], Susanne Scheruebel[1], Silke Patz[9], Roland Malli[2,6], Eric Daniel Głowacki[3,4]*, Theresa Rienmüller[2,10]*, Rainer Schindl[1,2]*
ADV MATER TECHNOL-US. 2022; 2101159 Doi: 10.1002/admt.202101159

[1] Gottfried Schatz Research Center, Chair of Biophysics, Medical University of Graz, Neue Stiftingtalstraße 6, 8010 Graz, Austria
[2] BioTechMed-Graz, Graz, Austria
[3] Bioelectronics Materials and Devices Laboratory, Central European Institute of Technology, Brno University of Technology, Purkyňova 123, 61200 Brno, Czech Republic
[4] Laboratory of Organic Electronics, ITN Campus Norrköping, Linköping University, SE-60174, Norrköping, Sweden
[5] Department of Physics, Faculty of Science, University of Zagreb, Bijenička c. 32, 10000 Zagreb, Croatia
[6] Gottfried Schatz Research Center, Molecular Biology and Biochemistry, Medical University of Graz, Neue Stiftingtalstraße 6/6, 8010 Graz, Austria
[7] Department of Pharmacology, Toxicology and Clinical Pharmacy, Institute of Pharmacy, University of Tuebingen, Auf der Morgenstelle 8, 72076 Tuebingen, Germany
[8] NMI Natural and Medical Sciences Institute at the University of Tuebingen, 72770 Reutlingen,
[9] Research Unit of Experimental Neurotraumatology, Department of Neurosurgery, Medical University Graz, Auenbruggerplatz 2.2, 8036, Graz, Austria
[10] Institute of Health Care Engineering with European Testing Center of Medical Devices, Graz University of Technology, Graz, Austria.
[11] Gottfried Schatz Research Center, Division of Cell Biology, Histology and Embryology, Medical University of Graz, Neue Stiftingtalstraße 6, 8010 Graz, Austria

All co-authors have agreed to the inclusion of their published data in the dissertation. The reproduction of illustrations and figures published from own or third-party publications is granted.

Another part of this thesis contains unpublished data. Parts of this original data and figures were reprinted, adapted, or reused by diploma or master students and their work that I have co-supervised during my PhD.

During my PhD, I contributed to the following publications:

2019 **Optoelectronic control of single cells using organic photocapacitors**
Jakešová, M; Silverå Ejneby, M; Đerek, V; Schmidt, T; Gryszel, M; Brask, J; Schindl, R; Simon, DT; Berggren, M; Elinder, F; Głowacki, ED.
SCI ADV. 2019; 5(4): eaav5265-eaav5265. Doi: 10.1126/sciadv.aav5265

2019 **STIM1 and Orai1 regulate Ca2+ microdomains for activation of transcription**
Schober, R; Waldherr, L; Schmidt, T; Graziani, A; Stilianu, C; Legat, L; Groschner, K; Schindl, R.
Biochim Biophys Acta Mol Cell Res. 2019; 1866(7):1079-1091
Doi: 10.1016/j.bbamcr.2018.11.001

2019 **Mechanistic insights into the Orai channel by molecular dynamics simulations**
Bonhenry, D; Schober, R; Schmidt, T; Waldherr, L; Ettrich, RH; Schindl, R.
Semin Cell Dev Biol. 2019; 94(7):50-58 Doi: 10.1016/j.semcdb.2019.01.002

2019 **Sequential activation of STIM1 links Ca2+ with luminal domain unfolding**
Schober, R; Bonhenry, D; Lunz, V; Zhu, J; Krizova, A; Frischauf, I; Fahrner, M; Zhang, M; Waldherr, L; Schmidt, T; Derler, I; Stathopulos, PB; Romanin, C; Ettrich, RH; Schindl, R.
Sci Signal. 2019; 12(608): Doi: 10.1126/scisignal.aax3194

2020 **Luminal STIM1 Mutants that Cause Tubular Aggregate Myopathy Promote Autophagic Processes**
Sallinger, M; Tiffner, A; Schmidt, T; Bonhenry, D; Waldherr, L; Frischauf, I; Lunz, V; Derler, I; Schober, R; Schindl, R.
INT J MOL SCI. 2020; 21(12): 4410 Doi: 10.3390/ijms21124410

2020 **Blockage of Store-Operated Ca2+ Influx by Synta66 is Mediated by Direct Inhibition of the Ca2+ Selective Orai1 Pore**
Waldherr, L; Tiffner, A; Mishra, D; Sallinger, M; Schober, R; Frischauf, I; Schmidt, T; Handl, V; Sagmeister, P; Köckinger, M; Derler, I; Üçal, M; Bonhenry, D; Patz, S; Schindl, R.
Cancers (Basel). 2020; 12(10): Doi: 10.3390/cancers12102876

2021 **Potassium ions promote hexokinase-II dependent glycolysis**
Bischof, H; Burgstaller, S; Springer, A; Matt, L; Rauter, T; Bachkönig, OA; Schmidt, T; Groschner, K; Schindl, R; Madl, T; Plesnila, N; Lukowski, R; Graier, WF; Malli, R.
iScience. 2021; 24(4): 102346-102346. Doi: 10.1016/j.isci.2021.102346

2021 **Immobilization of Recombinant Fluorescent Biosensors Permits Imaging of Extracellular Ion Signals**
Burgstaller, S; Bischof, H; Rauter, T; Schmidt, T; Schindl, R; Patz, S; Groschup, B; Filser, S; van, den, Boom, L; Sasse, P; Lukowski, R; Plesnila, N; Graier, WF; Malli, R.
ACS Sens. 2021; 6(11):3994-4000 Doi: 10.1021/acssensors.1c01369

2021 **Targeted Chemotherapy of Glioblastoma Spheroids with an Iontronic Pump**
Waldherr, L; Seitanidou, M; Jakesova, M; Handl, V; Honeder, S; Nowakowska, M; Tomin, T; Rad, MK; Schmidt, T; Distl, J; Birner-Gruenberger, R; Campe, G; Schafer, U; Berggren, M; Rinner, B; Asslaber, M; Ghaffari-Tabrizi-Wizsy, N; Patz, S; Simon, DT; Schindl, R.
ADV MATER TECHNOL-US. 2021; 2001302 Doi: 10.1002/admt.202001302

Acknowledgements

My special thanks go to Rainer Schindl: “You have been much more than a good PI during my PhD; you are a great mentor and probably the nicest person in academia. One of my best decisions was to start working with you when you were starting a lab in Graz. I am thankful for the extraordinary working group and atmosphere that you have created, for every scientific and personal discussion, for your endless support, for all the fun we had and for all the things I could learn from you.”

Without the following collaboration partners and colleagues, this thesis would not have been possible. Special thanks to Eric Daniel Głowacki, Vedran Đerek, Marie Jakešová, Ludovico Migliaccio, and Aleksandar Opančar for the photocap idea, the prototyping, testing, improving, production and for teaching me various concepts related to material science. I enjoyed every meeting that we had and especially every drink. “Thanks Eric that I could have been part of this wonderful story!” I also want to thank Professor Wolfgang Heiß and Mykhailo Sytnyk providing the epindolidione microstructured pigments.

I also want to thank my dissertation committee members and co-supervisors Professor Wolfgang Schreibmayer and Silke Patz that supported my work with valuable ideas! “Silke, I really enjoyed the little stop overs and conversations when I was picking up cells at the ZMF!”

A special thanks also goes to Helmut Bischof and Sandra Burgstaller for our conversations and your impact on the idea to test potassium channels. “You both are truly two great personalities and you brought so much fun to work and extracurricular activities!”

Many people had a direct impact on this work. Therefore, I want to thank the whole LOGOS-TBI team and especially Theresa Rienmüller, Karin Kornmüller, Muammer Üçal and Marta Nowakowska. A very special thanks goes also to the members of my working group for your help and for our discussions to Linda Waldherr, Sabine Erschen, Verena Handl, and Astrid Gorischek which made life in lab so much fun. “Thanks, Linda, for being such a great ‘Doktoratsschwester’, we both definitely rock every conference!”I also want to thank all diploma and master students for their help, especially Clemens Stilianu. A big thanks also goes to Oleksandra Tiapko that teached me a lot about neurons.

The Gottfried Schatz Research Center and especially the Biophysics Department is a great place for scientific growth and making new friend. I thank Professor Klaus Groschner and Professor Ruth Prassl for being my inofficial mentors! I am also thankful to Robert Arnold, Sanja Curcic, Kurt Feichtinger, Hazel Erkan, Annarita Graziani, Denis Krivic, Roland Lohr, Niroj Shrestha and to the biophysics people

from Linz! Particularly I want to thank Astrid Grundner, Jasmin Maderer, Gebhard Schratter, Patrick Wiedner and Johann Krebs. “We spent together so much time in work and outside university, I am so glad that I met such wonderful persons!”

As a PhD student I received funding by the Medical University of Graz through the PhD program Molecular Medicine (MOLMED) and from the Austrian Science Fund (FWF project number P32778, P28701 and TAI 245 to Rainer Schindl and FWF project number ZK17 to the LOGOS-TBI). Some Figures were partly generated using Servier Medical Art, provided by Servier, licensed under a Creative Commons Attribution 3.0.

Mein größter Dank geht an meine Eltern Thea und Walter, sowie an meine Schwestern Isabelle und Stephanie. Ich bin euch für so vieles dankbar und ich bin so unendlich glücklich, dass ihr meine Familie seid!

Table of Contents

Kurzzusammenfassung

Lichtgesteuerte Kontrolle von neuronalen Informationen mit Hilfe organischer Bioelektroniken

Neurologische Störungen oder Verletzungen nach Trauma induzierenden Unfällen können oft die natürliche Fähigkeit von Neuronen zerstören Informationen zu verarbeiten oder weiterzuleiten. Die nicht natürliche Verknüpfung zwischen Technologie und Lebewesen kann diese Defizite behandeln und überwachen oder auch die ursprüngliche Funktion wiederherstellen. Alle bioelektronischen Geräte müssen sich zwei Hauptherausforderungen stellen: Die Biokompatibilität zu lebendem Gewebe und die Stromversorgung des Gerätes selbst. In dieser Arbeit stelle ich zwei neue Ansätze vor, die auf lichtempfindlichen organischen Pigmenten basieren, die keine kabelgebundene Energieversorgung oder genetische Modifikation erfordern, um Zellen zu stimulieren oder zu steuern und die sicher in Bezug auf die Verwendung mit lebenden Zellen sind.

Im Rahmen dieser Arbeit habe ich die Wechselwirkung von neuronalen Zellmembranen mit kolloidalen Makrokristallen aus Epindolidione-Pigmenten untersucht, die eine 3D Mikrostruktur auf ihrer Oberfläche aufweisen. Neuronen zeigten, dass sie ausgedehnte Netzwerke entwickeln und stabile Interaktionen mit diesen Strukturen erzeugen. Es wurde auch festgestellt, dass Neuriten in Richtung der organischen Pigmente wuchsen und adhärierten, oder während des Zellwachstums diese Verbindungen umbauten. Die photothermokapazitive Stimulation dieses Komplexes aus Neuronen und Pigmenten depolarisierte mit Hilfe eines Lasers die Zellmembran. Jedoch waren die Pigmentkristalle nicht in der Lage Aktionspotentiale zu induzieren.

Weiterhin wurden in dieser Arbeit neuartige Halbleiter getestet, die auf organischen Pigmenten basieren und in einer Elektrolytlösung wie ein Kondensator zur lichtgesteuerten und photokapazitiven Stimulierung von Säugetierzellen funktionieren. Diese können mit sichtbarem rotem Licht angeregt werden, welches in der Lage ist durch die Haut ins Gewebe einzudringen. Diese so genannten OEPCs (Organic Electrolytic Photocapacitors) bestehen aus flachen Schichten von halbleitenden Pigmenten. Dafür wurden N,N'-Dimethylperylentetracarbonsäurediimid (PTCDI) und metallfreies Phthalocyanin (H_2Pc) verwendet. Humane embryonale Nierenzellen (HEK) wurden mit dem spannungsgesteuerten Kaliumkanal $K_v1.3$ transfiziert. Elektrophysiologische Messungen zeigten eine zeitabhängige Ionenkanalaktivierung und eine Verschiebung der Kanalleitfähigkeit von etwa 30 mV, wenn die sich auf OEPCs befindlichen Zellen stimuliert wurden. Neuronen, die mit Lichtpulsen im Millisekunden Bereich stimuliert wurden, zeigten, dass wiederholt zuverlässig Aktionspotentiale erzeugt werden konnten, und zwar mit einzelnen oder mit einer Serie von Lichtpulsen.

Die hier vorgestellten Ergebnisse zeigen, dass diese bioelektronische Anwendung, die auf organischen Pigmenten basiert, für weitere *in vitro* Anwendungen sicher sind und dass man ohne genetische Veränderungen neuronalen Signale durch Licht erzeugen kann. Diese Ergebnisse bilden auch die Grundlage um in der Zukunft lichtgesteuert *in vivo* Anwendungen zu entwickeln, die mit hoher Präzision arbeiten.

Abstract

Optical Control of Neuronal Signaling with Organic Bioelectronics

Neurological disorders or injuries after traumatic events often destroy the natural function of neurons to process or transduce information. The artificial connection between technology and the living organism can treat, monitor, or restore such functions and conditions. All bioelectronic devices must address two main challenges: biocompatibility and power supply. In this work, I introduce two novel approaches based on light-sensitive organic pigments that require no wiring or genetic modification to control cell stimulation and that are safe in terms of use with living cells.

In this thesis, I have investigated the interaction of neuronal cell membranes with colloidal macrocrystals made from Epindolidione pigments that feature a 3D-shaped microstructure on their surface. Neurons developed extensive networks and stable interactions with these structures. Neurites that grew toward the organic pigments attached to them and remodeled connections during cell maturation. Photothermocapacitive stimulation of neuron-pigment complexes with laser light depolarized the cell membrane but was unable to induce action potential firing.

I also benchmarked the performance of Organic Electrolytic Photocapacitors (OEPCs) on photocapacitive stimulation of mammalian cells with visible red light that can penetrate through the skin into tissues. OEPCs form a planar photovoltaic device with the n- and p-type semiconducting pigments N,N'-dimethyl perylene tetracarboxylicdiimide (PTCDI) and metal free phthalocyanine (H_2Pc). Electrophysiology recordings of human embryonic kidney (HEK) cells transfected with the voltage-gated potassium channel $K_v1.3$ showed a time-dependent channel activation and a channel conductance shift of around 30 mV when placed on OEPCs. Neurons stimulated with millisecond pulses fired reliably action potentials on single and repetitive light pulses.

The findings demonstrate that organic pigment-based bioelectronics are safe to use *in vitro* and enable a nongenetic manipulation of neuronal signaling with light and high precision for future *in vivo* applications.

1 Introduction

1.1 Motivation

Neuronal signaling is essential for most complex organisms enabling them to develop sophisticated cognitive and behavioral complexity. Signaling pathways range from single cell to tissue levels, organs, or the entire organism. Chemical and electrical signals affect numerous processes directly and indirectly related to neurons or the nervous system [1]. Therefore, scientists of all disciplines and centuries developed ideas and methods to control neuronal signaling by activating or preventing processes related to it.

Chemical stimulation methods often aim to deliver neurotransmitter to the target. Glutamatergic stimulation or silencing has been used successfully to stimulate retinal ganglion cells [2], alter respiratory excitation [3], attenuate chronic pain [4] or alter synapse formation [5]. Other classical neurotransmitters, such as acetylcholine or dopamine, may also play an important role in non-neuro related stimulation mechanisms such as blood pressure control [6] or body temperature regulation [7].

However, the most common method for controlling neuronal signaling is achieved by electrical stimulation, since the cell membrane depolarization with an electric field offers a faster and more targeted stimulus to a tissue than a comparably slower chemical release that features unspecific diffusion [8]. There are three major applications in this field: neuroprosthetics that try to restore lost functions [9-11], devices that facilitate the natural healing process after acute injuries [12-15], or monitoring neuronal activities and the response of excitable tissues [16-19]. Electrical stimulation is not only a mature concept for *in vitro* use, it also provides reliable methods for clinical applications [20] such as in the treatment of Parkinson's disease [21, 22], pain reduction [23], or as signal converters for sensory organs such as cochlear [24-26] or retinal implants [27-29].

Most of these methods require wiring that complicates implantation, provides a high risk of infections [30-32], and causes discomfort for patients [33, 34]. Wireless bioelectronics, however, do not require an external energy source or an internal battery to deliver an electric current to the implant. Piezoelectric stimulation with ultrasound [35] or surface acoustic waves [36] avoids such risks, but mechanical vibrations [37] are introduced, which can result in self-heating [36, 38, 39].

A solution to many of the mentioned problems might be light as a source of energy. The three main light-based approaches are optogenetics [40], photopharmacology [41], and direct photostimulation.

Although the first two come with the catch of genetic modification or the delivery of chemicals, the latter is a more complex concept that describes different methods.

Since all the mentioned approaches to control neuronal signaling have unique problems, one must be very careful when designing them. The goal is to find a method which achieves an artificially introduced stimulation with as little as possible negative impact on neurons. The key criteria for this endeavor are biocompatible and stable devices that are easy to handle and safe to operate. Therefore, I want to introduce two methods for neurostimulation and evaluate them and their potential for *in vitro* use. Depending on their application site, they might be novel and useful tools for future *in vivo* implants capable of ultimately controlling neuronal signaling and related downstream effects in human physiology.

1.2 Optical Control of Neuronal Signaling with Organic Bioelectronics

The concept of bioelectronics is a broad research area covering applications for the treatment of diseases, monitoring physiological conditions or individuals, replacing functions, and many more. Bioelectronics provide an interface between life and technical solutions for a multitude of problems. A straight classification of all aspects is not possible. However, various concepts addressed in this thesis can be broken down into meaningful subunits (Figure 1) and contextualized to explain light-induced stimulation of excitable cells.

Within this thesis, I am exploring the potential of two approaches using different light absorbing devices to control neuronal signaling via neurostimulation. Both are based on organic pigments, which are already available for commercial use, but differ fundamentally in their working principles. First, I will introduce colloidal pigment crystals forming a microstructure that quickly changes temperature

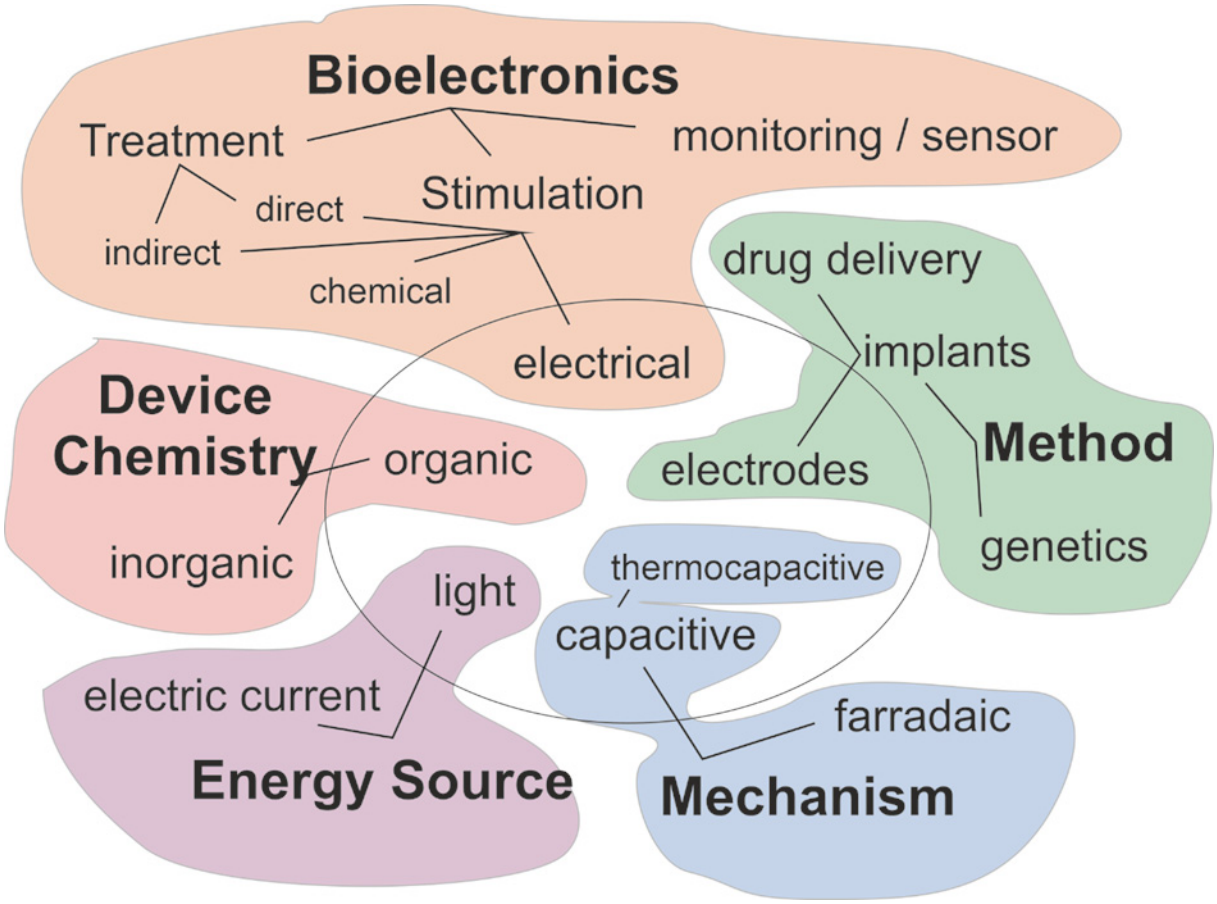

Figure 1 Overview of concepts and methods required for the optical control of neuronal signaling with organic bioelectronics.

upon light absorption. These photothermocapacitive devices have a large and structured surface area compared to their diameter, allowing rapid heating of the nearby cell membranes and therefore changing the capacitance of the cell membrane.

The second device is an organic semiconductor similar to its inorganic counterpart known from photovoltaic cells for electricity generation. However, the mechanism for neurostimulation is provided by a generated electric field in the electrolytic environment of an *in vitro* or *in vivo* system. The semiconducting materials charge during light absorption, causing the formation of an electrolytic double layer and a current between the oppositely charged electrodes. This photocapacitive mechanism results in a potential difference capable of polarizing nearby cell membranes.

1.3 The Cell System, the Plasma Membrane and Neuronal Signaling

Cells are compartmentalized to provide the necessary conditions for many different functions. Herein, the plasma membrane is the most important entity for the organization of the cell. It separates the interior from the outside environment and is responsible for many processes that are crucial for cell functions, such as cell-cell communication [42], intracellular and extracellular signaling [43], the transmission of electrical signals [44], cell protection, and many more [45]. Especially the electrical activity of neurons and their ability to elicit and transmit action potentials (APs) is crucial for information signaling over longer distances in complex organisms.

1.3.1 Cell Membrane and Electrolytic Environment

The cell membrane is a lipid bilayer composed primarily of phospholipids and cholesterol [46]. In addition, fatty acids such as cholesterol or glycolipids are essential for structural integrity and cell stability. The proteins within the membrane have various functions that range from intracellular and extracellular signaling to the maintenance of the proper electrolytic environment (Figure 2).

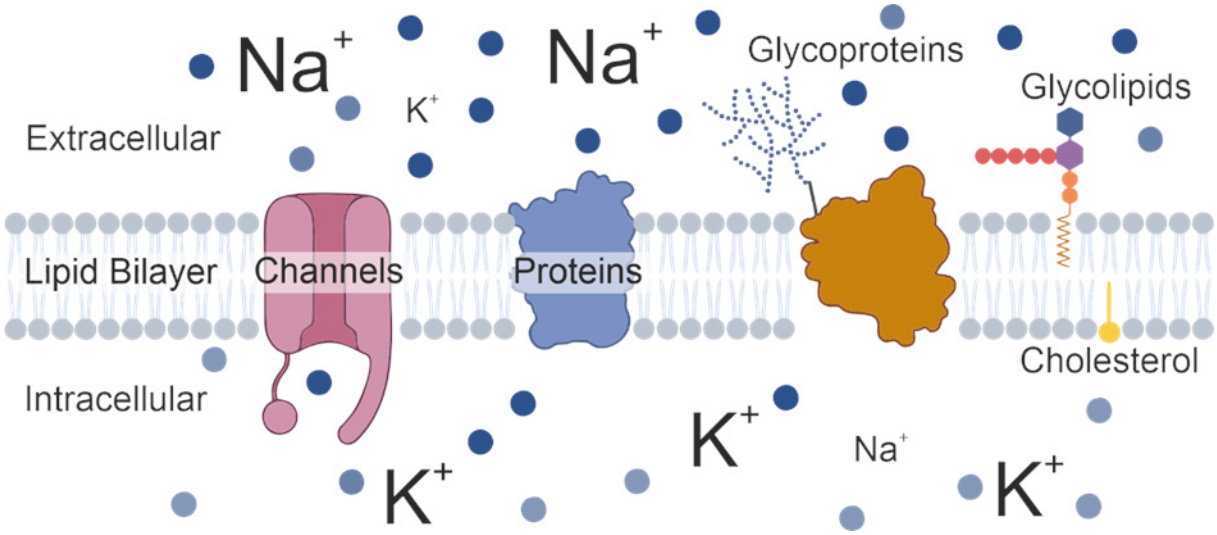

Figure 2 Schematic representation of a cell membrane with a lipid bilayer composed of the most common components such as phospholipids, cholesterol, and glycolipids, as well as different globular or integral proteins. Electrolytic composition with high potassium (K^+) in the cell and high extracellular sodium (Na^+) concentration [47].

Most processes within the cell require exact ion concentrations to be fully functional. Especially excitable cells such as neurons require a well-balanced electrolytic environment for signal induction and transmission, as well as for maintaining their resting membrane potential (V_{rest}). The typical

intracellular and extracellular ion concentrations for neurons are 12 mM Na^+_{in}, 145 mM Na^+_{out}, 155 mM K^+_{in} and 4 mM K^+_{out} [48]. This concentration gradient is generated and maintained by ion pumps which lead together with the permeation through K^+ channels to a V_{rest} of around -70 mV. The membrane is semi-permeable for ions to varying degrees. Charge separation and concentration gradient counteract diffusion until an equilibrium is reached. The equilibrium for each ion type can be calculated by the Nernst equation (1) with the Nernst potential E_{ion}, gas constant R, temperature T, number of valence electrons z_{ion}, Faraday constant F and concentration c.

$$E_{ion} = \frac{R * T}{z_{ion} * F} * \ln \frac{c(ion_{in})}{c(ion_{out})} \quad (1)$$

The membrane potential V_m is mostly dependent on the K^+ ion distribution but the membrane is also permeable for Na^+ and Cl^- to a certain degree. This correlation can be described by the Goldman equation (2).

$$V_m = \frac{R * T}{F} * \ln \frac{P_{K^+} * c(K^+{}_{out}) + P_{Na^+} * c(N^+{}_{out}) + P_{Cl^-} * c(Cl^-{}_{in})}{P_{K^+} * c(K^+{}_{in}) + P_{Na^+} * c(Na^+{}_{in}) + P_{Cl^-} * c(Cl^+{}_{out})} \quad (2)$$

1.3.2 Ion Channels

Ion channels are transmembrane proteins that facilitate the transport of ions across the cell membrane. In contrast to pores, most channels have an ion selectivity ranging from a low to a very high affinity for different species. The water molecules attached to ions are often substituted by the charged side chain residues of the ion channel selectivity filter and the ion concentration increases on one side of the membrane [49].

Ion channels can be classified into many different groups. Leak channels are constitutively open and allow free ion flow across the membrane along their concentration gradient. The K^+ leak channels are important for maintaining the resting membrane potential in a cell since the Na^+/K^+-pump is always active and does not stop when the typical intracellular K^+ concentration is reached. Excess K^+ ions can flow out of the cell until the electrochemical equilibrium is in balance again [50].

Another type are ligand-gated ion channels which also allow the flux of Na^+, K^+, Cl^- or Ca^{2+}. In contrast to the previous ones, ligand-gated channels require an external stimulus to switch from a closed state to an open state. This is achieved mainly by allosteric binding of an effector molecule to protein domains that can bind extracellular mediators such as neurotransmitters or intracellular mediators

such as nucleotides or even other ions itself [49]. Well studied ligand-gated ion channels include a receptor, for example, for γ-aminobutyric acid (GABA), glutamate, or nicotine acetylcholine [51].

Mechanosensitive ion channels sense the membrane tension or curvature in procaryotic and eucaryotic cells and change their conformation upon stress. This is important to regulate cell homeostasis which can protect against osmotic stress [52], or it can provide information on other mechanical deformations that might be a stimulus for sensing the environment, for example in hair cells in the cochlea [53].

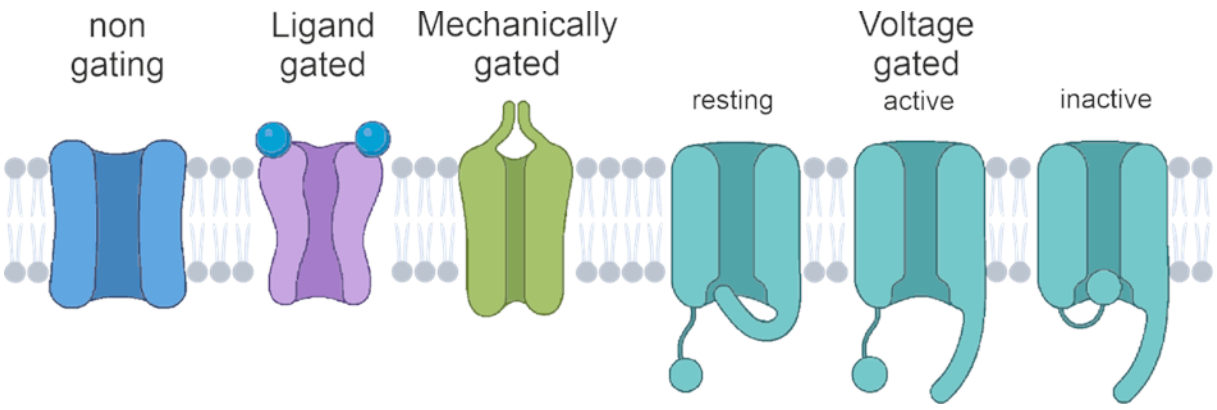

Figure 3 Overview of different ion channels with leak channels that are constitutively open and gated ion channels that change their conformation upon binding a ligand, sensing mechanical stress or a voltage change on the membrane [47].

The last major group of ion channels are voltage-gated channels that respond to a potential change at the membrane that induces a conformation change. Especially Na^+, K^+ and Ca^{2+} ion channels play a crucial role in the initiation and propagation of stimuli in excitable cells [54]. They can form protein complexes with heterologous subunits, but the general mechanism and function principle is the same for most of these channel types.

Potassium channels are assembled from four identical subunits that constitute a pore-forming complex [55] (Figure 4 A). Sodium and calcium channels have four homologous subunits that are connected to a single protein (Figure 4 B). All voltage-gated ion channel subunits consist of six transmembrane-spanning helices labeled as segment S1-S6. The S4 domain contains a series of basic amino acids, such as arginine (R) and lysine (K) in its sequence which are positively charged.

The membranes of excitable cells that undergo rapid depolarization become less negative on the inside. The positively charged residues (Figure 4 A right, blue barrel) move within the membrane a little toward the extracellular space, causing a conformation change [56] that can be recorded as a gating current. Specific ion species that passed the selectivity filter can then flow through the open pore generating an ion specific current that can be inward or outward rectifying.

These ion channels can have several open and closed states depending on the charge movement of the sensor, but especially Na_v ion channels are well known to have a third state: the inactive state. There are several mechanisms through which these channels are inactivated. The most prominent one is the N-type inactivation. The first residues at the N-terminus form a barrier that can block the pore on the cytoplasmic side, restricting the ion flux across the membrane [57, 58]. This process is reversible and can be achieved by a hyperpolarization of the cell.

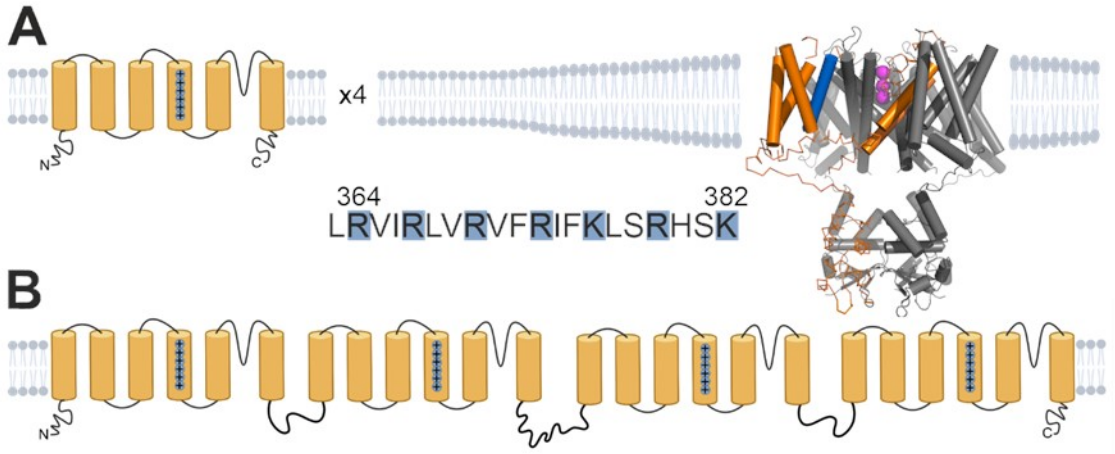

Figure 4 Schematic overview of two major voltage-gated ion channel species. (A) Shaker-related ion channel formed by 4 homologous subunits with an R and K rich voltage sensor in the transmembrane segment 4. The right side highlights a monomer (orange) of human $K_v1.3$, the voltage sensor (blue), and potassium ions in the selectivity filter (magenta) (PDB-ID: 7SSY). (B) Schematic representation of the structure of Na_v and Ca_v ion channels with 24 transmembrane-spanning helices grouped into four identical domains. Concept adapted from [54] and created with [47].

1.3.3 General Electric Description of the Cell

Alan Hodgkin and Andrew Huxley first described the ionic currents in giant squid axons and established a model that mathematically describes the propagation and initiation of an action potential [59]. The membrane of an excitable cell can be described in an equivalent circuit model (Figure 5) with three components (equations (3) – (5)):

The plasma membrane acts with its phospholipid bilayer as a dielectricum. Thus, it forms a parallel plate capacitor C with a membrane capacitance C_m, a charge Q, and an electrical potential V across the membrane.

$$C = \frac{Q}{V} \tag{3}$$

The conductance g (1/R) of ion channels is described as reciprocal of the resistance R. Hodgkin and Huxley defined a resistance for Na^+ channels R_{Na}, K^+ channels R_K and for the leakage of Cl^- ions a resistor R_{Cl}.

$$R = \frac{V}{I} \quad \Rightarrow \quad I = g * V \tag{4}$$

The last component is the electromotive force EMF_{ion} of an ion which is the difference between the membrane potential V_m (see Equation (2)) and the Nernst potential of a given ion E_{ion} (see Equation (1)).

$$EMF_{ion} = V_m - E_{ion} \tag{5}$$

The total membrane current I_{total} is divided into a capacitive current I_c that charges the capacitor (membrane) and an ionic current I_i that flows through all ion channels. The current of a single ion channel I_{ion} results from equation (4).

$$I_{total} = I_c + I_i \text{ with } I_c = C_m \frac{dV}{dt} \text{ and } I_i = I_{Na} + I_K + I_{Cl} \text{ while } I_{ion} = g_{ion} * EMF_{ion} \tag{6}$$

With these equations and the equivalent circuit model (Figure 5), one can approximate the behavior of an excitable cell upon stimulation and whether AP firing is triggered or not. This stimulation pulse can come from either a classical electrode inducing a current with a given amplitude and duration to reach the threshold potential or from other stimulation methods (see Section 1.4).

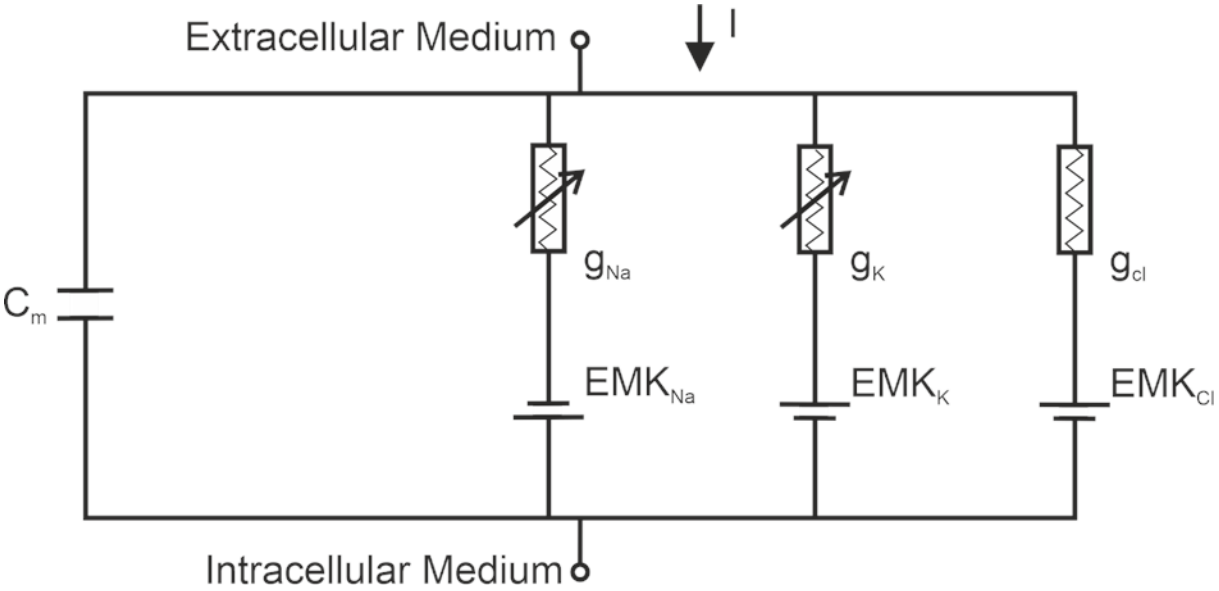

Figure 5 Equivalent circuit model of a cell.

1.3.4 Action Potentials

The resting membrane potential is mainly driven by the K^+ concentration gradient across the cell membrane and the electrical gradient of cations that flow out the cell, making the interior more negative until an equilibrium is reached (see Equations (1) and (2)) [60]. This Nernst potential (E_{ion}) together with the membrane potential across the membrane constitute the electromotive force together with the conductance, determining the current flow of ions. Since there is a higher permeability for K^+ in the plasma membrane than for Na^+ the overall resting membrane potential is closer to E_K than to E_{Na} [61].

This can have pathophysiological effects when there are elevated levels of K^+ in the blood. People with hyperkalemia have more depolarized cells, which can inactivate Na^+ channels while K^+ channels remain open, causing cells to become refractory which causes severe problems in neuromuscular activation [62]. However, this refractory effect is also known from healthy heart tissues and is caused by altered ion concentrations through altered membrane permeabilities. This changes the V_{rest} of special cells and enables a directed propagation which is necessary for normal heart physiology. The typical resting membrane potential in neurons is -70 mV but can range from -90 mV in skeletal muscles [63] to -50 mV in aortic smooth muscles [64].

A cell reacts in two different ways when a stimulus reaches an excitable cell. The neuron fails to initiate an AP if the threshold potential is not reached. Several stimuli can add up or cancel each other out in

complex neural connections. The cell will initiate or propagate the AP when the membrane potential exceeds the threshold potential due to the all-or-none law. Voltage-gated Na^+ channels react to this membrane potential change and activate. Positively charged ions flow into the cell during this depolarization phase which further alters the membrane potential allowing more ion channels to open. This feedback loop leads to an overshoot that even switches the membrane polarity. One can observe the inward current of the Na^+-cation in the negative current trace (Figure 6 A – blue). The conductance of the voltage-gated Na^+ channels peaks earlier (Figure 6 B – blue) than the current. This discrepancy is explained by equation (**6**) and the EMF that is the driving force for the ion flow.

Na^+ channels already start to inactivate during the overshoot, while voltage-gated K^+ channels open and allow the flux of K^+-cations out of the cell (positive current in Figure 6 A – red). The cell membrane repolarizes and even hyperpolarizes due to slower channel kinetics of K^+ compared to Na^+ channels. No further APs can be initiated during the refractory period since voltage-gated Na^+ channels need some time to transition from the inactivated state to the resting one. This slow transition and the rapid inactivation also allow for a unidirectional propagation of the signal along the membrane. The ionic concentration in the extra- and intracellular medium changes slightly compared to the charge transfer switching the membrane polarity from negative to positive and then back again. The Na^+/K^+ pump restores the ionic ratio to the levels before excitation. This process takes energy in the form of one ATP for pumping three Na^+ ions out of the cell and two K^+ ions into the cell.

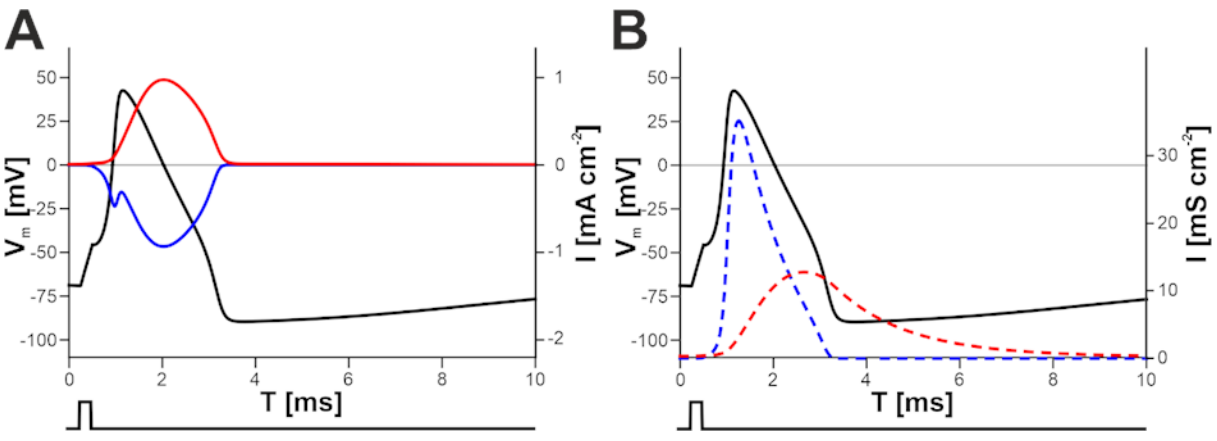

Figure 6 Currents and conductance during action potentials. Membrane potential (black) of a squid axon with (A) currents and the (B) conductance of Na^+ (blue) or K^+ (red) ion channels. Traces are calculated with the program Hodgkin-Huxley Cell Model from Robert Arnold (Gottfried Schatz Research Center – Biophysics, Medical University of Graz, Austria) based on the Hodgkin-Huxley equations.

The membrane of excitable cells deviates not only in the permeability of ions but also in the amount and composition of voltage-gated Na^+ and K^+ channels which further might have slightly different kinetics. This leads to a diversity in the shape and nature of APs [65] (Figure 7).

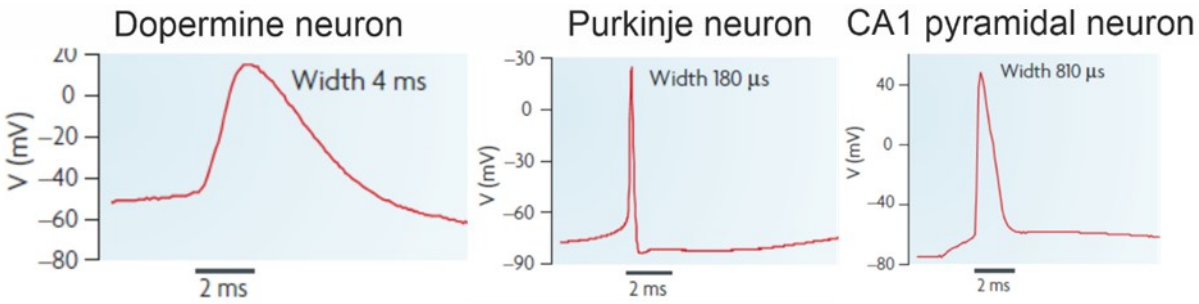

Figure 7 Diversity of action potentials in mammalian central neurons. Adapted and reprinted with permission from Springer Nature: Nature Reviews Neuroscience, [65], according to license number 5342390928481.

1.3.5 The Patch Clamp Technique

The electrical description of the cell helps to understand the basic biological mechanisms in excitable cells. One successful method enabled high-quality measurements of the membrane potential or the current flow across the membrane within the last decades. In the late 1970s and 1980s Erwin Neher and Bert Sakmann developed the foundation of the patch clamp technique by measuring small electrical currents of single ion channels in denervated frog muscle fibers [66].

Modern setups vary in individual components, but Figure 8 shows a standard configuration of a patch clamp rig. The microscope, the head stage of the pre-amplifier and the reference electrode are shielded by a Faraday cage to block external interfering electromagnetic fields. The measured analog signals are transmitted to an amplifier and digitized for data acquisition. For the purpose of this work, we extended this configuration by a light source for extracellular stimulation of cells through light-sensitive organic bioelectronics.

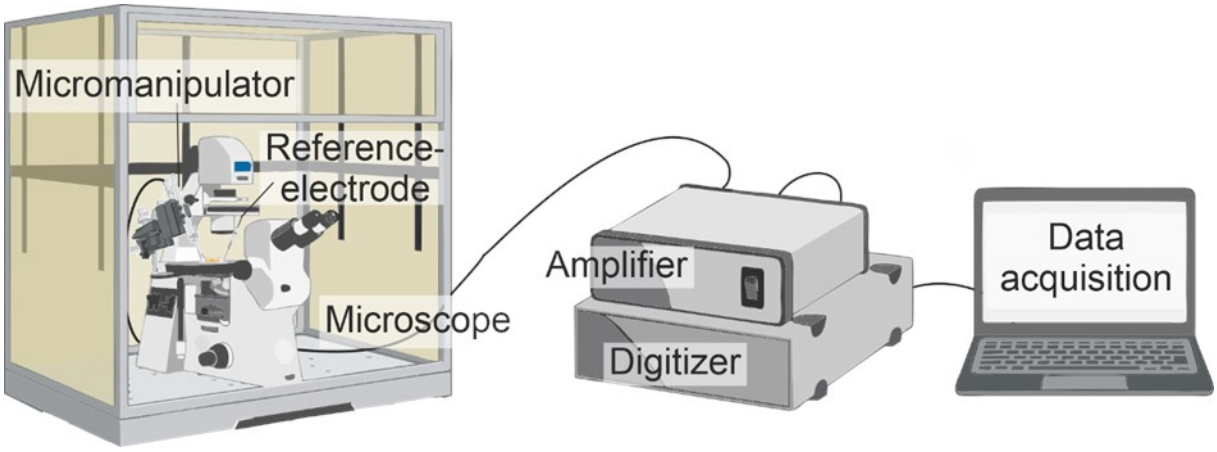

Figure 8 Schematics of an electrophysiology set-up with a microscope in a faradaic cage. The measuring electrode (not shown) is mounted to a micromanipulator to precisely target cell membranes and connected to an amplifier via the preamplifier in the head stage. A digitizer converts analog signals into digital signals for electronic data acquisition. [47]

A holder securing the coverslips is submerged in an electrolytic solution and contacted by a silver reference electrode coated with AgCl. The ionic current is transformed into an electric one and vice versa.

$$AgCl \quad \rightleftharpoons \quad \begin{matrix} & Ag^+ & \\ +e^- & \downarrow & -e^- \\ & Ag & \end{matrix} \quad + \quad Cl^-$$

The measuring electrode consists of a glass capillary with a small tip and an opening in the µm range. The electrode is filled with a conducting solution that mimics the intracellular ion concentration which is also in contact with an Ag/AgCl electrode (Figure 9 A) to close the circuit. There are different configurations of how the pipette contacts a membrane. In the cell-attached mode (Figure 9 B), one approaches the cell with a slight overpressure which is then released when close to the membrane. This increases seal resistance and reduces noise by forming a tight seal between the membrane and the electrode [67]. This mode allows to record spontaneous firing of excitable cells or single ion channels, since the cell interior is not altered [68].

The rapture of the cell membrane is achieved by a sudden change in pressure. This configuration is called whole-cell (Figure 9 C) and provides electrical access to the interior of the cell similar to a microelectrode that impales the cell directly [69]. In contrast to single channel experiments, this method allows to measure e.g., the sum of currents flowing through all membrane channels.

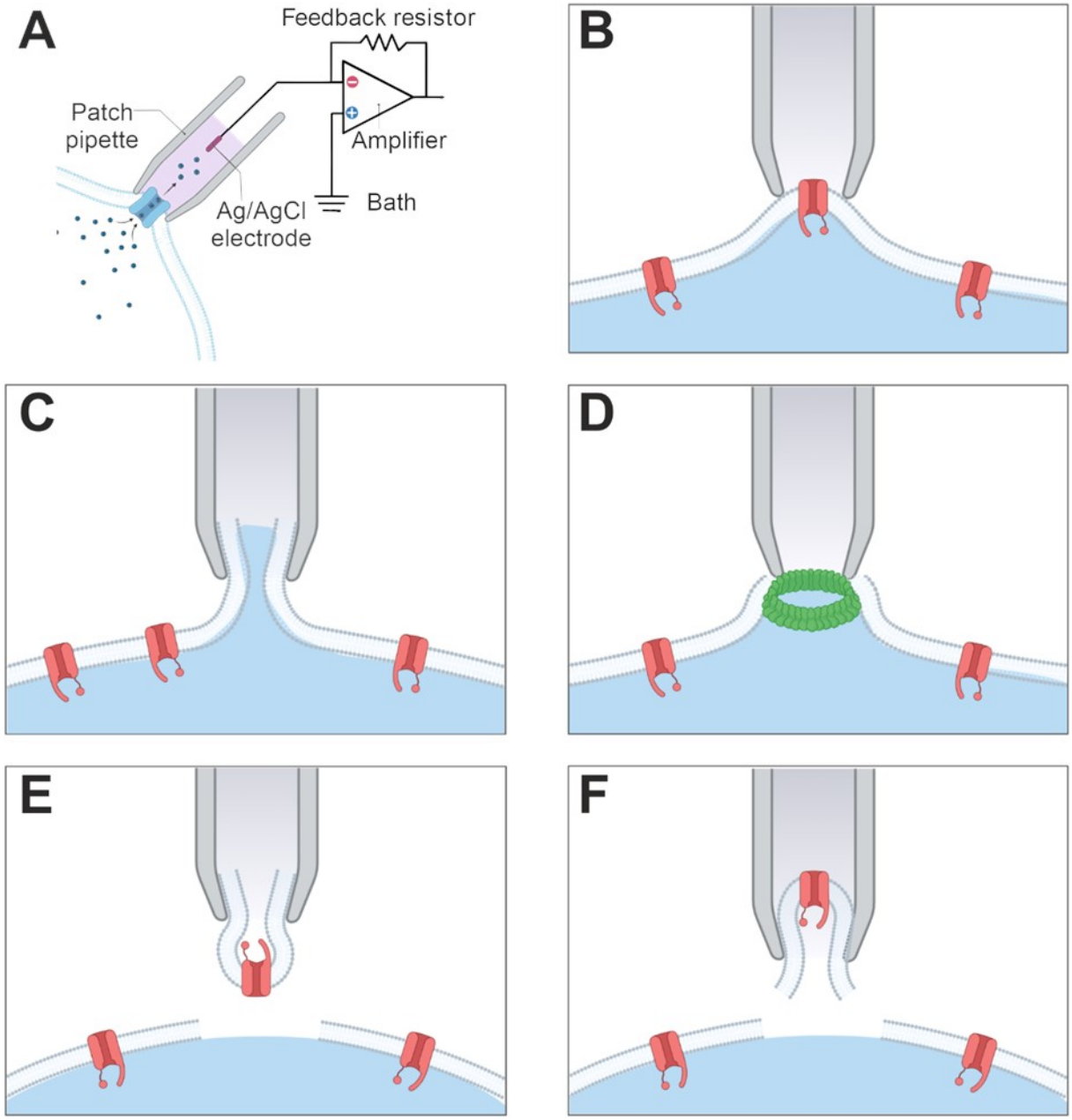

Figure 9 The patch clam technique and its configurations. (A) General schematics of an amplifier connected to a measuring electrode in a patch pipette. (B) Cell-attached, (C) whole-cell, (D) perforated-patch, (E) outside-out and (F) inside-out configuration. [70]

Hamill et al. developed two further methods in 1982, the outside-out (Figure 9 E) and inside-out (Figure 9 F) configuration [71]. Both techniques rapture the cell and take a small patch of the cell membrane which is often used to measure single ion channel currents. The method is also commonly used in small cells with low capacitance or high expression of some ion channel species [72].

To gain electrical access to the cell without rapturing the membrane, pore-forming antibiotics can be introduced into the pipette solution. This prevents a washout of the cell interior and provides an exchange of most monovalent ions through the membrane. Larger molecules remain in the cytoplasm, allowing the study of signaling pathways and other scientific questions that require an intact cell. Another big advantage of the perforated-patch configuration (Figure 9 D) is, that once established, the perforated patch provides a more stable seal and longer recording times which is useful for long-term experiment in excitable cells.

The patch clamp technique provides two modes of operation. The voltage clamp is often used to study ion channel gating by controlling the membrane voltage. To maintain this clamped voltage, a current flows across the membrane which is recorded by the amplifier. In current clamp mode, a current is injected into the cell and the membrane voltage is recorded which gives information about e.g., the depolarization of excitable cells. The true current clamp mode is achieved by a voltage follower circuit in the amplifier. In this work, we just used an I-V converter amplifier with capacitive feedback circuit.

1.4 Stimulation

1.4.1 Chemical and Mechanical Cell Stimulation

Cell stimulation can be achieved with a multitude of techniques for clinical applications and research-related questions. Most established tools use chemical methods, such as chemo attractants for cell migration or invasion studies [73], drug administration [74] for patient treatments, or even artificial chemical stimulation that introduces non-physiological receptors or agents into cell signaling pathways [75]. Another wide area is the mechanical stimulation of cells and tissues [76] by physical stretching of cell cultures that stimulates hormone production [77] or stem cell differentiation [78].

1.4.2 Electrical Stimulation of Excitable Cells

The most common form of stimulation anyhow is the electrical coupling of excitable cells which can be subdivided into three major classes: Direct coupling, capacitive coupling, and induction (Figure 10). Direct current coupling is the process of direct cell stimulation in which electrodes are contacted to excitable tissues or membranes. The electric current thereby causes a potential change and a polarization of the membrane. This method allows for the use in *in vitro* or in vivo applications such as neurite growth [79], bone fracture healing [80, 81], and stem cell differentiation of neuronal cells [82]. Capacitive coupling produces a homogeneous and uniform electromagnetic field. The probe is located between two electrodes [83] and is not in direct contact with the electrode. Since this does not require a conductive scaffold, capacitive coupling allows noninvasive stimulation [84]. Inductive coupling generates a controlled electromagnetic field that generates small currents and potential differences close to a probe by using coiled electrodes [83].

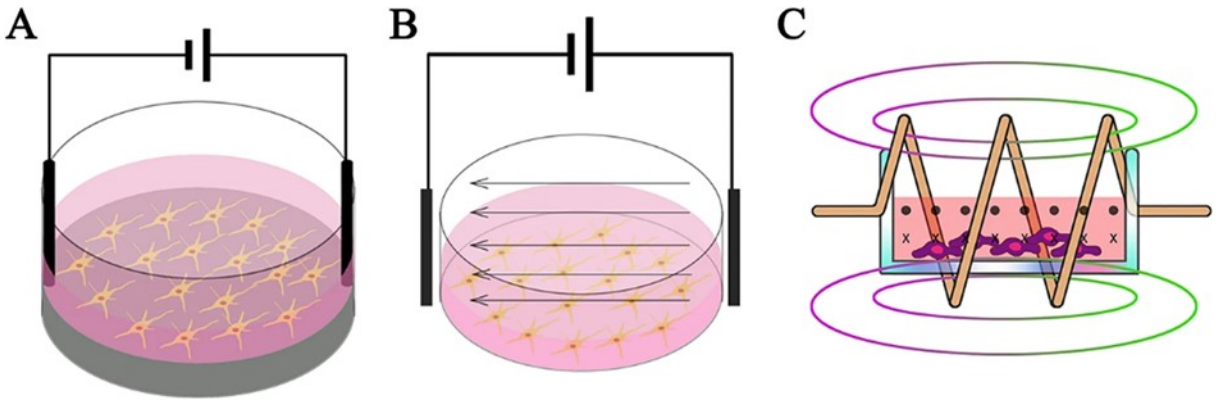

Figure 10 Electrical stimulation of cells via (A) direct or (B) capacitive coupling or (C) induction. Reprinted with permission from Springer Nature: Biomaterials Research, [84], under the terms of the Creative Commons CC BY license.

1.4.3 Electrode Materials

Electrodes are made of metals and metal alloys or polymers that can be either organic or inorganic. Metal electrodes, in particular, raise a certain number of problems often related to faradaic processes (see Section 1.4.4). Although noble metals such as gold are known for their inertness and stability in solution, various studies have reported that Au or Au-alloy electrodes caused cell death in primary and cell line cell cultures [85] due to the release of metal ions. Other materials exhibited reduced biocompatibility [86] when magnesium was utilized or toxicity through the application of silver and copper electrodes [87]. Another problem for *in vitro* use is the alteration of the medium or electrolytic environment by changing the pH [81] or oxygen concentrations [88]. Inorganic semiconducting materials, such as silicon, exhibit higher biocompatibility and less toxicity [89] which explains their widespread use in microelectrode arrays [89, 90].

However, in recent years, organic semiconductors and conducting biopolymers have matured into an alternative in electrode design. Current flow and charge transfer can occur via the transport of electrons or protons and ions in these electrodes. The abundant and naturally occurring pigment melanin was among the first conductive organic compounds found and studied for the use in broader applications [91]. A more modern and commonly used material is the PEDOT polymer (poly(3,4-ethylenedioxythiophene)) mixed and doped with the PSS polymer (polystyrene sulfonate). PEDOT:PSS is widely used in electrode designs for neurostimulation such as a coating for microelectrode arrays [92] or as a replacement for transparent conductors like ITO (indium tin oxide) [93].

A subclass of organic semiconductors is the class of photoactive pigments. Indigo and its derivatives have been used for centuries, but the first application as a bioelectric photovoltaic cell was developed in the 1980s [91, 94]. In contrast to other organic compounds, indigo is very light-stable due to the process of excited-state proton transfer [95]. Through photoexcitation, indigo reaches an excited state which exhibits another reactivity compared to the ground state. Rapid proton transfer [96] allows rapid deactivation from that excited state and a stabilization of the molecule.

The semiconducting property of indigo is related to the nature of its crystalline structure [91]. Indigoid monomers form a polymer through hydrogen bonds during crystal growth allowing π–π stacking between the aromatic rings which is important for the charge transport and mobility (Figure 11 A). Other variants, such as epindolidione, reach their high mobility by forming linear chains [97] (Figure 11 B). Within this work, pigments similar to indigo such as metal free phthalocyanine (H_2Pc) and epindolidione were used to exploit their material properties for photocapacitive and thermocapacitive stimulation.

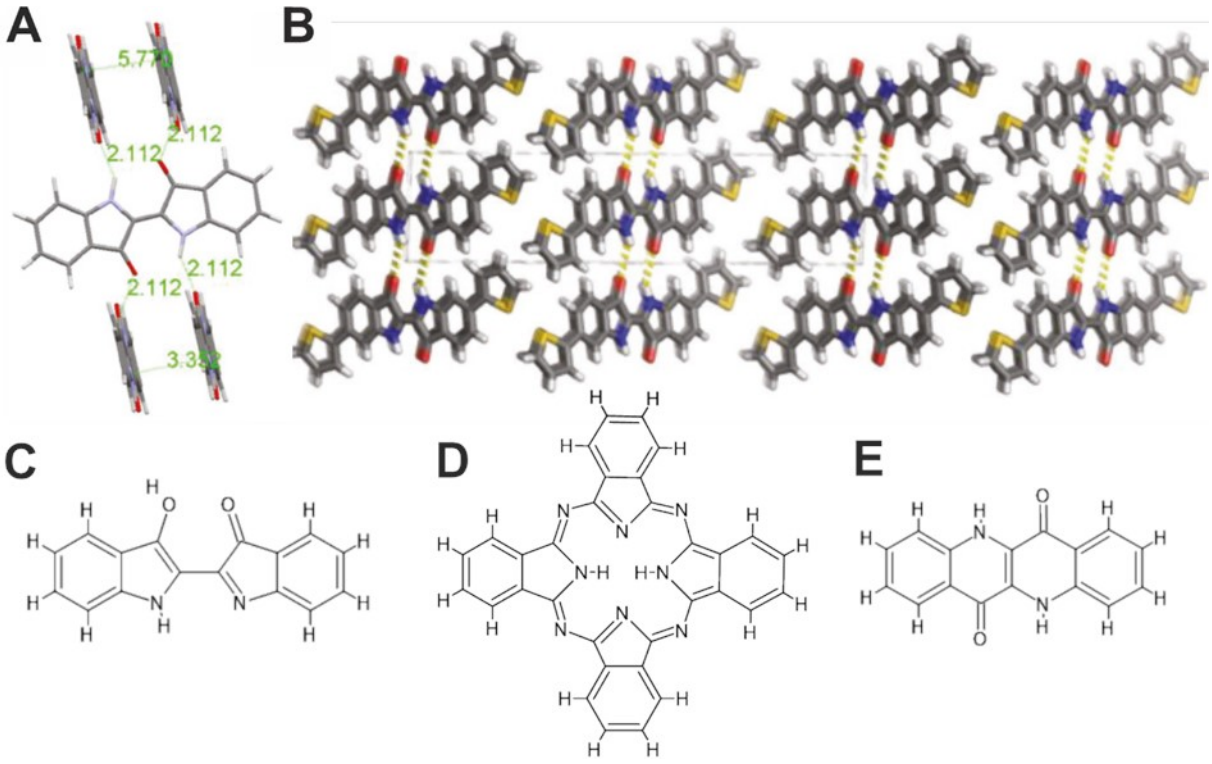

Figure 11 Crystal structure of indigo and variants. Hydrogen bonds between (A) π–π stacked indigo monomers or (B) linear bonded indigo derivatives. (C) Indigo, (D) metal free phthalocyanine (H_2Pc) and (E) epindolidione. (A) and (B) were adapted and reprinted with permission from John Wiley and Sons: Advanced Materials, [91], according to license number 5347721276562.

1.4.4 Stimulation Mechanisms

All cells in tissues and organs are surrounded by an extracellular fluid containing ions of opposite charge. *In vitro* cell cultures also use media and solutions that mimic a physiological ion concentration. During electrode stimulation, the main charge carriers in the fluid are cations and anions. Electrical circuits, however, use electrons as charge carriers. This creates the need to transduce the form of the charge carrier from electrons to ions at the interface between the stimulation electrode and the electrolyte for stimulation [98, 99].

Faradaic

Faradaic charge transfer occurs when electrons are transferred directly between the electrode and the electrolyte. If the working electrode is negatively charged, then nearby reactants are reduced while oxidative reactions occur at the counter electrode [100]. This can lead to oxide formation and metal

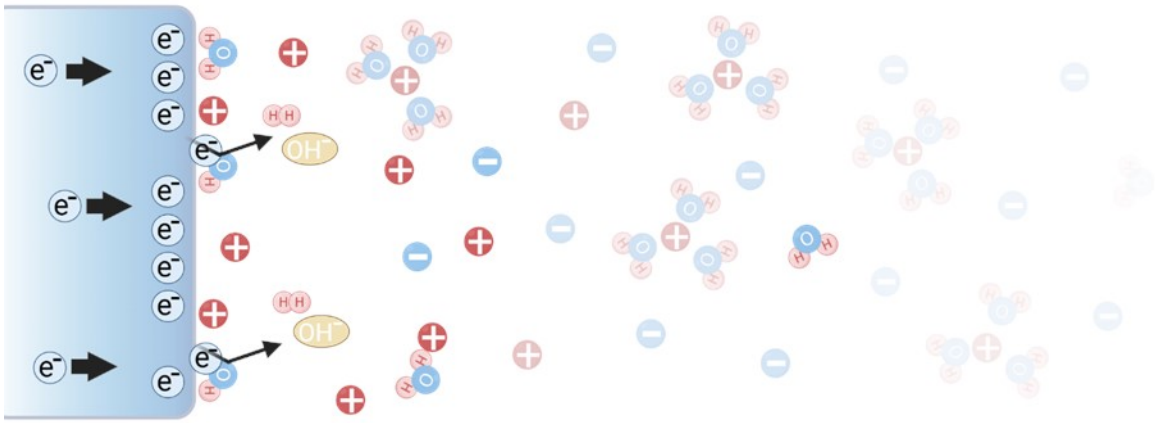

Figure 12 Faradaic processes on an electrode. Charge transfer between an electrode and the electrolyte causes faradaic redox reactions. The products are likely to diffuse away, preventing a reverse reaction. [47]

deposition at the electrode interfaces, or to a pH change in the electrolyte due to the reduction of water [98]. Reversing the current flow by switching from a cathodic current to an anodic one does not recover the educts since most reactants diffuse away during a stimulation pulse (Figure 12). These processes are not optimal for cell stimulation because of the change in the physiological electrolyte or because of the durability of the electrodes that are consumed or destroyed by electrochemical processes.

Capacitive

An electric potential forms between the electrode and the electrolyte, creating an electric field when the electrode is charged. This means that electrons accumulate at the negatively charged surface of the cathode and positively charged ions in the electrolyte accumulate next to the electrode, forming a double layer capacitor. Likewise, also other charged molecules orient in that field and a potential gradient forms within the electrolyte (Figure 13) [98]. The injected charge is also stored in the capacitor. The opposite process occurs at the counter electrode. When the polarity is reversed, the injected charge is recovered without transferring electrons throughout the electrolyte electrode interface.

This is a safer method of cell excitation because it mimics natural-occurring processes during stimulation. However, if the injected charge is too high, faradaic processes will also occur alongside the capacitive ones.

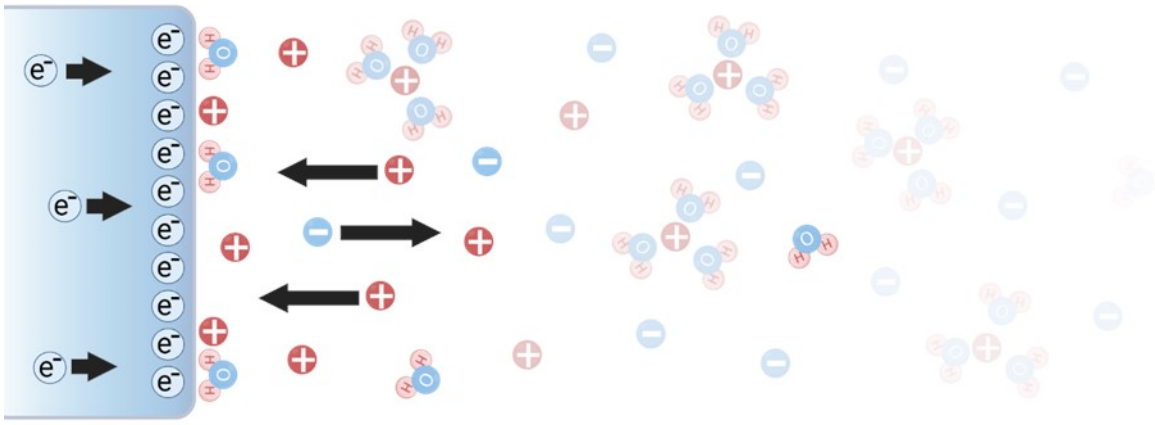

Figure 13 Capacitive processes on an electrode. Charge transfer between an electrode and the electrolyte. Formation of a double layer with oppositely charged charge carriers. The schematics depict a cathodic stimulus where the electrode charges negatively and attracts positive charges from the electrolyte. [47]

The capacitance and therefore the amount of charge that can be injected into the electrolyte are dependent on the size of the electrode. The surface area can either be increased by microstructuring the electrode [101, 102] as in the case of 3D shaped pigment plates [103] within this thesis or by the use of pseudocapacitive materials such as PEDOT:PSS [104]. This polymer has a high volumetric capacitance [105] due to its conducting polymer chains that surround a large area which is accessible to the electrolyte (Figure 14) [106].

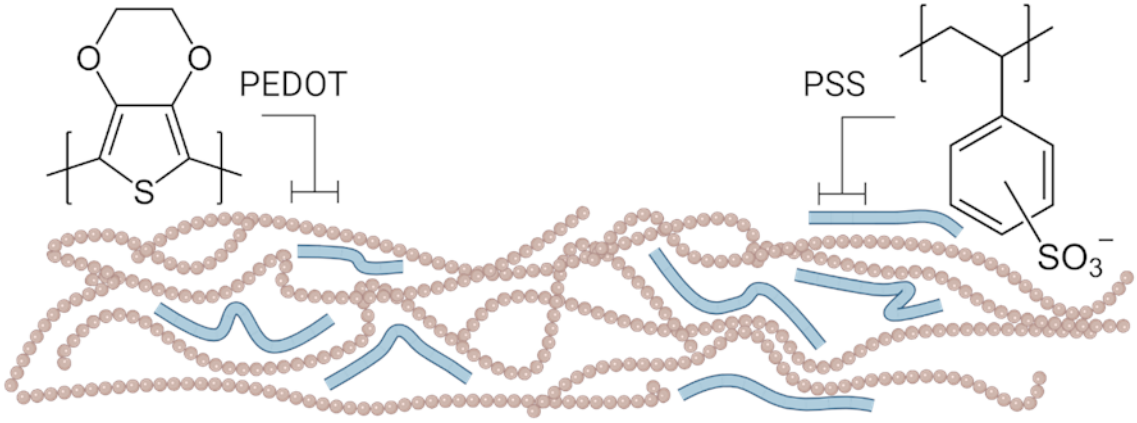

Figure 14 Schematic representation of PEDOT:PSS with amorphous polymers from a mixture of Poly(3,4-ethylenedioxythiophene) and polystyrene sulfonate.

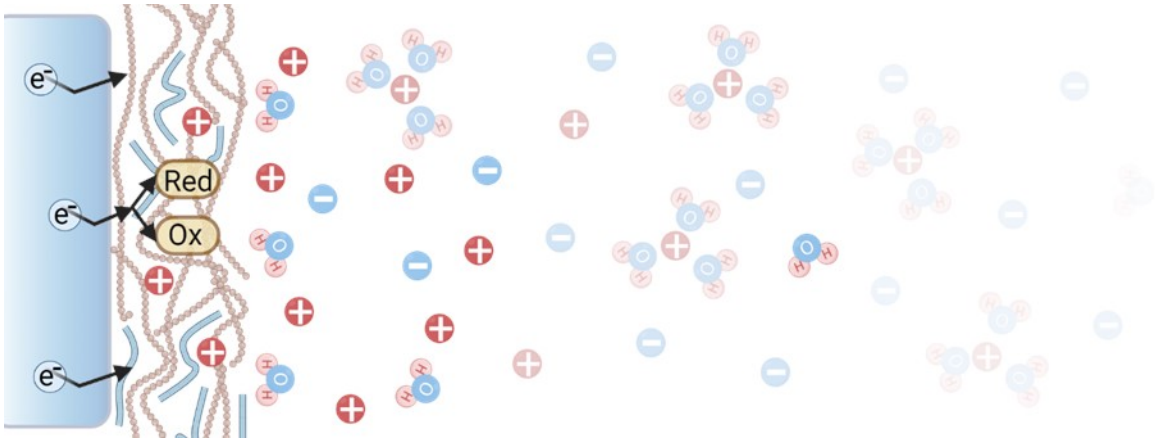

Figure 15 Pseudocapacitive processes on an electrode with a PEDOT:PSS coating. [47]

Pseudocapacitors also transfer electrons, as in faradaic processes, but the redox products cannot diffuse away because they are part of the electrode or its coating. Therefore, the electrolyte is not altered and the overall composition of the electrode is restored by reversing the currents (Figure 15).

1.4.5 Stimulation Parameter

Neurostimulation devices are typically operated with a working and a counter electrode. A cathodic current flows when the working electrode is negative compared to its pre-stimulus potential. Is the electrode driven positive, then the current is anodic [98] (Figure 16 A). This current can be continuously injected creating a monophasic pulse or reversed to create a biphasic pulse (Figure 16 B) which also reverses electrochemical processes as previously described [100]. The current of both phases can either be balanced or imbalanced (Figure 16 C). Positive and negative phases can be continuous or interrupted (Figure 16 D).

A cathodic-leading balanced biphasic pulse is quite advantageous for cell stimulation for various reasons [107, 108]. If the anodic phase does not match the cathodic phase in terms of total injected charge, some charge may remain at the electrode and decrease the effect of succeeding stimulation pulses. A delay between the cathodic and anodic phases might also contribute to a loss of charge, as diffused products cannot be recovered quickly enough.

The cathodic phase depolarizes the attached part of the membrane, causing voltage-gated Na^+ channels to initiate an AP at this membrane patch. The non-attached membrane slightly hyperpolarizes in this process. An anodic leading stimulation has phases with reversed polarities and is capable to induce AP firing on the free membrane [109].

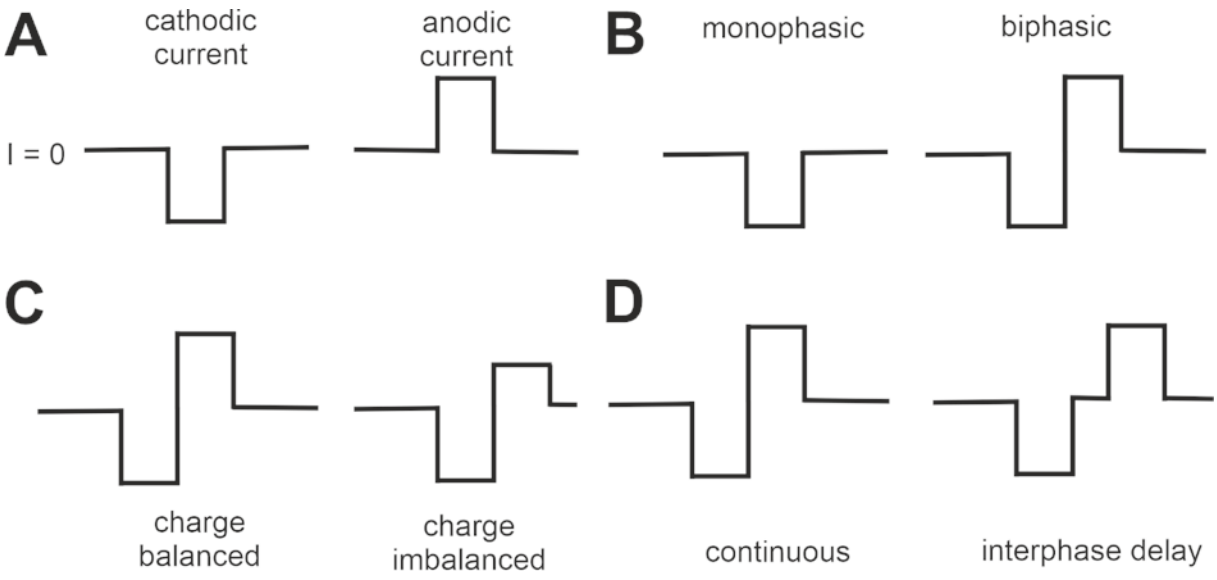

Figure 16 Stimulus pulse phases for electrode stimulation. (A) Monophasic pulses with cathodic or anodic currents. (B) Comparison between a monophasic pulse and the opposite phases of a biphasic pulse. (C) Charge balanced and imbalanced pulses; the imbalance can be either on the cathodic or anodic side. (D) Comparison between biphasic pulses with a continuous profile or an interphase delay between cathodic and anodic phase.

If the charge of a biphasic pulse is not balanced, then both configurations might induce APs at their respective site of action, dependent on the amplitude of the pulse. Other parameters, such as the time between two pulses, can also affect AP firing. Rapid succeeding stimulation pulses can increase membrane polarity increment wise with every stimulus.

1.5 Light as an Energy Source

Chemical neurostimulation is widely used in science and is successful in the treatment of many pathophysiological conditions. However, for many applications, this method is not specific enough to work precisely on local targets. Wired electrical stimulation solves this problem and enables precise control of neuronal signaling processes with greater spatiotemporal resolution compared to chemical stimulations. Since the disadvantages of electrical stimulation around biocompatibility [110], inflexible design [111, 112], inflammation issues [113] and power supply are well known, the search for promising new methods has drawn more and more attention to light-activated approaches.

The simplest method is direct light absorption by tissues. Water molecules absorb infrared light [114] and locally increase the surrounding temperature [115] and thus depolarize the cell membrane by increasing the electrical capacitance [116]. Endogenous biomolecules, such as those present in mitochondria, are also capable of absorbing light, but their applicability as a target is still under debate [117].

1.5.1 Stimulation with Optogenetics and Photopharmacology

The optogenetic approach combines genetics and light to investigate a multitude of phenomena *in vitro* and *in vivo*. However, its roots originate in neuroscience [118]. Opsins are light-sensitive proteins that transform a light stimulus into a signal that can be processed by cells. The first opsins found encoded for ion channels. That genetic information was derived from algae or other microbes.

Boyden et al. transfected neurons with channelrhodopsin-2, a light-gated cation channel [119]. They stimulated their probes with blue light and evoked an inward current with microsecond pulses. Neuronal stimulation could also be achieved by a series of light pulses that might induce trains of APs or synaptic events [120]. The rapid advancement in this field nowadays leads to applications that can precisely control single neurons and trigger gain or loss of function mechanisms (Figure 17) [118]. This is achieved by genetic introduction of different molecules into the cell, but also through a variety of different stimulation wavelengths and pulse protocols [40].

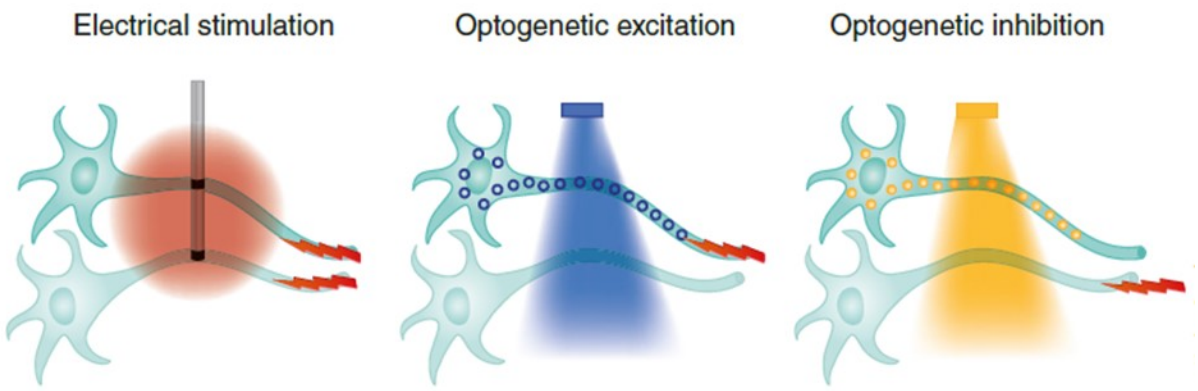

Figure 17 Difference between electrical and chemical stimulation. Targeted neurostimulation of single cells for the activation (channelrhodopsin) and inhibition (halorhodopsin) of single cells with different wavelengths. Reprinted with permission from Springer Nature: Nature Methods, [118], according to license number 5356970964744.

Photopharmacology introduces light-sensitive ligands to their targets that can switch conformation or undergo cyclization upon light stimulation [121]. These mostly artificial photoswitches have an azobenzene or diarylethene group within their structures that photoisomerize the molecule into an active or inactive conformation. Photoswitches can be administered as free-circulating drugs or tethered to their specific targets such as ion channels [41].

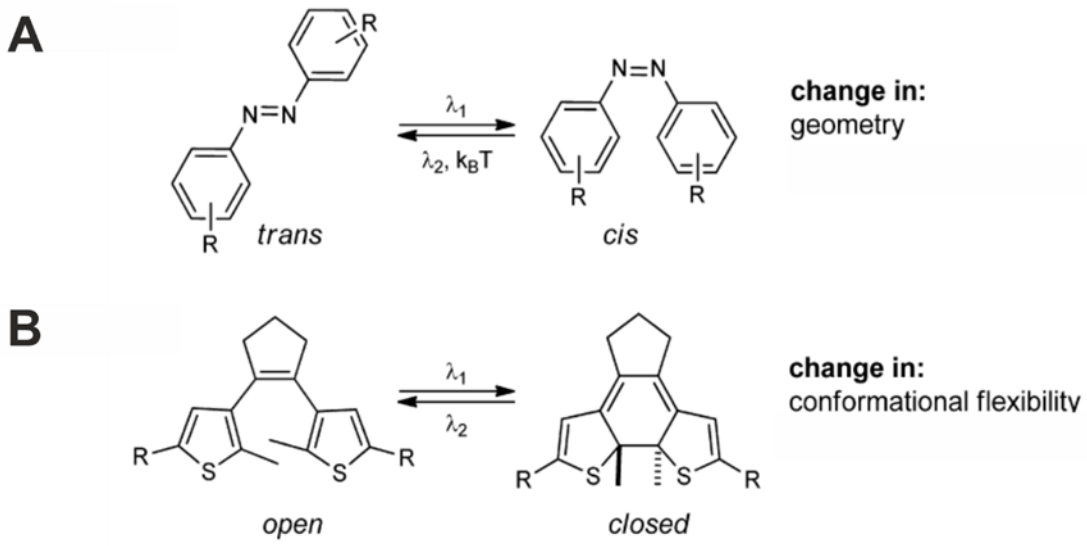

Figure 18 Mechanism of photoswitches. (A) Azobenzene and (B) Diarylethene groups and photoisomerization upon light stimulation. Adapted and reprinted with permission from [121], Copyright 2014 American Chemical Society.

Optogenetics and photopharmacology are two innovative approaches to mitigate the problems associated with wired stimulation techniques. However, one of the biggest downsides of optogenetics is the need to introduce genetically modified vectors of xenographic origin into hosts. This and the introduction of artificial photoswitches might raise concerns about biological safety. Both methods are relatively young and need to prove their potential in long-term applications in humans.

1.5.2 Stimulation with Photovoltaics

General Description of Photovoltaics

Photovoltaic cells convert light energy into electric energy. Thereby, they generate an electrical potential and an electric current when photons are absorbed by certain materials. Photovoltaic devices use semiconducting materials that are mostly based on inorganic chemistry like Si, GaAs, InP, or GaN which form solid crystalline structures. The most prominent example is the use of highly pure silicon wafers in semiconductor production. Group V elements from the periodic table, such as P or As, can be introduced in the crystal lattice to enhance electron mobility. These atoms have a higher number of valence electrons allowing nonbinding electrons to move freely through the material. This process is called doping and results in an n-type semiconductor material. Doping the silicon with group III elements, such as B or Al, results in a p-type semiconductor carrying an electron hole (Figure 19).

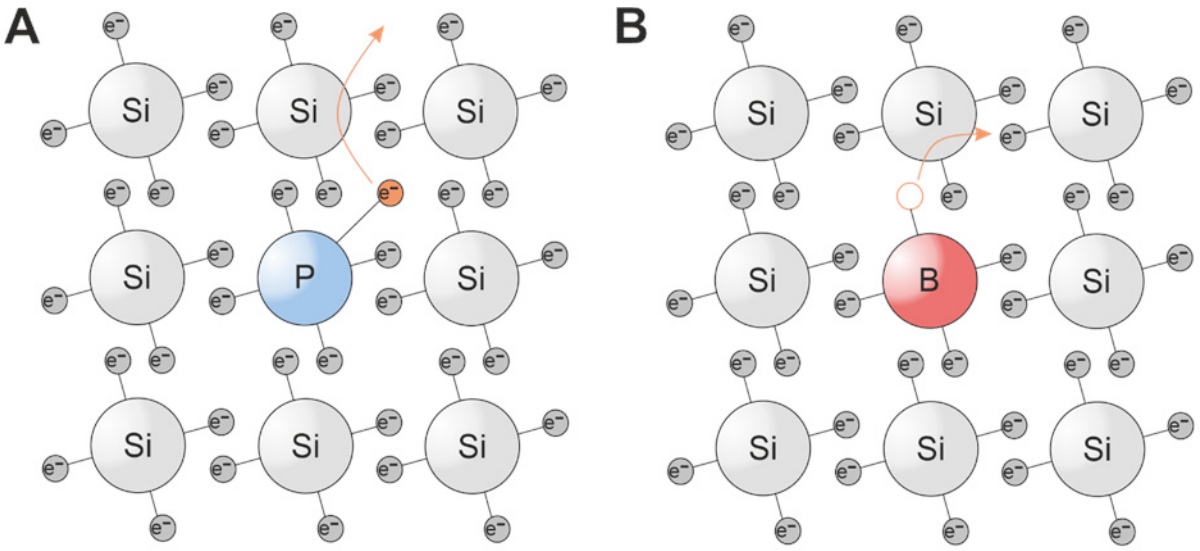

Figure 19 Doping of semiconductors using the example of crystalline silicon. (A) n-type semiconductor with an excess of electrons. (B) p-type semiconductor lacking electrons; depicted as virtual particles diffusing as electron holes.

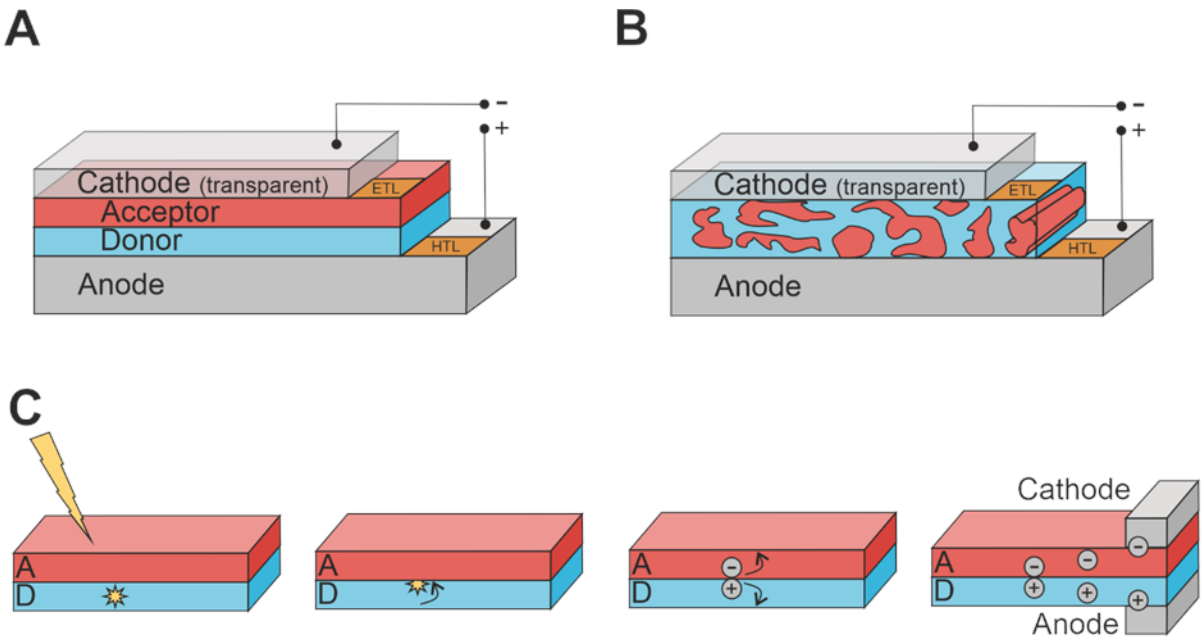

Figure 20 Simplified schematics of photovoltaics. (A) Planar heterojunction between electron donor and acceptor semiconductor layers with an anode and a cathode which is here depicted as a transparent electrode for a facilitated light transmission to the semiconductors; both electrodes might have an extra layer between them and their semiconductor for an improved charge transfer (ETL = electron transfer layer and HTL = hole transfer layer). (B) Bulk heterojunction of mixed donor and acceptor substrates. (C) Working principle of PVs with the stages of (i) light absorption and exciton creation, (ii) exciton diffusion to the junction, (iii) charge separation, and (iv) charge extraction via electrodes.

The development of organic photovoltaics began with pigments [122] such as quinacridone or P3HT (poly(3-hexylthiophene-2,5-diyl) [123] that can form single or multiple heterojunctions [124]. Today, a wide variety of organic materials are used to produce organic photovoltaics. These are arranged in two main configurations forming a planar or a bulk heterojunction (Figure 20 A and B). Bulk heterojunctions use two polymers mixed together, creating a blend of donor and acceptor molecules [125, 126]. A clearly separated junction between both semiconductors is achieved by adding two layers of organic materials on top of each other [127, 128]. Doping of organic semiconductors can also enhance their p- or n-type properties through the oxidation [129] of pigments or the addition of dopants, similar to inorganic PVs, during the manufacturing process [130, 131].

The general working principle for all photovoltaics (PVs) is the same. Photoactive molecules absorb a photon which leads to an excited state. The exciton created during this process diffuses to the junction where the electron and electron-hole pair disintegrates via charge separation into single charge carriers (Figure 20 C) [123]. Compared to their inorganic counterparts made from Si or Ge [132], organic photovoltaics have a disadvantage due to their reduced mobility of charge-carriers. Si-based

PVs form large crystalline lattices compared to the smaller pigment crystals of organic compounds which limits the diffusion length of excitons [133, 134] and therefore reduces the generation of charge carriers [135]. These disadvantages are compensated for by a higher absorption coefficient [123] which allows the production of thinner organic PV devices.

Photocapacitive Stimulation with Organic Electrolytic Photocapacitors

In this thesis, I explore the effect of Organic Electrolytic Photocapaitors (OEPCs) on ion channel gating and neurostimulation. These devices have a thin indium tin oxide (ITO) layer as a back electrode that can cover glass coverslips or be coated on other support materials. On top are two vapor-deposited layers which form the photoactive pixel for the experiments. The planar heterojunction is composed of N,N'-dimethyl perylene tetracarboxylicdiimide (PTCDI) as electron acceptor (n-type layer – Figure 21 C) and metal free phthalocyanine (H_2Pc) as donor (p-type layer – Figure 21 D) [136, 137]. Both OEPC device variants have either a drop-casted PEDOT:PSS ring (Figure 21 A) or a spin-coated layer (Figure 21 B) on top of their surface to increase the volumetric capacitance for cell stimulation.

The red light sources used here are either diffuse radiating LEDs or a focused laser which allows a more precise targeting of the samples. The tissue is relatively transparent for wavelengths between 650 nm

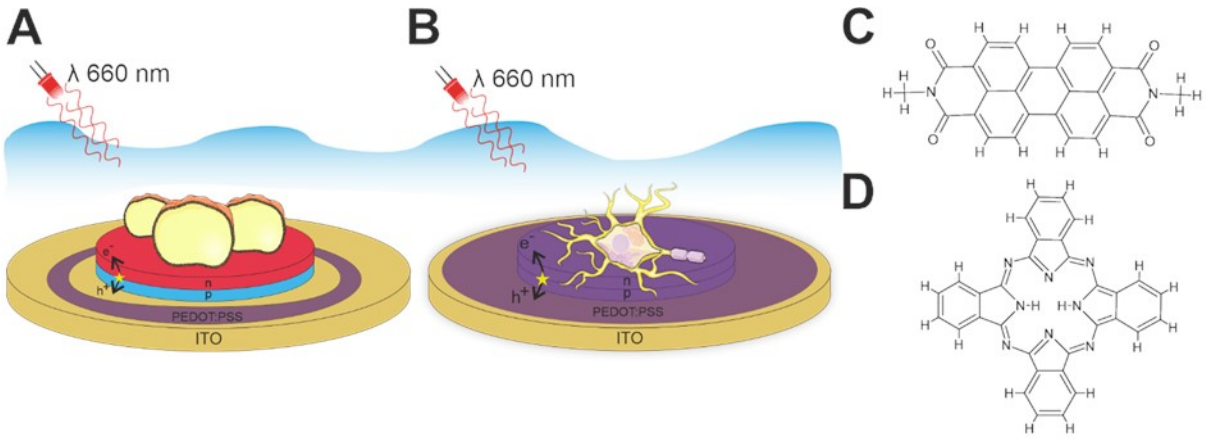

Figure 21 Organic Electrolytic Photocapacitors (OEPC) devices. (A) Configuration with a drop-casted PEDOT:PSS ring on the back electrode or (B) with a spin coated thin layer of PEDOT:PSS on the surface of the whole device to increase volumetric capacitance. (C) N,N'-dimethyl perylene tetracarboxylicdiimide (PTCDI) as electron acceptor (n-type layer). (D) metal free phthalocyanine (H_2Pc) as donor (p-type layer).

and 950 nm as well as for 1000 nm and 1350 nm. The first range is well known from the measurement of blood oxygen levels with red light-driven pulse oximeters whose light can penetrate the skin. OEPCs absorb light in a similar range because of the composition of their photoactive organic pigments.

OEPC devices are electrically free-floating in an electrolytic environment. H_2Pc has a high absorption coefficient, and its absorption peak is between 600 and 800 nm, making this pigment a good choice for light stimuli within the tissue transparency window. The created exciton then diffuses to the heterojunction between both pigments. H_2Pc and PTCDI form well-connected layers that have been shown to not delaminate from each other [136]. PTCDI pigment crystals have a high charge carrier mobility facilitating the transport of electrons.

OEPCs, as photocapacitive stimulation devices, act in a way identical to the capacitive stimulation mechanism described above. Electrons accumulate in the PTCDI layer during charging and a double layer forms between the interface of the n-type layer and the electrolyte (Figure 22). The back electrode becomes positively charged which also induces double layer formation of opposite polarity [137, 138].

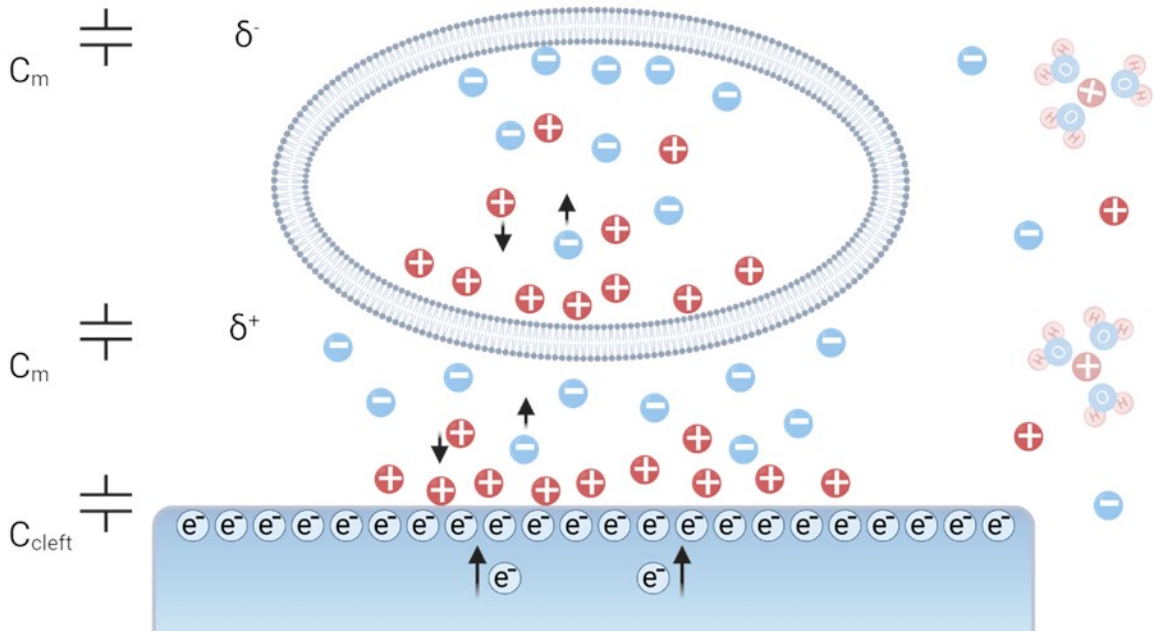

Figure 22 Model of the photocapacitive stimulation mechanism on OEPCs. Formation of a double layer at the interface of the n-type semiconducting pigment and the electrolyte upon light-induced charging. The attached membrane becomes depolarized (less negative on the inside) and the free membrane becomes slightly hyperpolarized according to the two domain model. [47]

The negatively charged semiconductor surface and the positively charged ITO create a transient electric field. When switching the light on, OEPCs create a cathodic stimulation pulse that depolarizes the attached cell membranes (Figure 22) to such an extent that neurostimulation related voltage-gated ion channels can open. The opposite effect occurs when the light is switched off.

Schön, Fromherz, et al. [109, 139, 140] described this behavior with capacitive metal electrodes. They divided the cell membrane into two domains, the membrane patch attached to the stimulation electrode, and the rest that is free floating. The attached membrane becomes less negative on the inside during cathodic stimulation (Figure 22) which gates the ion channels in this area. The free membrane even gets slightly hyperpolarized during electrode charging. The cell membrane polarizes during this short charging period according to Figure 22.

Cathodic stimulation directly depolarizes the attached membrane. Creating an anodic-leading OEPC device through changing the order of the pn-layer could also lead to cell stimulation, since the free membrane would undergo depolarization. However, this would require much higher currents and a potential change due to the larger distance between the electrode and the free membrane.

1.5.3 Photocapacitive Stimulation with 3D-shaped Transducers

Shape of Photocapcacitive Transducers

Organic pigments with semiconducting properties can be used to form planar layers to exploit the photoelectric effect. They are called organic photovoltaics when the layers are connected to an anode and a cathode. As shown above, the same device can be operated without a wired anode and cathode to induce capacitive stimulation on the free-floating device in an electrolytic environment. Another way to use organic pigments is to directly use them as transducers that absorb light and dissipate energy by heating their surroundings.

This heat dissipation is influenced by the shape of the heat transducer. Simulations with quinacridone, a pigment structurally related to epindolidione, showed that planar layers (Figure 23 C) are not as efficient in dissipating heat as spherical objects (Figure 23 B) containing the same pigment molecules. Moreover, the devices showed an increased temperature and a faster heating as well as a faster heat dissipation when the surface of the sphere was structured with micro- to nanoscale needles or plates (Figure 23 A) [103].

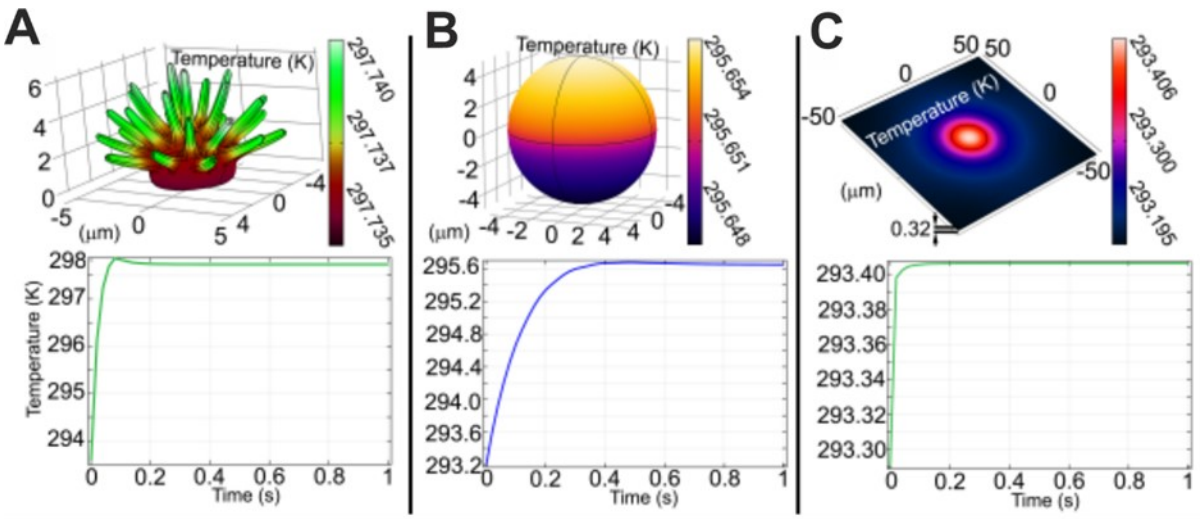

Figure 23 Heating simulations of quinacridone. (A) Microstructured 3D surface, (B) colloidal shape with plane surface and (C) planar pigment surface. Reprinted under the terms of Creative Commons CC BY from the supplementary information of [103].

Direct Capacitive Coupling Stimulation Mechanism with 3D shaped Organic Pigments

The use of 3D-shaped organic pigment semiconductors as chromophores raises the question of how one could influence neuronal signaling by light. Two possible mechanisms [103] have been proposed on how such structures could polarize cellular membranes: direct capacitive coupling and optocapacitance [103].

With direct capacitive coupling, the cell membrane polarizes in a way that is opposite to that of the semiconducting material which is in close contact to the cell membrane. An increase in the interface area between the semiconductor and the membrane could lead to an increased potential for cell depolarization. This can be achieved by microstructuring the surface of the light transducer (Figure 24). However, it is highly unlikely that a charge separation occurs if the semiconducting pigments are not connected to another conductor or semiconducting material. A missing heterojunction interface hinders the charge separation of excitons created by photoexcitation.

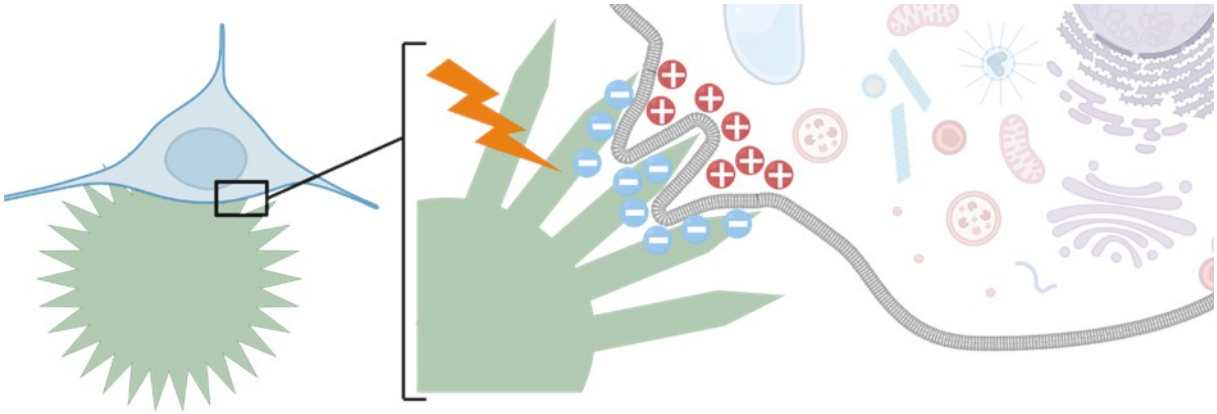

Figure 24 Direct capacitive coupling mechanism. 3D microstructured crystalline pigments attached to a cell membrane under light stimulation. [47]

Photothermocapacitive Stimulation Mechanism with 3D shaped Organic Pigments (Optocapacitance)

Free standing 3D shaped structures that consist of only one semiconducting material are more likely to exhibit faradaic (photocatalytic) or photothermal processes [138]. The photothermal effect describes that the capacity of the cell membrane is directly dependent on the temperature. The capacitance change in the membrane gives rise to capacitive currents which can depolarize the cell membrane. This effect was confirmed in various experiments [116, 141-145] and is not attributed to ionic currents produced by ion channels. The biophysical mechanism of how the membrane capacitance increases due to a change in temperature is under debate [146-148] .

However, the capacitance of the cell membrane increases with higher temperatures, as the surface area of the cell membrane expands and the thickness of the membrane decreases [149, 150] (Figure 25). The change in membrane capacitance through heating causes capacitive currents which is called optocapacitance when the dissipated heat is derived from a transducer that absorbs light directly [151]. The transducer can be water [116] or, in the case of this thesis, organic pigments [103] that attach directly to the cell membrane. A direct measurement of optocapacitive currents is complicated because they overlap with other temperature-sensitive currents measured within experiments, e.g., the activation of temperature-dependent channels [152] or the simple increase of ionic conductance of ion channels in a temperature elevated environment.

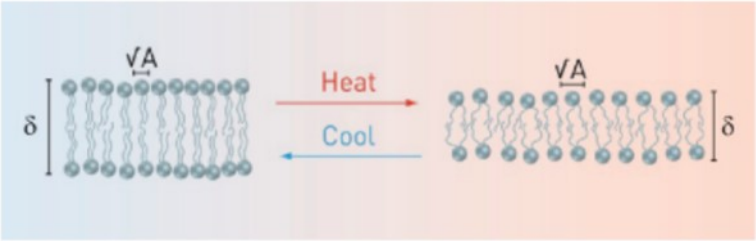

Figure 25 Structural change of a lipid bilayer after heating. The membrane area increases as the thickness of the lipid bilayer decreases. Reprinted with permission from [149], Copyright 2011 American Chemical Society.

The temperature-induced expansion of the membrane is only half the story in understanding the increase in capacitance. The intracellular part of a cell is more negative than the extracellular part. The membrane potential originates from the Nernst potential (see 1.3.1) where e.g., K^+ ions flow out of the cell leading to a net negative charge inside the cell. However, the membrane potential also originates

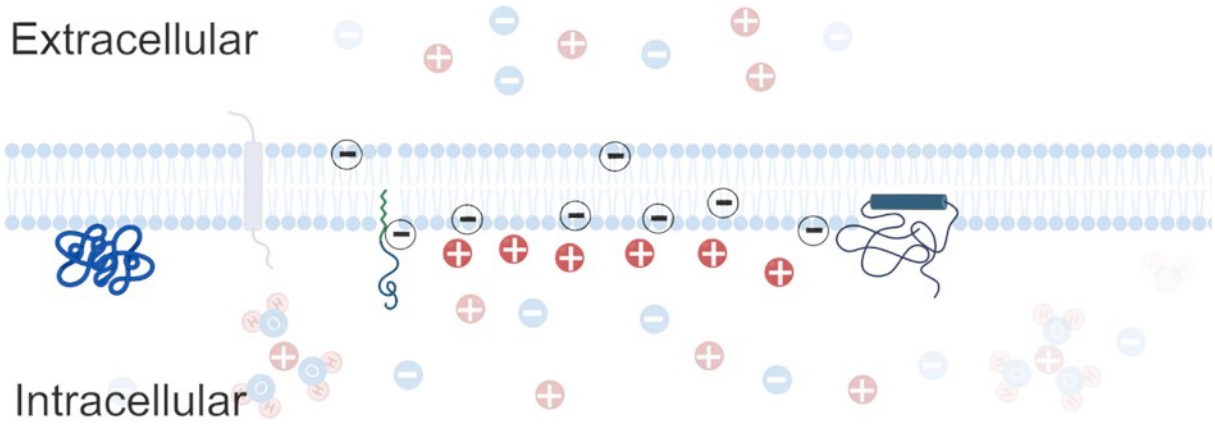

Figure 26 Surface charge potential of a lipid bilayer at resting potential. The inner leaflet of a cell membrane is more negatively charged than the outer one. [47]

from the surface charge potential (V_s) of the lipid bilayer. The phospholipid bilayer has two leaflets that have an asymmetric charge distribution [153, 154]. The inner leaflet contains more negatively charged proteins or molecules [155] that attract positive ions in a very narrow window (Figure 26).

The light absorption of microstructured pigments leads to a temperature increase near the cell membrane which increases the membrane area and its capacitance. This means that the membrane can store more charges, resulting in a capacitive current by the redistribution of charges close to the membrane. This change in V_s leads to a depolarization of the cell [151]. Pinto, Bezanilla et al. show in their mathematical models that effective AP generation requires a rapid change in membrane capacitance to generate a large voltage change [151] for cell stimulation.

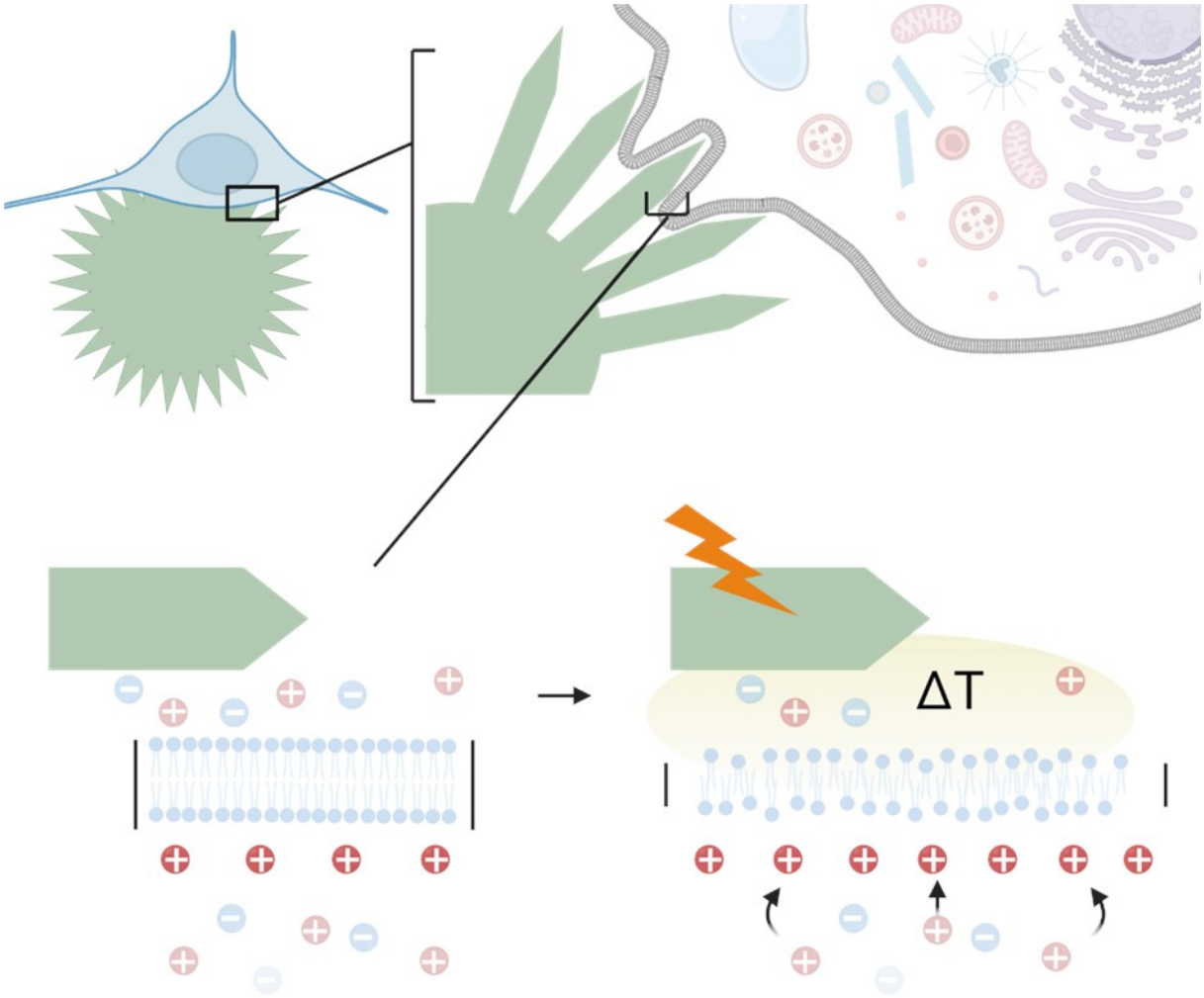

Figure 27 Proposed photothermocapacitive stimulation mechanism. [47]

1.6 Hypothesis and Aims

Optical control of neurostimulation with organic bioelectronics requires an extensive exchange between many disciplines such as neuroscience, material science, membrane biophysics, photonics, electrophysiology, and many more. All communities have their unique communication language and approaches to address similar problems, raising the need for an interdisciplinary strategy.

The main objective of this work is to combine these different disciplines and to explore the potential of organic pigment-based bioelectronics to stimulate neuronal signaling *in vitro*, which can later translate into other *in vitro* or *in vivo* applications that might help to treat neurological pathophysiologies with bioelectronic implants.

Therefore, I examine two novel concepts of light-sensitive stimulation devices and their applicability in terms of cell-device interaction, biocompatibility, activation mechanism, functionality, and reliability. To achieve this goal, we defined several milestones for the thesis:

- Establish new tools and repurpose existing methods by adapting them to the needs that wireless, light-activated stimulation techniques require
- Introduce new model systems in the laboratory to evaluate the effectiveness of bioelectronic devices on *in vitro* applications
- Report new insights back to collaboration partners in material science and neuroscience to improve device prototypes and model systems
- Optimize the interaction between model systems and bioelectronic devices
- Explore the stimulation mechanism with the help of ion channels and the patch clamp technique
- Activate neurostimulation in mammalian neurons with bioelectronics

The shift from classical electronics to organic-based bioelectronics within the last two decades is a paradigm shift in science and for *in vivo* applications. Both disciplines have the intrinsic problem of how to power such devices, since they try to combine artificial technology with biological processes. The use of light as an energy source for bioelectronic devices is a new approach that has become possible only with technological advances in material science and organic chemistry mainly within the last decades. This work introduces two new systems that take advantage of light as an energy source for cell stimulation but differ fundamentally in their underlying activation mechanisms.

2 Materials and Methods

2.1 Thermocapacitive Stimulation

2.1.1 Epindolidione Colloidal Microstructures

The epindolidione microstructures were synthesized and crystallized by the lab of Wolfgang Heiss (Chair of Materials for Electronics and Energy Technology, Friedrich-Alexander-Universität Erlangen-Nürnberg, Germany) [156].

The colloidal crystals were dispersed in 1.6 mg ml^{-1} DMSO (dimethylsulfoxide). Disposable glass capillaries were used to coat the coverslips with the crystals. To prevent clocking or pigment loss due to adhesion of pigments to the glass wear surfaces, the stock solution was diluted 1:1 with DMSO. Each coverslip was coated with 2 - 4 µg cm^{-1} epindolidione. After the evaporation of DMSO, the coverslips were washed with PBS (Phosphate Buffered Saline solution) and distilled water. The coated surfaces were sterilized with 15 min of UV radiation and stored in a dark environment until further use.

2.1.2 Cell Culture and Cell Viability

HEK293 cells (p18 – p35) were cultured in Dulbecco's Modified Eagle's Medium (DMEM) supplemented with 10 % Fetal Bovine Serum (FBS) and splited every 3 days at around 80 % confluency.

Neurons were derived from postnatal rats (Sprague Dawley, Charles River). In summary, the hemispheres of decapitated P0-1 pups were collected, the hippocampi were removed, then transferred to a McIlwain tissue chopper (Mickle Laboratory, UK) and finally cut in 100 µm slices. The tissue was digested in 1 ml of Accutase at 310.15 K for 20 min and then transferred to 5 ml 10 % DMEM in a cell strainer to separate aggregates. The resulting cells were centrifuged (1000 rpm, 5 min) and seeded into dishes with colloidal crystalline epindolidione pigments. The medium was then changed to neurobasal medium with B27 supplement, antibiotics, 5 ng ml^{-1} FGF (fibroblast growth factor), 20 ng ml^{-1} EGF (epidermal growth factor) and glutamine at a final concentration of 0.5 mM. After 4 days of cultivation, the FGF concentration was increased to 10 ng/ml and the cells were used for further experiments.

Cell viability tests were performed for HEK293 cells in 96-well plates. The colorimetric MTS assay CellTiter 96® AQueous One Solution Cell Proliferation Assay (Promega, Germany) was assessed according to the manufacturer's protocol at different time points for each cell type. The luminescence was then measured with a CLARIOstar platereader (BMG Labtech, Germany) at 490 nm.

2.1.3 Scanning Electron Microscopy

For SEM imaging, DIV5-14 neurons on epindolidione coated glass coverslips were washed with PBS and fixed with 2 % paraformaldehyde, 2.5 % glutaraldehyde and 0.1 M cacodylate buffer adjusted to pH 7.4 for 30 – 60 min. For Osmium staining, the glass coverslips were transferred into a container with 4 ml of 2 % OsO_4 solution for 30 min. The OsO_4-cacodylate solution was then removed and dehydration was achieved by a series of 30 %, 50 %, 70%, 80 %, 90 %, 96 % and 100 % ethanol solutions. The coverslips were immersed in the corresponding beaker for 15 min each. The devices were transferred to a 100 % acetone solution and dried with a critical point dryer (BalTec CPD 030, Balzers, Lichtenstein). Sputter coating was then performed in vacuum with prior flushing of the chamber with argon gas in a BalTec SCD 500 (Balzers, Lichtenstein). SEM images were acquired with a Zeis Sigma 500 VP (Zeiss, Germany).

2.1.4 Imaging and Analysis of Dynamic Interactions

Long-term observations of neurite outgrowth towards epindolidione crystals were conducted with a cell observer (Axiovert 200M, Zeiss, Germany). Positions were defined in a 6-well plate and brightfield images were taken every 30 minutes. The images were stabilized with the Fiji image analysis platform [157] and the growth of neurites was traced for each frame with the Simple Neurite Tracer plug-in [158]. The analysis was performed using a Matlab script developed in house [159].

2.1.5 Electrophysiology and Light Stimulation

Patch clamp experiments were performed on an inverted Nikon Eclipse TE300 microscope, with an Axopatch 200B amplifier (Axon Instruments, USA) and a Digidata 1440A (Molecular Devices, USA). Recordings of HEK293 cells attached to the epindolidione microstructure were made at room temperature with a bath solution containing 140 mM NaCl, 5 mM KCl, 1 mM $MgCl_2$, 2 mM $CaCl_2$, 10 mM HEPES and 10 mM glucose adjusted to pH 7.4 with NaOH and an intracellular one containing 145 mM KCl, 1 mM $MgCl_2$, 10 mM HEPES and 10 mM glucose adjusted to pH 7.4 with KOH. For laser stimulation, we used a 10 W solid laser (450 nm) coupled into the optics of the microscope. The self-made laser mount was controlled by an Arduino Genuino MEGA2560 micro controller [159]. Current clamp recordings were performed with I = 0 pA.

2.2 Photocapacitive Stimulation

2.2.1 Device Fabrication

The OEPC devices were produced in the laboratories of Eric D. Głowacki and Vedran Đerek in the Laboratory of Organic Electronics (Linköping University, Sweden), in the Central European Institute of Technology (Brno, Czech Republic) and the Faculty of Science (University of Zagreb, Croatia). Device fabrication for prototypes and single variants might be slightly altered depending on the place of manufacturing and availability of the production equipment on site. In general, the performance of all OEPC devices was evaluated by a standard procedure prior to use.

Cleaning

We used commercially available glass coverslips that already had an ITO coating on one side. They were precleaned in a 323,15 K ultrasonic bath for 15 min each cycle in a series of different solvents: Acetone, Isopropanol, Hellmanex 2 % and DI water. Between each cycle and before solvent change, the glass coverslips were washed with DI water and dried with N_2 (g).

In the next step, the pre-cleaned ITO glass coverslips were placed in a 343,15 K basic piranha solution (150 ml of DI water, 30 ml of ammonium hydroxide and 30 ml of hydrogen peroxide 30%) for 3 min to remove additional organic materials, to etch the surface and to oxidize the metal. After treatment, the coverslips were rinsed with DI water and dried with N_2 (g).

Silanization

To prepare a hydrophobic surface for the further deposition of the pn-layers, the etched ITO was silanized with octyltriethoxysilane (OTS). For vapor deposition, two 30 µl drops were spread into a 30 cm metal box. A plastic spacer held the coverslips approximately 2 cm away from the bottom in place with the ITO side facing towards the OTS. The metal box was then closed and heated to 363,15 K on a hot plate for 2 hours. The hydroxyl groups react with the silicon by a nucleophilic attack forming a monolayer on top of the ITO with hydrophobic octyl groups now covering the surface area (Figure 28). The silanized coverslips were then sonicated in acetone for 15 minutes at 323,15 K, rinsed with isopropanol and dried with N_2 (g).

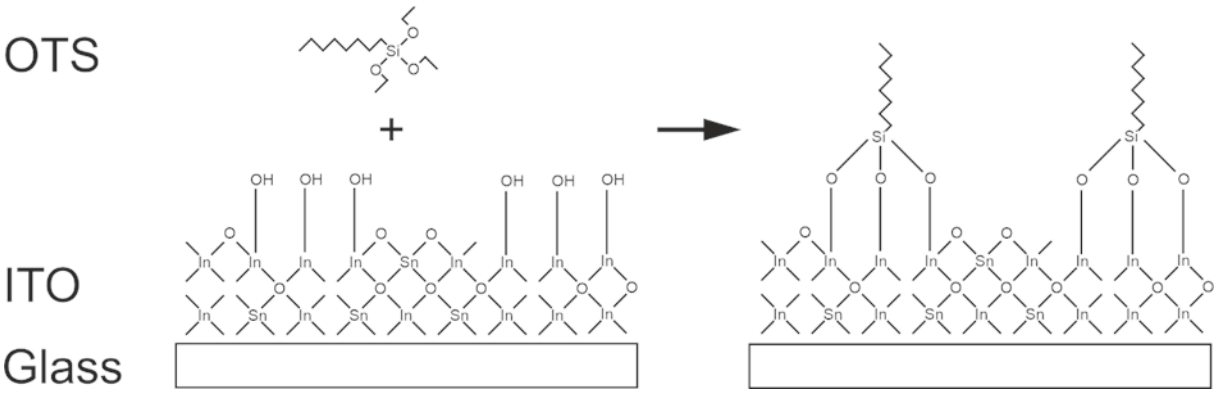

Figure 28 Schematic reaction during silanization. Nucleophilic attack of hydroxyl groups on OTS (dimensions are not to scale).

Physical Vapor Deposition

The pn-layer was deposited via thermal evaporation via physical vapor deposition (PVD). Therefore, the reaction chamber is evacuated to approximately 1×10^{-6} mbar and the crucible containing the organic pigment is heated, releasing molecules into the vapor phase. The high vacuum in the chamber reduces the likelihood of a collision between the vaporized pigments and other molecules present in the atmosphere in the PVD chamber (Figure 29).

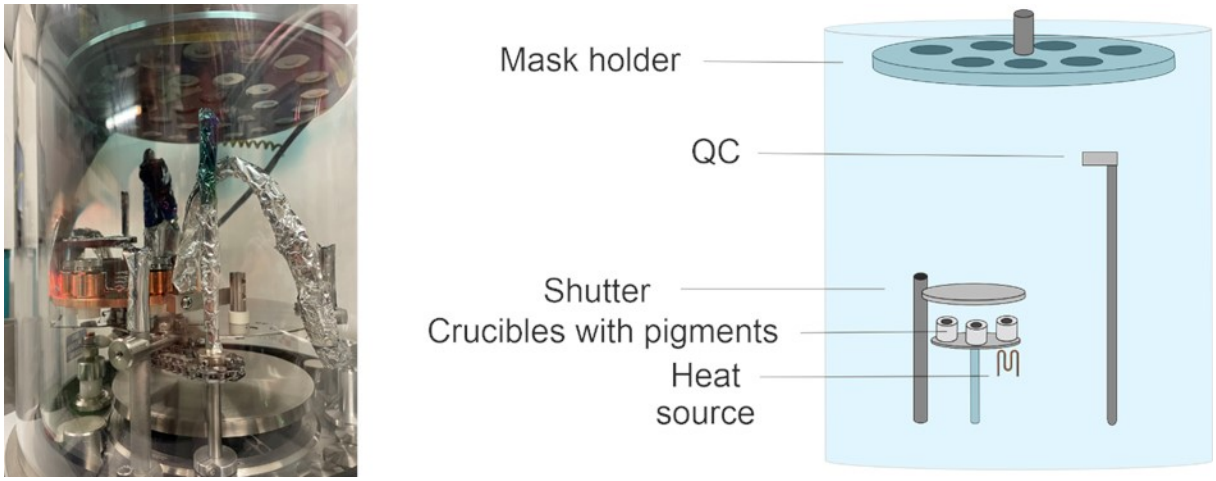

Figure 29 PVD chamber for the deposition of organic pigments. PVD chamber and schematic representation with the rotating mask holder and the inlet for the glass coverslips, quartz crystal for measuring the deposited pigment thickness, crucibles for heating up the pigments and a shutter.

The cleaned and silanized ITO glass cover slips were put into a holder that can rotate around its axis for an even and uniform formation of pigment crystals on its surface. The masks varied in size and shape to define the pixel dot size (e.g. 15 mm, 5 mm and 1 mm) and were mounted into the holder, covering the glass rim which should be protected from vapor deposition.

The first crucible contained the pigment for the p-type layer metal free phthalocyanine (H_2Pc) (Figure 30 A) and was heated by applying approximately 0.5 A to the resistive heating element. After removing the protective shutter element, the evaporated molecules can condensate on the surface of the mask holder forming a thin film of pigment crystals. The evaporation rate can be fine-tuned via the applied current and the deposition rate (~1.6 Å s^{-1}) is monitored by a quartz crystal microbalance. The n-type layer with N,N'-dimethyl perylene tetracarboxylicdiimide (PTCDI) (Figure 30 B) was deposited the same way on top of the p-type layer with 1.9 A current and a deposition rate between 0.5 – 1.6 Å s^{-1}. The film thickness of each layer was set to 20-30 nm.

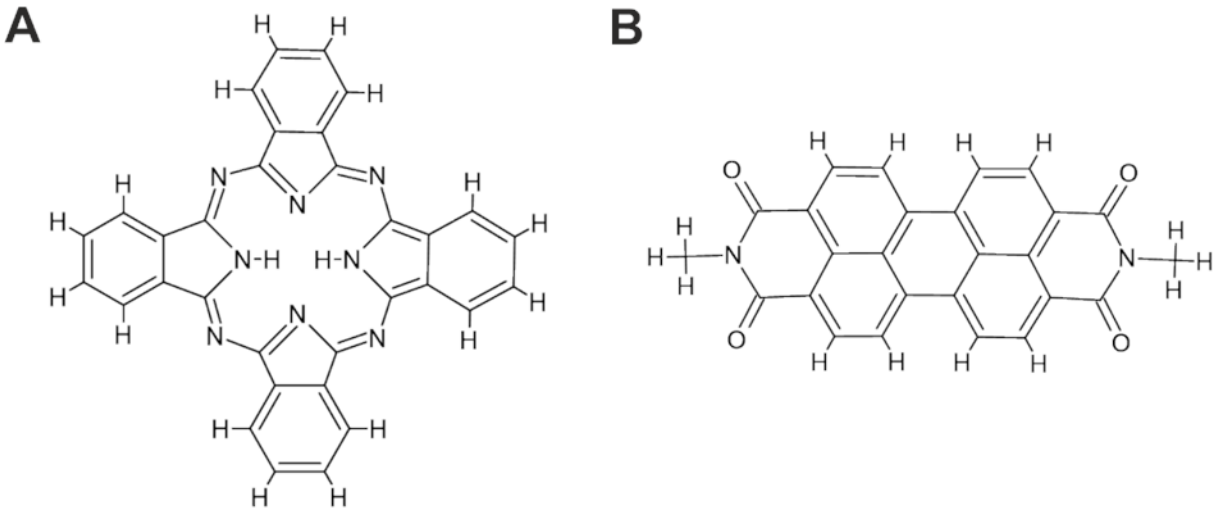

Figure 30 Organic pigments for the photopixel of the OEPC devices. (A) metal free phthalocyanine (H_2Pc) for the p-type layer and (B) N,N'-dimethyl perylene tetracarboxylicdiimide (PTCDI) for the n-type layer.

PEDOT:PSS Coating

PEDOT:PSS is a mixture of Poly(3,4-ethylenedioxythiophene) and polystyrene sulfonate forming a conductive and organic polymer that increases the capacitance of the OEPC device. In this work, two main methods for applying PEDOT:PSS were used. Either a 2-3 mm thick ring was drop-casted on the metal back electrode manually with a pipette or a drop of PEDOT:PSS was placed in the middle of the

OEPC device and then spin-coated by a fast rotating table (~7000 rpm). This results in a thin and even coating on the whole surface of the OEPC device, including the photopixel and the back electrode. The film thickness can be adjusted by the rotation speed.

2.2.2 Device Characterization

The device characterization was performed in the laboratories of Eric D. Głowacki and Vedran Đerek in the Laboratory of Organic Electronics (Linköping University, Sweden), in the Central European Institute of Technology (Brno, Czech Republic) and the Faculty of Science (University of Zagreb, Croatia) in order to ensure constant performance of the OEPCs between batches and production places. For this, the photovoltage and photocurrent were measured with an Ag/AgCl electrode mounted in a syringe filled with 0.1 M KCl. The electrode is connected via the electrolyte to the photopixel during the measurement, while the back electrode is directly connected to the metal of the OEPC device [137].

For the validation of the transient voltages, we used the patch clamp amplifier in voltage clamp mode and the solutions used to patch clamp HEK293 cells (see below). The reference electrode was placed 1.5 cm away from the center of the photopixel and the patch pipette was placed approximately 10 µm to 30 µm above the surface to ensure comparable measurements.

2.2.3 Scanning Electron Microscopy

For SEM imaging, DIV10-21 neurons on OEPC devices were washed with PBS and fixed with 2 % paraformaldehyde, 2.5 % glutaraldehyde and 0.1 M cacodylate buffer adjusted to pH 7.4 for 30 – 60 min. Dehydration was achieved by an ethanol series from 30 %, 50 %, 70%, 80 %, 90 %, 96 % and 100 % by immersing the device into the corresponding beaker for 15 min each. Subsequently, the devices were transferred to a 100 % acetone solution and dried with a critical point dryer (BalTec CPD 030, Balzers, Lichtenstein). The sputter coating was then performed under vacuum with prior flushing of the chamber with argon gas in a BalTec SCD 500 (Balzers, Lichtenstein). SEM images were acquired with a Zeis Sigma 500 VP (Zeiss, Germany).

2.2.4 Cell Culture and Cell Viability

HEK293 Cells

HEK293 cells (p18 – p35) were cultured in Dulbecco's Modified Eagle's Medium (DMEM) supplemented with 10 % Fetal Bovine Serum (FBS) and split every 3 days at around 80 % confluency.

Cells stably expressing the $K_v1.3$ ion channel were generated by linearizing a plasmid containing a TagRFP-$K_v1.3$ sequence from *mus musculus* and a neomycin resistance gene (Figure 31). HEK293 cells were then transfected with Lipofectamine 2000 (Invitrogen, Thermo Fisher Scientific, Inc.) and cultured with G418 (Genetecin) for two weeks to select for cells expressing the plasmid with the resistance gene. Subsequently, they were sorted by FACS analysis (FACS Aria Illu, BD Biosciences, Germany) and st$HEK_{Kv1.3}$ single cell clones of similar RFP brightness were picked and pooled. We used 1 µM PAP-1 (5-(4-Phenoxybutoxy)psoralen) in the growth medium to inhibit ion channel conductance. The inhibitor cannot be washed out. Therefore, the medium was changed to a PAP-1 free medium 4 hours before experiments to allow cells to synthesize new channel proteins.

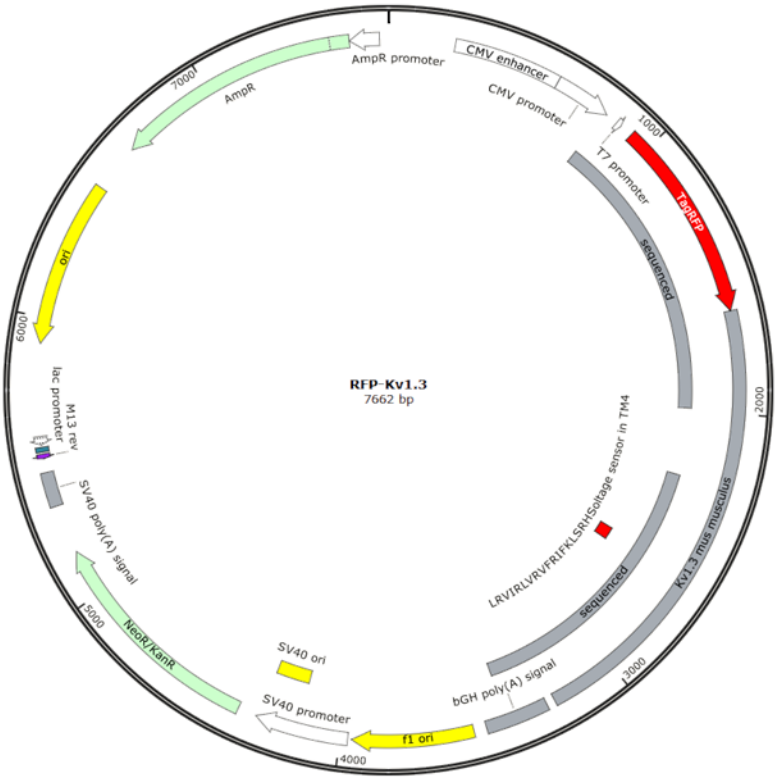

Figure 31 Plasmid map of TagRFP-$K_v1.3$. Schematic representation created with SnapGene (Insightful Science) with a N-terminal His-Tag, a red fluorescent protein, the gene of interest $K_v1.3$ from *mus musculus* and a neomycin resistance gene cassette.

Neurons

Neurons were derived from postnatal rats (Sprague Dawley, Charles River). The preparation differs from the previous one and the process was previously described [20, 160]. In summary, the hemispheres of decapitated P0-1 pups were collected in an ice-cold solution containing 137 mM NaCl, 5.4 mM KCl, 1.1 mM Na_2HPO_4, 1.1 mM KH_2PO_4 and 6.1 mM glucose adjusted to pH 7.3; in addition we also added 1:100 100 mM kynurenic acid to the solution. The hippocampi were separated and transferred to a papain solution (25 U ml^{-1}) for a maximum of 30 min at 310.15 K. The tissue was disintegrated by gentle up and down pipetting and a series of pipettes becoming smaller before seeding the cells into glass rings sitting on poly-D-Lys coated glass coverslips or OEPC devices. After being attached to the surface, the medium was changed to a DMEM medium with high glucose (4.5 g l^{-1}), 10% FBS and a nutrient solution.

Cell Viability

Cell viability tests were performed for HEK293 cells in 24-well plates and neurons in 96-well plates containing glass coverslips as control or OEPC devices with an appropriate diameter. The colorimetric MTS assay CellTiter 96® AQueous One Solution Cell Proliferation Assay (Promega, Germany) was assessed according to the manufacturer's protocol at different time points for each cell type. The luminescence was then measured with a CLARIOstar platereader (BMG Labtech, Germany) at 490 nm.

2.2.5 Electrophysiology

Patch clamp experiments were performed on an inverted Olympus IX70 microscope, with an Axopatch 200B amplifier (Axon Instruments, USA) and a Digidata 1440A (Molecular Devices, USA). The patch pipettes were pulled on the micropipette puller P-1000 (Sutter Instruments, USA) from thin glass walled capillaries 30-0068 for HEK293 cells and thick-walled capillaries 30-0060 for neurons (Harvard Apparatus, USA). The recordings were performed at room temperature. We also used an insulating bath chamber made from polytetrafluoroethylene and an Ag/AgCl electrode as a reference electrode. For perfusion experiments, we used a chamber from NGFI (Graz, Austria).

HEK293 and st$HEK_{Kv1.3}$

The bath solution for HEK293 cells contained 140 mM NaCl, 5 mM KCl, 1 mM $MgCl_2$, 10 mM HEPES and 10 mM glucose adjusted to pH 7.4 with NaOH and the intracellular one contained 145 mM KCl, 1 mM $MgCl_2$, 10 mM HEPES and 10 mM glucose adjusted to pH 7.4 with KOH.

Neurons

The bath solution for neurons contained 140 mM NaCl, 2.5 mM $CaCl_2$, 2 mM $MgCl_2$, 2 mM KOH, 10 mM HEPES and 10 mM glucose adjusted to pH 7.4 with NaOH and the intracellular one contained 3.5 mM NaCl, 1.5 mM $CaCl_2$, 0.25 mM $MgCl_2$, 10 mM HEPES, 120 mM D-gluconic acid potassium salt, 1.5 mM D-gluconic acid sodium salt and 5 mM EGTA (3,12-Bis(carboxymethyl)-6,9-dioxa-3,12-diazatetradecane-1,14-dioic acid) adjusted to pH 7.3 with KOH. In contrast to HEK293 cells, neurons were recorded with a perforated patch using amphotericin B (250 µg ml^{-1}) that was added to the pipette solution shortly before the experiment. We further used 0.5 µM TTX (tetrodotoxin) in the bath solution for experiments blocking the voltage-gated sodium channels.

Light Stimulation and Patch Clamp Protocols

During the experiments different methods for light stimulation were used. We used either a 10 W LED (660 nm, Roschwege, Germany) collimated (Figure 32 A) from the top or mounted on the objective revolver from the bottom (Figures 32 B and C). Neurons on OEPC devices were primarily stimulated with a 700 mW diode laser (638 nm, Lasertack, Germany).

The voltage clamp and current clamp protocols are indicated in the results section corresponding to each experiment and figure. Neuronal stimulation recordings in current clamp were performed with I = 0 pA.

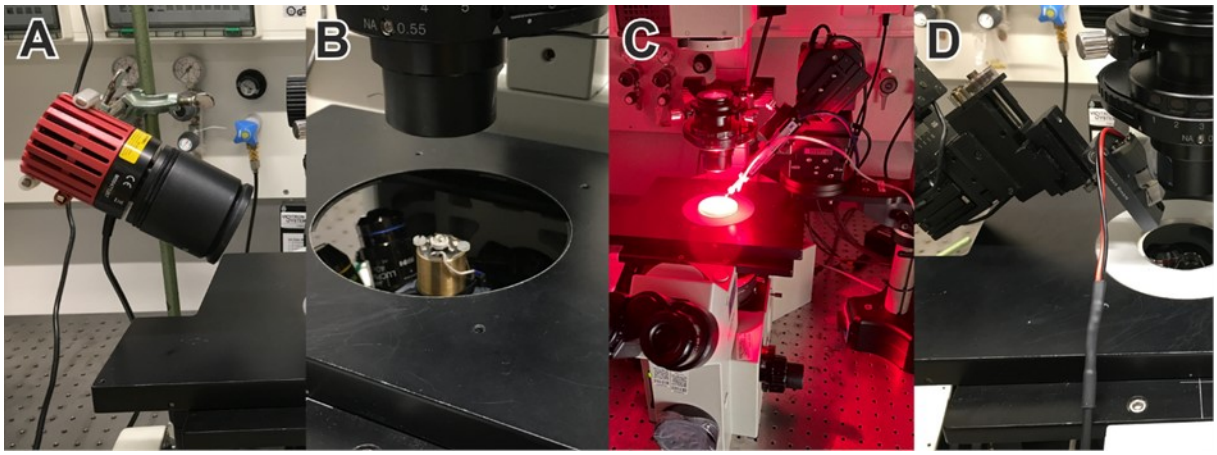

Figure 32 Light sources for OEPC stimulation. (A) Collimation of a 10 W LED from the top. (B) and (C) bottom illumination (660 nm) with a 10 W LED mounted on an objective revolver. (D) Laser illumination with a 700 mW diode laser (638 nm).

2.2.6 Confocal Microscopy and Cell Membranes

Staining cell membranes of HEK293 was achieved by transfecting the cells transiently with mTagRFP-Membrane-1 (Addgene plasmid # 57992). Z-stacks of 12-bit images were taken with a confocal microscope (A1R, Nikon, Japan) using a Plan Apo 40x/0.95 objective (Nikon, Japan). Further imaging parameters were set to: pixel dwell time of 1.1 µs, pixel size = 0,31 µm/px, Z-step = 0.374 µm and 4 times averaging. For 3D convolution, mesh generation and surface area calculation, the Amira software 6.5.0 (Thermo Fisher Scientific) was used.

3 Results

3.1 Thermocapacitive Stimulation with Homogen Colliodal Pigment Crystals

Photostimulation requires a light-sensitive acceptor in the cell or in proximity to convert the energy into a stimulus. The introduction of photoactive ion channels or chromophore-containing proteins means an alteration of the cell's genetic code. This is relatively easy to achieve for *in vitro* cell culture, but more complicated to realize for *in vivo* applications. In this thesis, I tested a photosensitive molecule as an alternative that dissipates heat after light absorption and depolarizes the cell membrane. This molecule is a pigment that can form a 3D-shaped macromolecular crystals during chemical synthesis.

3.1.1 Stability of Crystalline Microstructures and Cell Attachment

Epindolidione Crystals

Epindolidione molecules form round microstructures with diameters between 5 µm to 10 µm. They are subdivided into dozens of continuous plates of the crystalline pigments (Figure 33 A) that further increase the surface area. The working hypothesis was that a large and structured surface area provides many interaction sites for the cell membrane to attach to.

The microstructures are dispersed in an organic solvent (DMSO). Storage vials were carefully inverted or vortexed to prevent clumping. The microstructures were then pipetted onto glass coverslips. The general majority adhered to the glass surface while the solvent evaporated. Careful rinsing with water washed away an estimated 20 % of the structures. SEM images show that the remaining pigment crystals cluster in larger groups with loose contacts to other organic crystals (Figures 33 B-D). Neither a dilution of the crystalline pigments (1.5 mg ml^{-1} to 0.15 mg ml^{-1}) in DMSO, nor an accelerated evaporation of the solvent prevented the observed clustering on the coverslips.

In vitro Cell Culture

Initial experiments suggested a strong attachment of HEK293 cells to the microstructures. Cells in solution seeded into dishes randomly attached to the glass coverslips and the microstructures (Figure 34 A). The cells were observed to displace microstructures when the culture grows confluent (Figure 34 B). Furthermore, there was no indication that the cells internalized whole structures or parts of the pigments. The crystals, however, detached from the glass substrate as soon as they got in

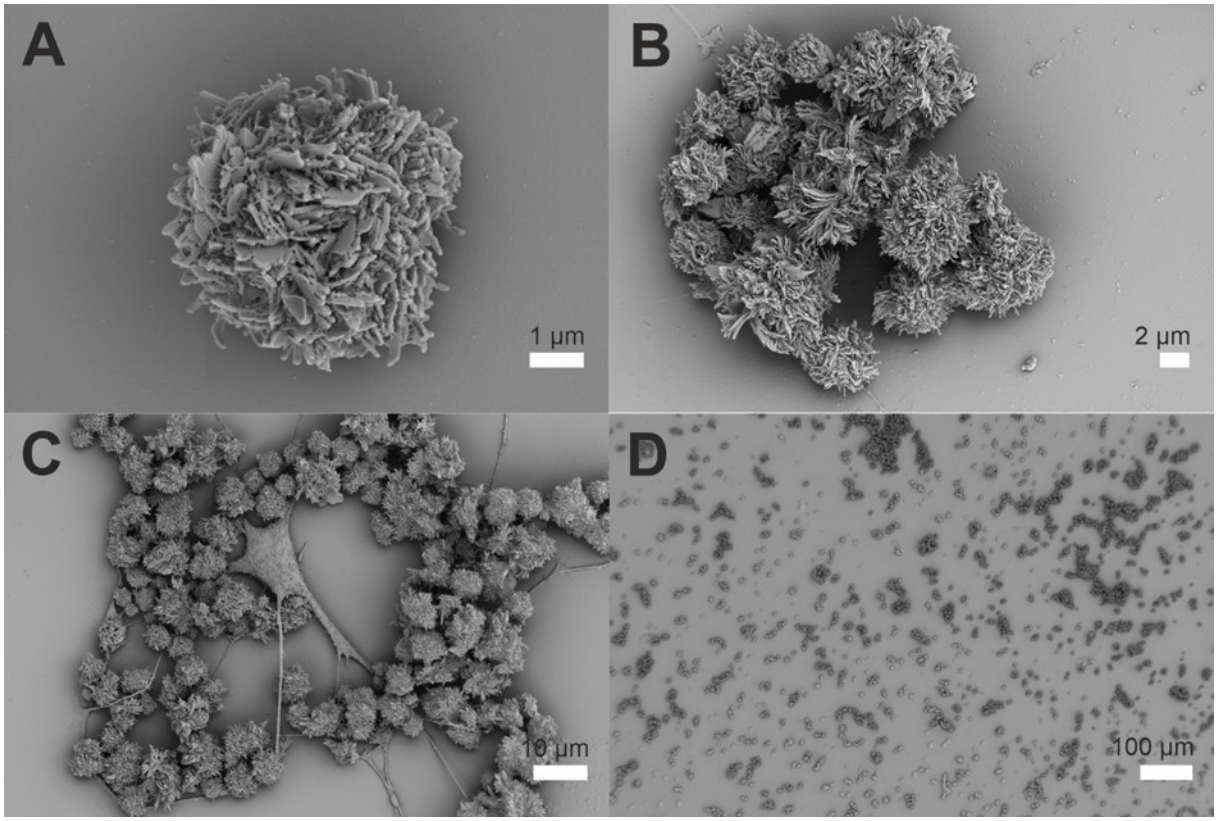

Figure 33 Representative SEM images of epindolidione pigment crystals. (A) Single round microstructure with platelets. (B) and (C) microstructures clustered together on glass coverslips. (D) Overview of the distribution between single particles compared to clustered ones (unpublished data).

contact with a cell membrane. Similar observations were also made with neurons. They matured in cell culture for up to three weeks without problems (Figure 34 C). The microstructures did not detach or disintegrate in the electrolytic medium during long-term cultivation. Only cell membranes were able to detach the microstructures from the glass.

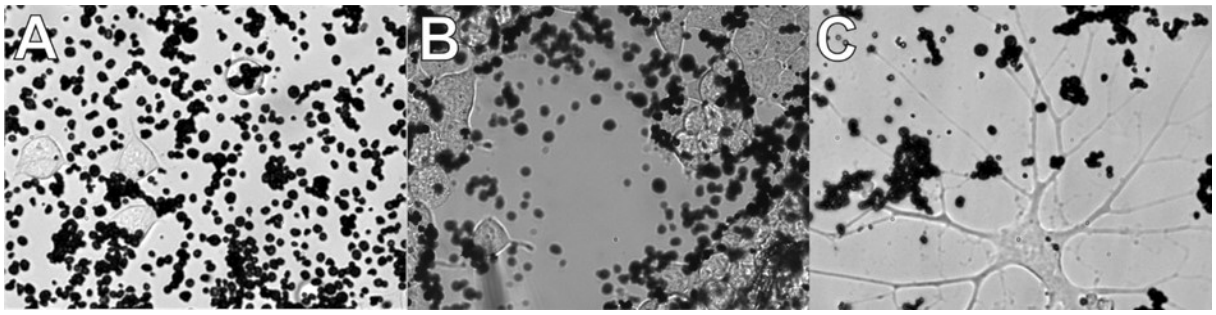

Figure 34 Representative brightfield images of epindolidione pigment crystals with (A) and (B) HEK293 cells or (C) neurons (unpublished data).

Cell Attachment

The detachment of the microstructures could be explained by further SEM imaging. Cell membranes of spherical HEK293 cells (Figure 35 F) or neuron somata (Figures 35 D and E) fuse together with microstructures when they come into close contact with each other. The cell membranes grow over the pigment plates and adapt their shape according to the 3D structure of the pigment crystals. This creates a large interaction site where both surfaces can bind firmly to each other.

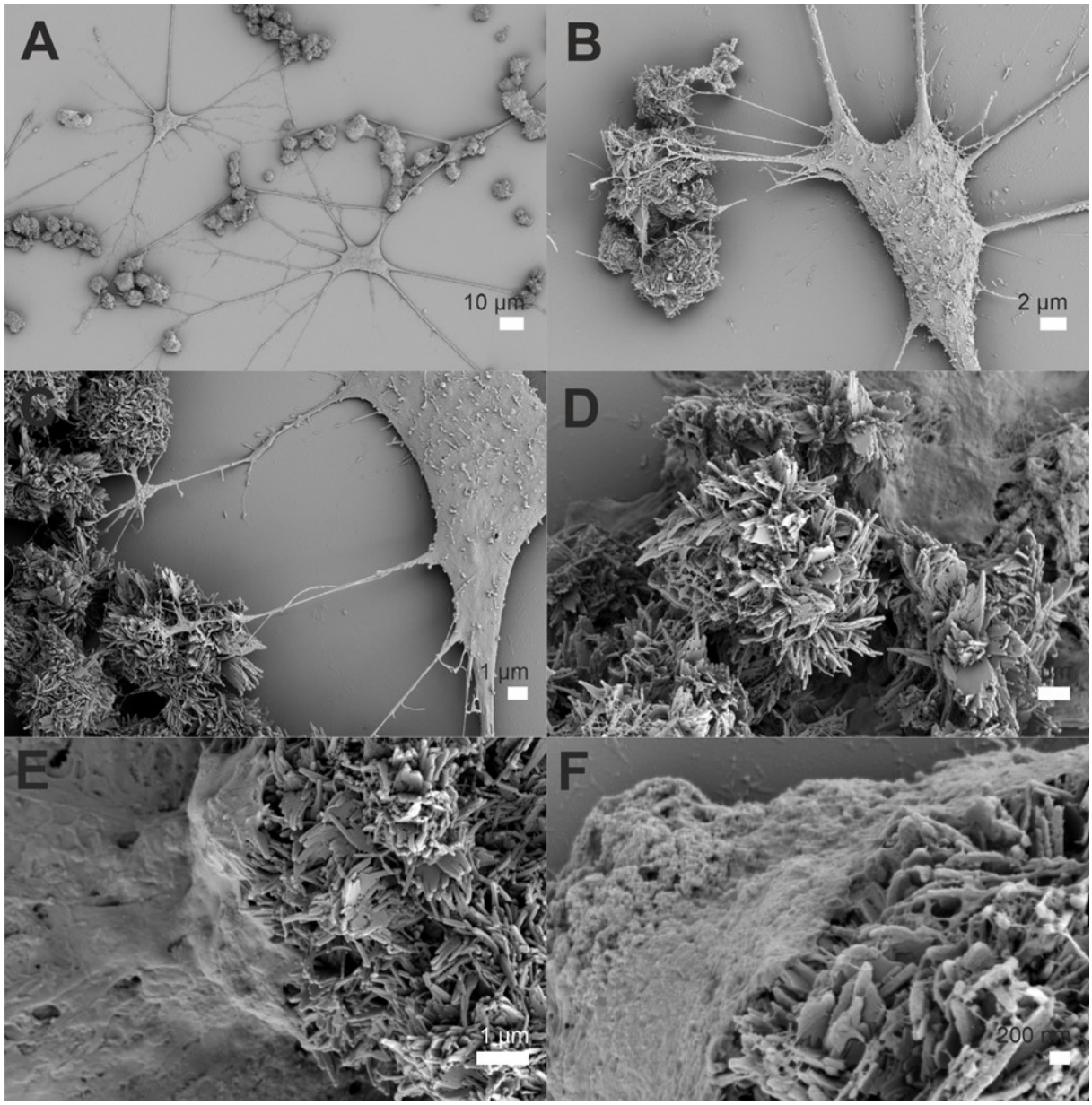

Figure 35 Representative SEM images of epindolidione pigment crystals with cells. (A) – (E) Primary hippocampus neurons from *Rattus norvegicus* (P0-1) that establish an interconnected network between cells and outgrown dendrites to pigment microstructures. (F) Cell membrane of a HEK293 cell that grows over the epindolidione platelets (unpublished data).

Another observation was the outgrowth of neurites and dendrites toward microstructures. Neurons established a regular network of cell interactions (Figure 35 A), but they also established extensive connections to the pigment surfaces (Figures 35 B and C).

3.1.2 Dynamic Interactions between Crystalline Microstructures and Neurons

Further long-term live cell experiments were conducted on a cell observer to investigate the dynamics between the neurite growth and the interaction with the microstructure surface. Neurons were seeded on glass coverslips coated with epindolidione and the maturation process was imaged. Brightfield images were automatically made every 30 minutes on a microscope with an incubation chamber covering the probe.

The neurons establish a neuronal network by growing neurites in all directions. They interact with neighboring cells by connecting to their membranes or by reorganizing the growth direction. Since the neurons were sparsely seeded in the *in vitro* cell culture, one could observe a high mobility and a great number of events, when neurites attached or retracted from and to the pigments (Figure 36 A). The median retention time of 9 neurons was 14.8 h while 4 neurites exhibited two binding events on different spots (Figure 37).

We traced the outgrowth of single neurites with a semi-automated approach by measuring the trajectory in an X-Y coordinate system. We defined the end point of the growth cone and plotted its position for a representative neuron over a 72 h time course (Figure 36 B). In this case, the neurite connected to a microstructure (Figure 36 A and B – t = 9 h orange) and remained attached for 6.5 h. We further calculated the relative dynamic of the growth cone compared to its previous positions (Figure 36 C – orange). The dynamic in this area is less than 5 µm (8 pixel) in both axes and within the error margins for the semi-automated tracking approach. The neurite retracted then from the microstructure after 20 h which correlates with a higher dynamic (Figure 36 C – green) until the neurite binds to another epindolidione pigment (indicated in red) (Figure 36 A – C).

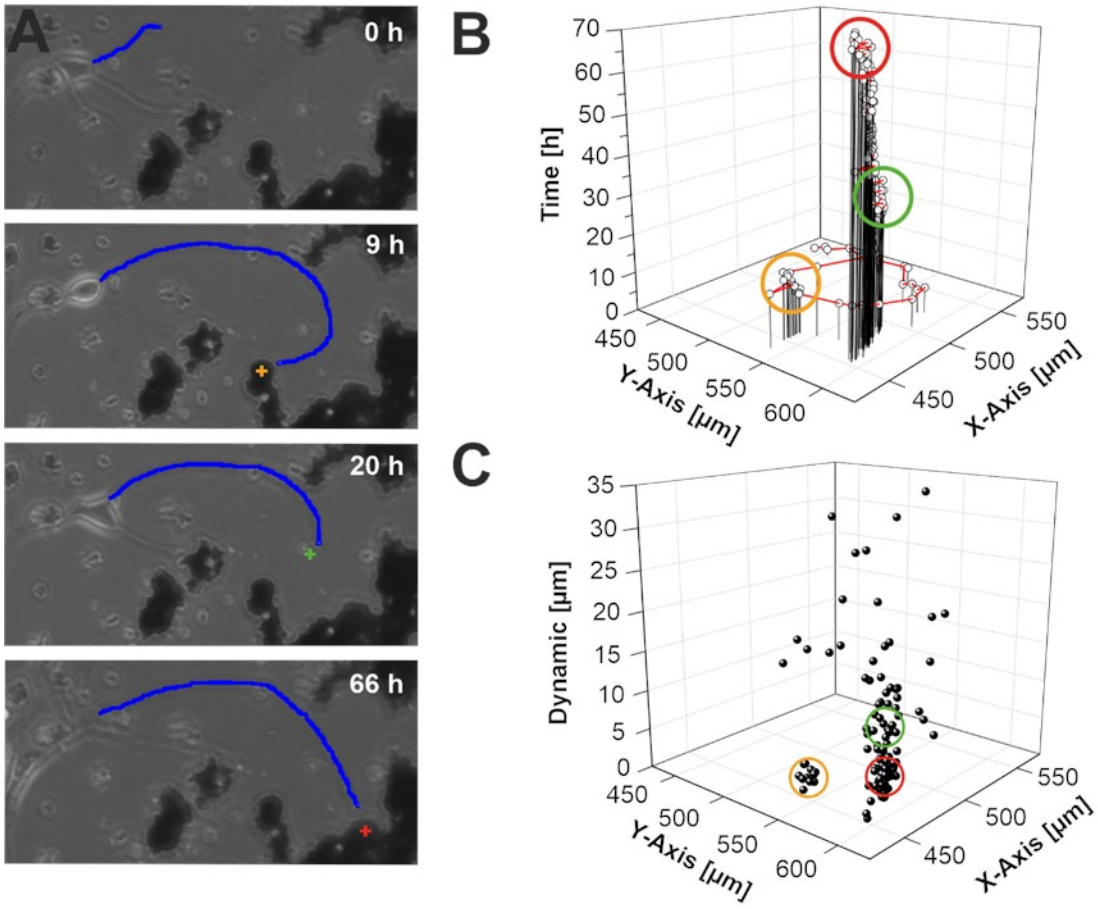

Figure 36 Dynamic of neurite growth and interactions with epindolidione. (A) Brightfield imaging of neurons seeded on glass coverslips coated with microstructures over time and the neurite trajectory in blue. (B) End points of the neurite in space (X-Y axis) plotted over time. (C) End points of the neurite in space (X-Y axis) plotted over the dynamic change compared to the previous coordinates. Orange, green and red crosses indicate the position. Circles highlight the corresponding data points (representative analysis - unpublished data).

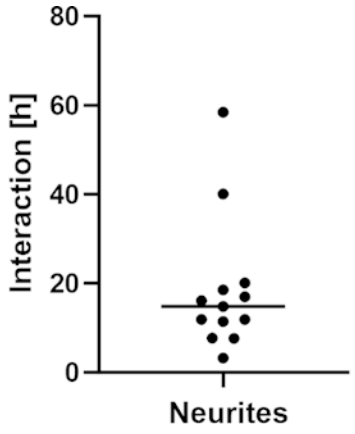

Figure 37 Retention time of neurites attached to epindolidione microstructures. Single datapoints of 9 neurons with 13 binding events within 72 h (unpublished data).

3.1.3 Light Stimulation and Cell Viability

Experimental Set-up

In the next step, we evaluated the effect of light stimulation on membrane depolarization. A self-constructed laser (450 nm) was coupled into the optics of the microscope and focused to a spot size (5 - 10 µm) similar to the diameter of the epindolidione microstructures (Figure 38 B – arrow). Cells that had two or more pigments attached were chosen for electrophysiological experiments (Figure 38 A). The adhesion between cells and microstructures varied for each measurement. Some pigments were washed away when approached with the patch pipette which was under a slight overpressure.

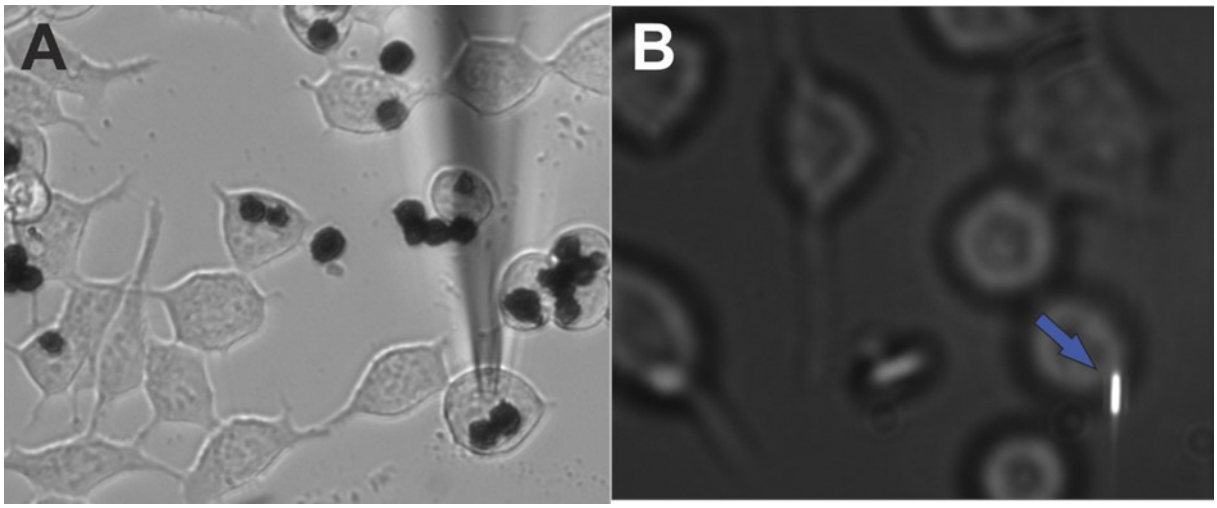

Figure 38 HEK293 cells with epindolidione microstructures. (A) Single cells attached to pigment structures. (B) Laser spot (460 nm) focused to the plane of epindolidione microstructures (unpublished data).

Patch Clamp Experiments

We tested three different light pulse length conditions with a laser light intensity between 0.2 and 1 mW μm^{-2}. The membrane of HEK293 cells depolarized with a median of Δ 4.5 mV for 50 ms and 100 ms pulses (Figure 39 A). There is no significant difference in height between pulse amplitudes, but membrane depolarization remained constant during light stimulation (Figure 39 B). When the membrane is voltage-clamped to the resting potential of the cell, we could record transient capacitive peaks with opposite directions when the light is switched on and off (Figure 39 C). A slight current increase was recorded during the pulses of longer stimulations (50 ms and 100 ms). However, the height of the transients remained relative constant. Some noise was introduced by the nearby electronics of the laser set-up.

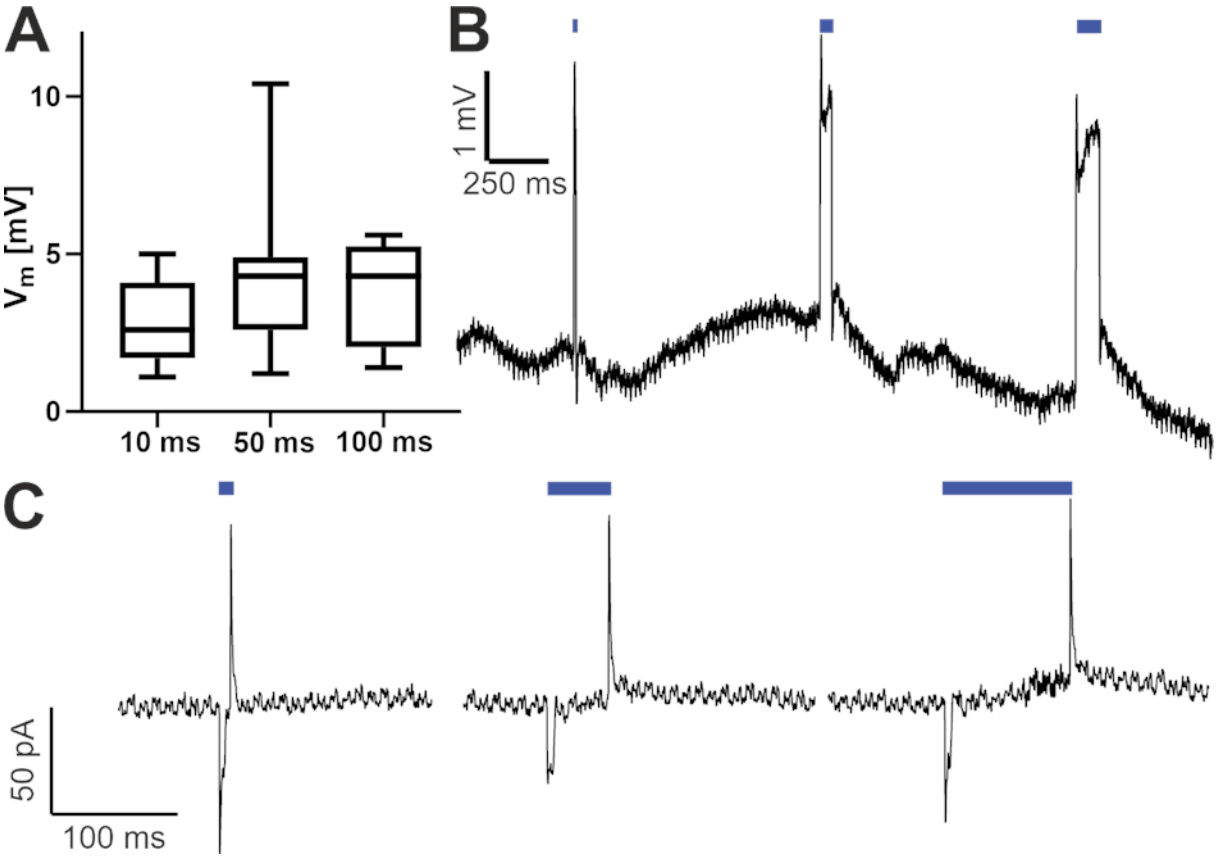

Figure 39 Light stimulation of epindolidione microstructures attached to HEK293 cells. (A) Overview of the median membrane depolarization for 10 ms (0.2 mW µm^{-2}), 50 ms (1 mW µm^{-2}) and 100 ms (1 mW µm^{-2}) with a 450 nm laser (N = 7) and (B) a representative trace in current clamp. (C) Corresponding voltage clamp measurements to (B) (unpublished data).

Cell Viability

The small laser spot was carefully aligned to hit the epindolidione microstructures. Some HEK293 cells bursted during light stimulation due to high laser intensities, despite avoiding hitting the cells directly with the laser spot. Lower intensities, however, resulted in weaker cell membrane depolarization.

In cell culture, it was observed that proliferating HEK293 cells were more likely to die, when attached to epindolidione structures compared to controls. This effect was not observed in maturating primary neurons. Therefore, we tested the cell viability of HEK293 cells on epindolidione with an MTS assay that showed a significantly reduced cell viability (Figure 40). When interpreting these data, one must be careful, since the absorption of epindolidione precursor molecules, dispersed single molecules, and colloidal microstructures varies significantly [156]. The absorbance of colloidal pigment crystals shifts to a peak maximum at 490 nm with a broad absorption spectrum adjacent to it. The reaction of the assay converts the MTS to formazan. The absorption of this formazan dye is then measured at 490 nm. Whether the epindolidione pigments slowly dissolve or disperse might be to debate.

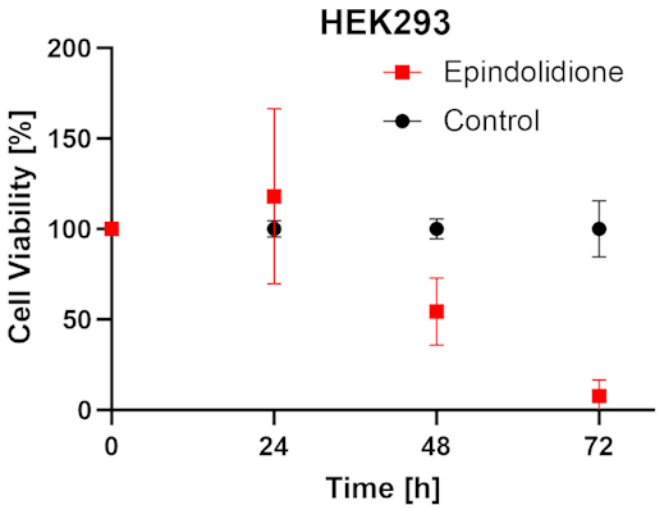

Figure 40 Cell viability of HEK293 cells attached to epindolidione microstructures. HEK293 cells on colloidal epindolidione crystalline pigments (red) and a control condition with cells seeded in well plates (black) with n = 3 (unpublished data).

3.2 Photocapacitive Stimulation with Organic Pigment Semiconductors

Organic Electrolytic Photocapacitors have a fundamentally different device architecture compared to the microstructured epindolidione crystals. While the latter devices might be superior to the planar design of OEPCs in terms of cell interaction, a photocapacitive stimulation mechanism might be more effective for neurostimulation than a thermocapacitive one. In this part of the thesis, I will explore the interaction between cells and OEPCs, as well as the potency and the principal mechanism of the stimulation mechanism.

3.2.1 Scanning Electron Microscopy

Strong attachment of cells to the OEPC devices is very important for successful photocapacitive stimulation. A rather small cleft region between the cell membrane and an OEPC minimizes the decay of the surface potential within the electrolytic environment. During this PhD project, many different cell types were tested for their potential to be stimulated, e.g., HL1 cells, RBL cells, or rodent cardiomyocytes. Especially, cell culture cell lines tend to adhere strongly on a huge variety of surfaces without further coatings that mimic the extracellular matrix such as polymers like poly-Lys or laminin. These agents would further increase the cleft region to the cell membrane. HEK293 cell culture cells, in particular, demonstrated a strong and robust attachment to the crystalline pigments of the n-type layer. In contrast to cell culture cell lines, primary cells mostly need a completely different environment for growth and maturation. Like whole tissues, isolated heart muscle cells did not adhere at all to the commonly used surfaces in cell culture. Neuronal cells, however, need a surface coating for a solid attachment, but together with feeder or glial cells, they form a tight connection between each other and exhibit a narrow cleft to the attached surface. The aim of the following paragraphs is to evaluate the attachment of HEK293 cells and hippocampal neurons from rats to different surfaces of OEPC devices.

Surfaces of OEPC Devices

In all experiments, we chose two different surface conditions to seed cells on. HEK293 cells were seeded directly on the crystalline surface of the PTCDI pigments that constitutes the top layer of the OEPC device (Figure 41 A). Neurons, however, were seeded together with glia cells on top of a spin-coated PEDOT:PSS layer, covering the whole OEPC. The surface received a poly-D-Lys treatment prior to cell seeding (Figure 41 B).

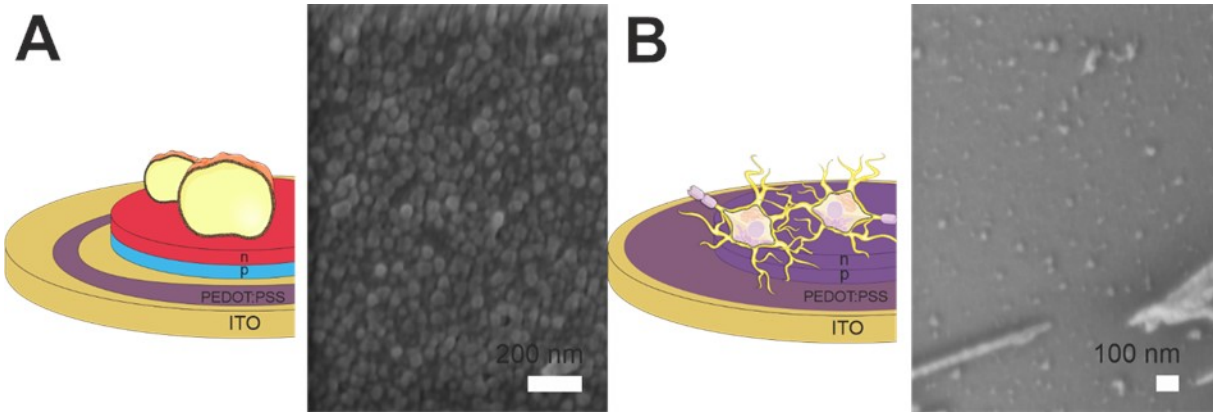

Figure 41 Overview of different OEPC surfaces. (A) SEM imaging of the crystalline PTCDI surface of the n-type layer. (B) SEM imaging of the spin-coated PEDOT:PSS surface together with poly-D-Lys (representative images). PEDOT:PSS is indicated in purple in the schematic illustration, N,N'-dimethyl perylene tetracarboxylicdiimide (PTCDI) as electron acceptor (n-type layer) is indicated in red and metal free phthalocyanine (H_2Pc) as donor (p-type layer) is indicated in blue.

HEK293 on n-type Crystalline PTCDI Pigments

We decided to seed single HEK293 cells directly onto the photoactive surface of an OEPC device variant consisting of an ITO layer, a p-type layer and an n-type layer (bottom to top). Single cell contacts were monitored with scanning electron microscopy.

The dehydration steps during the preparation of the SEM samples seem to have a negligible effect on cell morphology. Since the cells were seeded 1-3 h before preparation, one can observe round cell shapes (Figure 42 A). The filopodia grew radially in all directions (Figures 42 B and D) and the somata attached directly to the crystalline surface of the PTCDI n-type layer pigments (Figure 42 C). Even when dehydration artifacts and cell shrinkage are considered, most of the cell membranes are in close contact with the OEPC surface. In some cases, we even observed a rapture of the photo layer caused by cell shrinkage under harsh preparation conditions, indicating that the strong adherence between the membrane and the OEPC surface is more powerful than the strong adherence between the pn-layer and ITO.

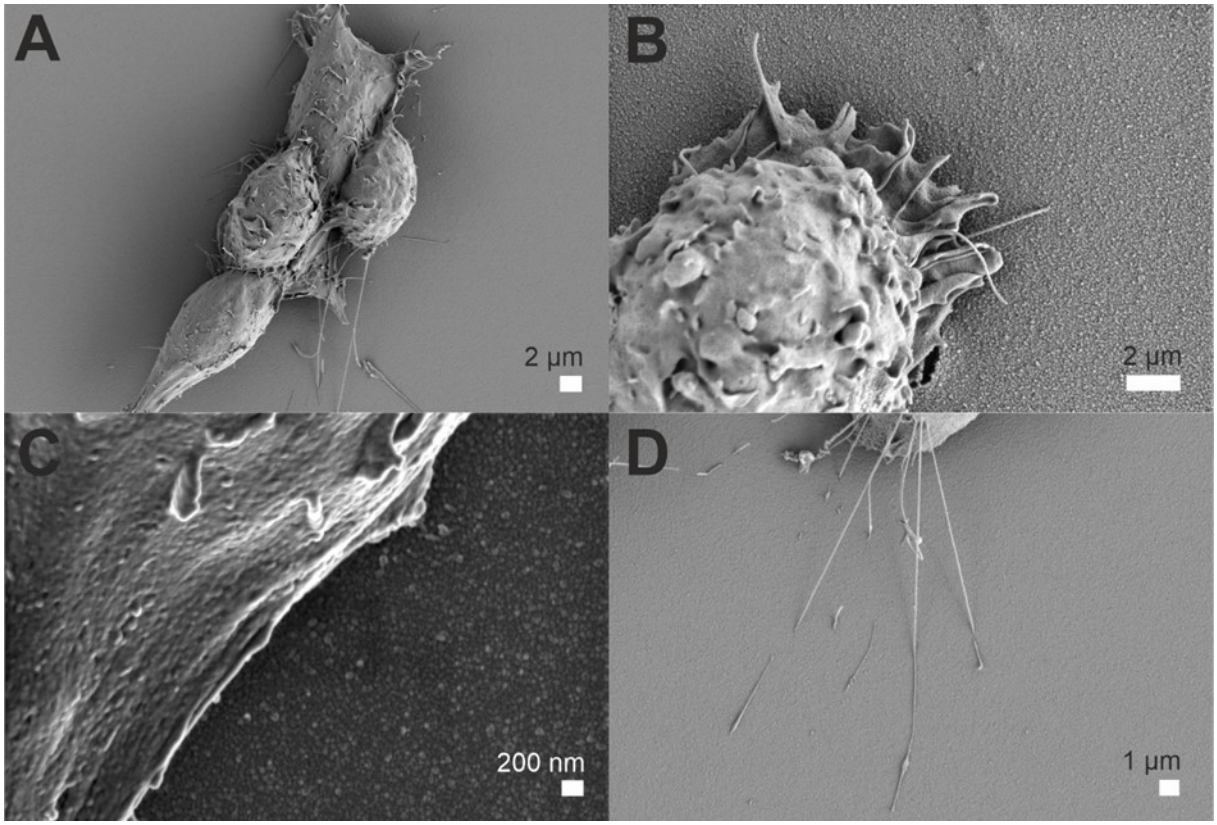

Figure 42 Representative SEM images of HEK293 cells on n-type layer crystalline PTCDI pigments. (A) Clustered cells, (B) Single cell, (C) Soma and (D) filopodia of HEK293 cells.

Neurons on Spin-coated PEDOT:PSS Polymers

Similarly to cell culture cells, neuronal cultures show viable cells with normal morphology. After seeding on the spin-coated PEDOT:PSS layer, cells maturated 2-3 weeks on the OEPC device before SEM preparation. Neurons formed complex and highly interconnected networks among each other and with supporting glia cells (Figures 43 A and B). Neurons can be observed to grow directly on the PEDOT:PSS surface (Figure 43 C) or to attach to nearby glia (Figure 43 B). In addition, multiple neurites and dendrites were observed to grow into the PEDOT:PSS layer and even into the underlying pigment layer (Figure 43 C). This reduces the ability of the OEPC device to be reused for future experiments, but the results support our assumption that the cells like to maturate on the device surface. Neuronal outgrowth on and into the surface together with the support of glia cells indicate a strong and close contact between the cell membrane and the OEPC device. Cell culture cells such as HEK293 or RBL cells can easily be dissociated from OEPC surfaces with serine proteases such as Trypsin or enzyme solutions such as Accutase. Although neurons thrive on OEPCs, removing them is a more tedious task. A harsh

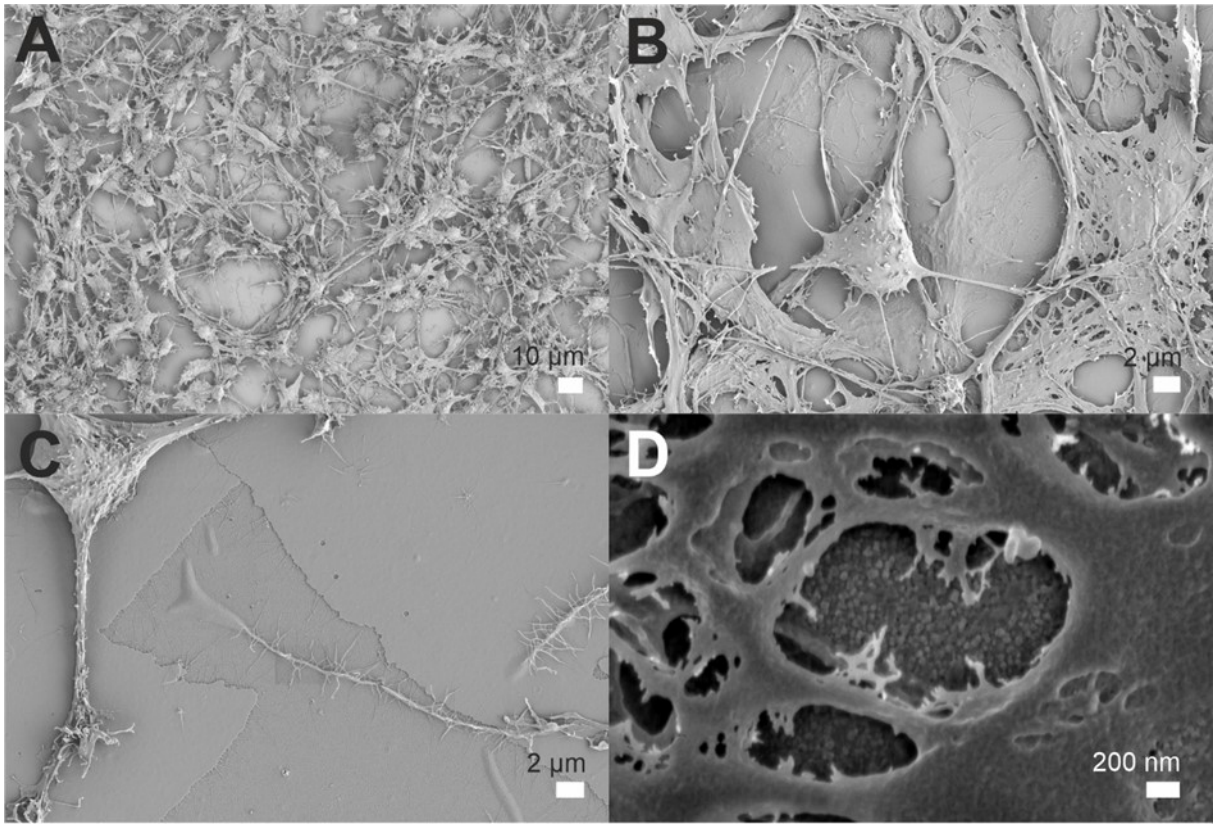

Figure 43 Representative SEM images of DIV14-21 hippocampal neurons on OEPC devices spin-coated with PEDOT:PSS. (A) and (B) interconnected neuronal network consisting of *Rattus norvegicus* hippocampal neurons and glia cells (P0-1). (C) and (D) layer structure of OEPC devices after SEM preparation protocol.

mixture of enzymes and detergents (Tergazyme) is needed to remove the cell membrane from the surface, resulting in partial defects when cleaned after an experiment (Figure 43 D). Even if the PEDOT:PSS coating has a negative effect on reusability, we could not find any negative effects on maturation behavior and cell attachment.

3.2.2 Cell Viability on OEPCs

The surface of the OEPC plays an important role in cell attachment and in the formation of a narrow cleft region between the membrane and the device. However, material optimization can introduce problems for *in vitro* experiments. Possible contaminants from the production process or degradation and delamination processes of single components as well as leachables could influence cell viability. Therefore, we tested the viability with a colorimetric MTS assay.

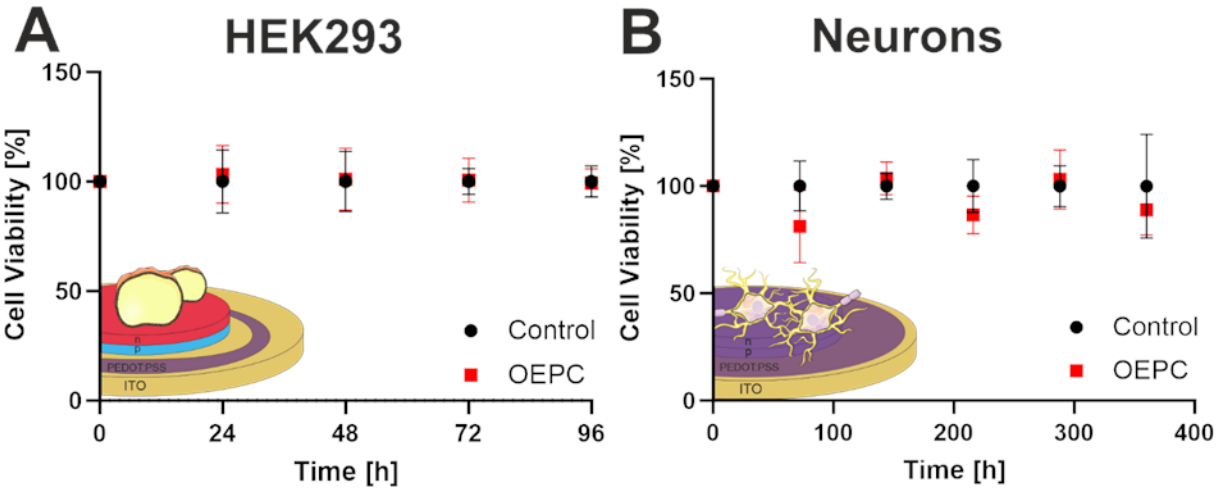

Figure 44 Cell viability of cells on OEPC devices compared to control groups (+SD). (A) HEK293 cells on n-type crystalline PTCDI pigments (red) with n = 6. (B) Hippocampal neuro-glia mixture from *Rattus norvegicus* (P0-1) on PEDOT:PSS spin-coated OEPCs (red) with n = 10. Poly-D-Lys coated glass coverslip as control group (black). Adapted and reproduced with permission from John Wiley and Sons: Advanced Materials Technologies, [20], under the terms of the Creative Commons CC BY license.

We seeded 75.000 HEK293 cells per well containing an OEPC device or a glass control. The OEPC conditions (red squares) and controls (black circles) represent at least six replicates of two independent experiments (Figure 44 A). One should note that HEK cells do not really maturate but mostly proliferate during the four days of cell culture. Due to this reason, we normalized cell viability to the control condition for each time point. Similarly to this approach, we seeded a mixture of 170.000 neuronal and glial cells for the experiment with 10 replicates from two independent experiments (Figure 44 B). We performed a multiple unpaired *t*-test analysis for each condition (desired FDR = 1.00%) and could not observe any significant change in cell viability between the OEPC conditions and respective glass controls for HEK293 cells and neurons.

3.2.3 OEPC Device Characterization

For the characterization of OEPC devices, mainly a 10 W high-power LED (660 nm) was used as illumination source that stimulates the specimens from the bottom. Other attempts to focus the light within the internal optics of the microscope or the collimation of the illumination source from the side led to a dramatic decrease in light intensity or a lack of adjustment for the focus plane. During this project, many different OEPC variants (Figure 45) were tested for their neurostimulation capabilities. For the sake of simplicity, all devices were first tested with HEK293 cells to determine their response

to light stimuli. The material composition of the devices varied for experimental reasons, but the overall structure remained the same: supporting material, metal electrode, photoactive pn-layer, and occasionally a surface coating. The first component was either a glass coverslip, a rigid PET foil or some thin Parylene-C. The electrode material was mostly ITO, but gold was also used, especially in the first attempts. The composition of the photoactive layer stayed the same, but the pixel size could have changed from a grid of small 1 mm dots to a single large pixel of 13 mm. The PEDOT:PSS coating was applied as either a spin-coated layer over the full OEPC surface area, a drop-casted ring on the metal electrode, or was not applied at all. Because many of these combinations were 'work-in-progress' devices, in electrophysiological measurements, the following OEPC design was mainly used: a glass coverslip as a supporting material for stability reasons when mounting to the patch clamp setup or practical issues when handling in cell culture. ITO was used as metal back electrode because of its material properties of being conductive but also of being transparent for light. This is especially important when the light source stimulates the OEPC from the bottom. Lastly, we preferred to use large 13 mm photo pixels because they do not need perfect light alignment and the larger OEPC surface area increases the probabilities of cells attaching to the photopixel.

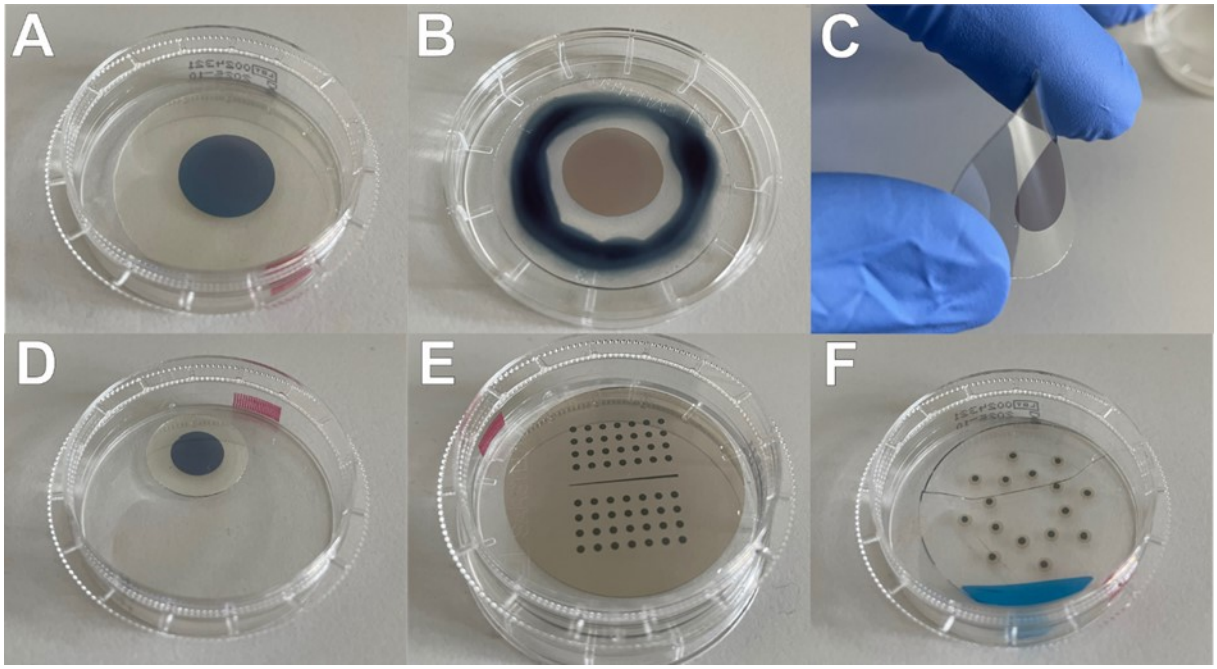

Figure 45 Selection of different OEPC devices and prototypes. (A) 30 mm ITO glass coverslip with 13 mm photopixel, (B) 30 mm ITO glass coverslip with 13 mm photopixel and a drop-casted PEDOT:PSS ring on the back electrode, (C) flexible 30 mm ITO PET foil with 13 mm photopixel, (D) 10 mm ITO glass coverslip with 5 mm photopixel, (E) 30 mm gold glass coverslip with a grid of 1 mm photopixel and (F) 30 mm glass coverslip with 1 mm photopixel on 2 mm gold back electrodes.

Influence of the Inter-pulse Time on OEPCs

OEPC devices absorb the red light from the 10 W LED that charges the surface of the photopixel and the back electrode. PTCDI, the electron acceptor molecule in the surface-exposed n-type layer, charges negatively when the light is switched on. After this cathodic leading phase, an anodic current occurs when the light is switched off. Figure 46 shows a series of light pulses and the potential measured on a HEK293 cell that is attached to the OEPC surface. Since OEPC stimulation is biphasic, one measures a negative potential followed by a positive one. The distance between both phases is dependent on the pulse length (see next section). However, the amplitudes of the negative and positive ongoings should be constant for every light pulse.

When the OEPC is stimulated with a rapid train of succeeding pulses, one observes a steady decrease in the amplitudes for both phases (Figure 46). One can interpret these results that OEPCs require a minimum inter-pulse time to fully charge and discharge. This time depends on the length of the light pulse. The overall capacity of the OEPC device is reduced with each charging cycle when there is not enough time between pulses to fully discharge. This effect can add up, decrease device efficiency, and reduce the peak high for all succeeding pulses.

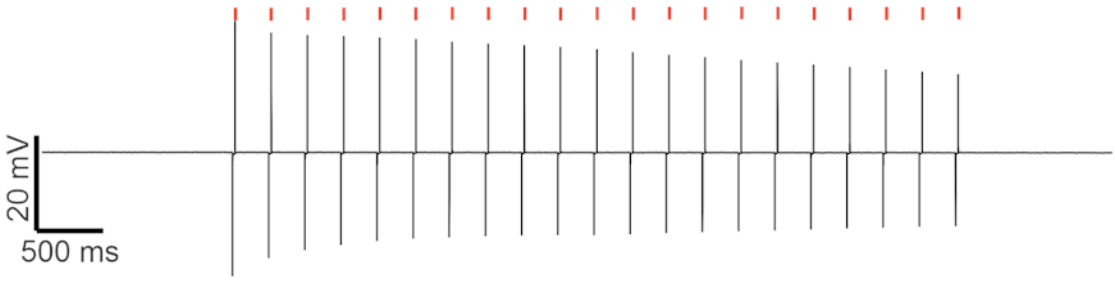

Figure 46 Representative image of the potential change measured on a HEK293 cell attached to a 30 mm ITO-glass OEPC with a 13 mm pixel. 20 ms pulses with an interpulse time of 250 ms with decreasing amplitudes of their positive and negative peak amplitudes. Red bar indicates the light pulse.

Influence of Different Light Pulse Lengths on OEPCs

Next, I measured how the recorded potential changes when altering the stimulus pulse lengths. OEPCs were given enough time to fully discharge between stimulations so that the previously described effect could be excluded.

When the light is turned on, the OEPC introduces an electric potential that creates a negative voltage peak which decays over time and reaches a steady-state plateau. This plateau is slightly lower than the resting state potential (Figure 47 A). When the light is turned off, an opposite potential peak develops. Both peak amplitudes correlate with the pulse length.

The steady-state plateau reaches a stable potential after around 2 ms to 3 ms where one can measure no further perturbation (Figures 47 A, B and C). It must be noted that capacitive stimulation itself takes place in much shorter time scales. The decay of the negative peak can be interrupted when the light is turned off before reaching the steady state. This leads to a significant reduction in the positive peak amplitude, while the amplitude of the negative peak remains the same (Figure 47 D, E and F). This could be explained by the fact that the OEPC is still negatively charged before reaching the plateau, which must be compensated for during the polarity switch.

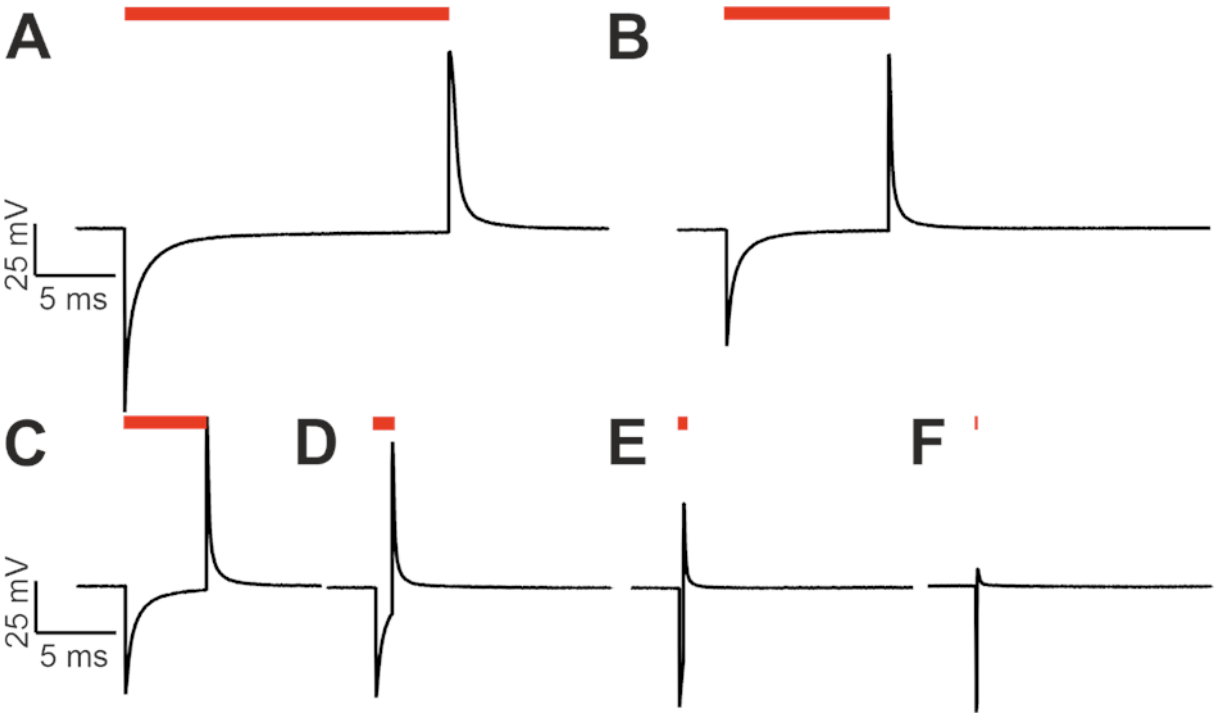

Figure 47 Light pulse length comparison of a HEK293 cells attached to a 30 mm ITO-glass OEPC with a 13 mm pixel. Representative voltage time course with a (A) 20 ms, (B) 10 ms, (C) 5 ms, (D) 1 ms, (E) 0.25 ms and (F) 0.05 ms light pulse. Red bar indicates the light pulse length on the traces, beginning with a cathodic negative peak, a steady-state plateau during the pulse and a positive peak when the light is turned off. Adapted and reproduced with permission from John Wiley and Sons: Advanced Materials Technologies, [20], under the terms of the Creative Commons CC BY license.

In patch clamp, the potential across the cell membrane is normally measured in whole cell current clamp mode between the cell interior and the outside electrolyte. It should be noted that characterization measurements on OEPCs are mostly conducted with cells, but these recorded voltage time courses do not translate directly to the membrane potential (V_m) of the measured cell.

OEPCs are capacitive stimulation electrodes operated in an electrolytic environment. Every light pulse introduces a potential perturbation on the cell membrane and in the medium. The patch clamp electrode measures in these experiments not directly the voltage time course of the cell membrane but more the potential difference between the reference electrode and the OEPC stimulation electrode. This part of the thesis concentrates on the characterization of the OEPC device. The effects of light stimulation on excitable cells and ion channel gating are described later.

Charge Balance of Different Light Pulses

The maximal values of the cathodic and anodic peak are in a certain way dependent on the distance between the OEPC stimulation electrode and the reference electrode, as well as on the conductivity of the electrolyte, which requires high diligence not to change any of those parameters. However, the rise and decay kinetics are not affected.

In Figure 47 one could observe that the cathodic and anodic phases have different rise and decay times. For this reason, the absolute peak amplitude might not be as significant in assessing the charge balance as the area under the curve (AUC). Normalized AUCs of different pulse lengths were compared for both phases. Ideally, both AUCs should sum up to 100 % with an equal area each. Faradaic processes on the photoactive layer or on the metal back electrode could alter the OEPC charging and discharging behavior, and therefore the AUCs.

We observed for all pulse lengths an equal AUC of the negative (triangle) and positive (dots) peaks (Figure 48) indicating a mostly capacitive stimulation mechanism. Short pulses reach within error margins 50 % AUC each, while longer pulses reach just 30 –45 % for the cathodic and anodic phases. This might be explained by the patch clamp amplifier trying to actively compensate for the long pulses of the OEPC stimulation electrode that is not part of the electrophysiology measurement set-up.

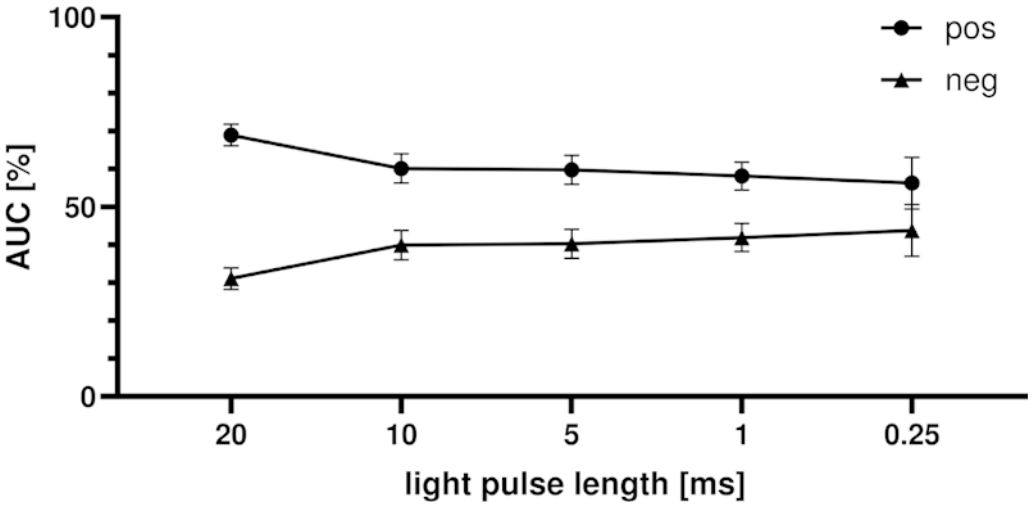

Figure 48 Area under the curve for different light pulse lengths measured with HEK293 cells attached to 30 mm ITO-glass OEPCs with a 13 mm pixel. Different light pulse lengths (+SD) for n = 14 for each condition.

The OEPC devices in this measurements (glass-ITO back electrode and no PEDOT:PSS coating on the photo pixel) indicate a balanced charging and discharging behavior. Both properties might be used for cell stimulation. The cathodic stimulation that occurs during the negative voltage peak can be used for cell depolarization on the attached membrane or the anodic one to depolarize the free membrane (see 1.5). Other OEPC devices (glass-ITO back electrode with PEDOT:PSS coating) might behave slightly different. We will focus on the cathodic leading phase since it is known to be more effective for cell stimulation and easier to directly control by light pulse manipulation.

Influence of Different Light Pulse Intensities on OEPCs

In the next step, I evaluated the impact of illumination intensity on OEPC stimulation. Figures 49 A - C show the voltage time-courses of a 0.25 ms, 1 ms and a 10 ms pulse with recordings for different light intensities. The peak amplitudes decrease with lower light intensities. One can establish a direct proportional correlation between light intensities and the absolute peak values on a logarithmic scale (Figure 49 D). The cathodic stimulus (dots) has a greater effect on the peak maximum than the anodic one. Nevertheless, one should note that the peak maximum varies in dependance on the light intensity, but this does not influence the AUC ratio between cathodic and anodic peaks or the slope of the kinetics (Figure 49 A, B, and C).

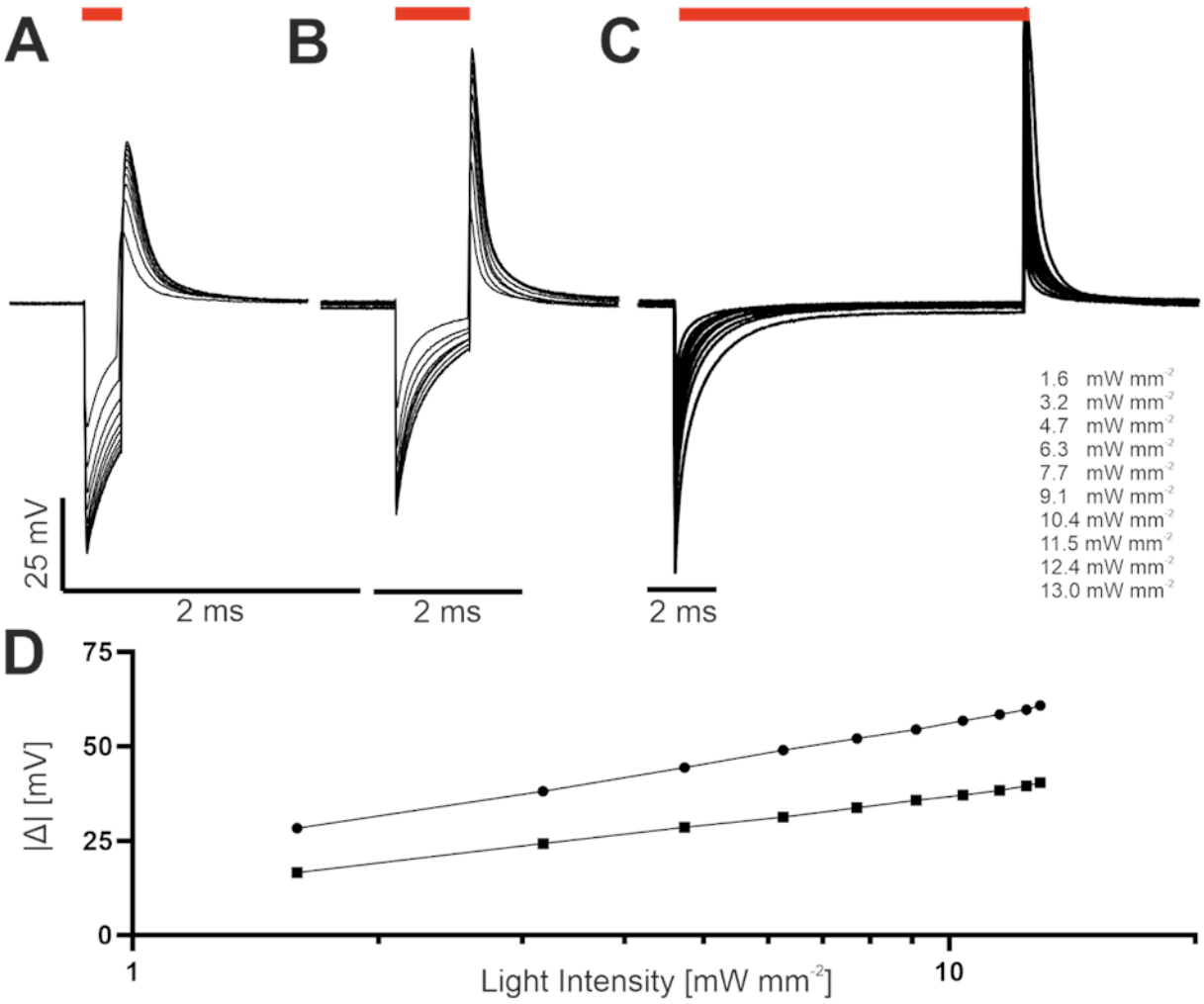

Figure 49 Comparison of the voltage shift for different light intensities measured with HEK293 cells attached to 30 mm ITO-glass OEPCs with a 13 mm pixel. Representative voltage time courses for stimulations with (A) 0.25 ms, (B) 1 ms and. (C) 10 ms light pulses each with traces for 10 % to 100 % of the LED driving current (see legend for corresponding light intensities. The red bar indicates the length of the light pulse. (D) Absolute values of the potential perturbation plotted against the light intensity. Cathodic peak (dots) and anodic peak (squares).

Comparison of Potential Perturbations Generated by Different OEPCs

Lastly, the recordings of slightly different OEPC devices were compared and evaluated how single properties influence the voltage time-course. Figure 50 A shows a representative recording of a HEK293 cell attached to a 30 mm glass-ITO OEPC stimulated with a 2 ms light pulse. A PET-ITO of the same size (Figure 50 B) shows decreased cathodic and anodic peak amplitudes compared to the glass. One can further observe a little bump at the end of the anodic peak. This bump is also present in other PET-ITO back electrode OEPCs like the 15 mm device (Figure 50 C).

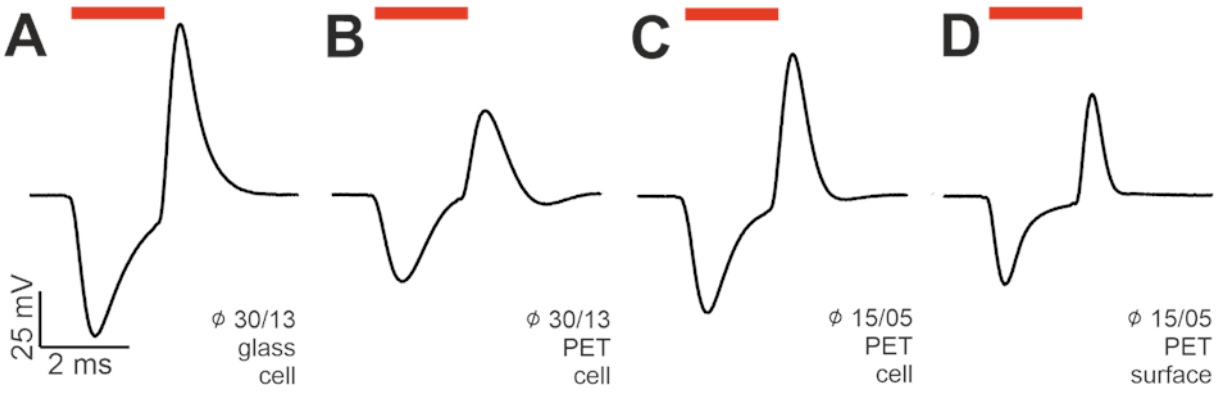

Figure 50 Comparison of the voltage time-courses and potential perturbations caused by different OEPC devices during a 2 ms light pulse. Representative traces of (A) 30 mm OEPC with a 13 mm pixel with ITO-glass or (B) ITO-PET foil as back electrode measured with a HEK293 cell. (C) 15 mm OEPC with a 5 mm pixel with ITO-PET foil measured with a HEK293 cell or (D) measured directly on the device surface without a cell.

Figure 50 D shows the same OEPC device as in Figure 50 C, but this trace was recorded with a patch pipette close to the surface and not attached to a cell membrane as in (C). One observes decreased peak maxima for both phases, but more interesting is, that the slope of the cathodic peak seems to be different. The surface measurement reaches earlier the steady-state plateau (Figure 50 D) than the cell attached variant (Figure 50 C). Both observations might be explained by an overlap of the stimulation artifact (i.e. the potential change caused by the OEPC device – see below), the pipette tip in the electrolyte vs. the cell attached resistance and membrane capacity. There might be more parameter variations such as the thickness and the ration between the pigment p- and n-type layer, but the improvement of OEPC device designs is out of the scope of this work.

Despite those minor differences, the overall voltage time course is similar between all measured variants of the OEPC device. More important is that the voltage time courses are even comparable between measurements where the pipette is close to the surface or attached to a cell. As mentioned above, the OEPC device acts as a third electrode, next to the patch pipette and the reference electrode of the patch clamp system. The patch clamp electrode measures the membrane potential by measuring the difference between the inside of a cell and the reference electrode.

However, the OEPC stimulation electrode changes the potential in the electrolytic environment. Recording this alone can provide valuable information about the function and working principles of a capacitive stimulation electrode, but one must be careful not to misinterpret this information and regard those recordings as actual membrane potentials. When the patch pipette is connected to a cell,

most of the potential difference recorded between the patch clamp electrodes can therefore be regarded as an artifact caused by the stimulation electrode. To account for this, we fixed all electrodes to not change positions to achieve comparable results between measurements. However, even the amount of electrolyte in the measuring chamber or its ionic composition might change the absolute values of the voltage time course.

The voltage time courses of a depolarization or a hyperpolarization event is still present in the recordings of a cell membrane, even if the cathodic leading stimulation artifact overlaps with the actual membrane potential in current clamp mode. Since HEK293 cells are not excitable, they may not be the best model system for studying neuronal excitation. Nevertheless, they are a valuable system for characterizing ion channel gating, especially when voltage-gated channels are overexpressed.

3.2.4 Effects of OEPCs on Ion Channel Gating

Comparison Between the Kinetics of Voltage-Gated Ion Channels

Voltage-gated ion channels are an ideal target to directly measure the response to a light activated OEPC device in cells or cell membranes. Our hypothesis is that photocapacitive stimulation changes the extracellular potential in the electrolyte, creating an electric field that might affect the voltage sensor and, therefore, switch the conformation of voltage-gated ion channels.

The membrane depolarization and the generation of AP in excitable cells is driven mainly by sodium channels. One can measure the flux of sodium ions across the membrane into the cell when the channels are open. This is done using the patch clamp technique in voltage clamp mode and whole cell configuration. In addition, voltage-gated potassium and calcium channels also play an important role in the various phases of APs in neurons or cardiomyocytes. Voltage-gated channels in these cells have different gating kinetics, and all their currents overlap, making it difficult to isolate the gating of single channel types and to record their activation separately.

Instead, HEK293 is an easy-to-handle cell model that offers the advantage of overexpressing exogenous DNA or endogenous channels with high transfection rates and low expression problems. The resulting currents may not be physiological, but the experimental results are relatively simple to interpret in a well-characterized and controlled experimental environment with adjustable parameters. Therefore, we tested different ion channels overexpressed in HEK293 cells to find the perfect conditions to study the influence of the fast capacitive stimulation of OEPCs on ion channel gating.

Voltage-gated sodium channels have a short activation period and inactivate rather quick, making it difficult to distinguish between capacitive currents of light-mediated electrode stimulation and fast ionic currents during channel gating. Light pulses might even be longer in duration than the opening and the inactivation of the channel combined. Therefore, we tested the voltage-dependent T-type calcium channel subunit α_1G ($Ca_v3.1$) that also plays a role in repetitive firing of APs in certain cells. We transiently transfected HEK293 cells with the $Ca_v1.3$-YFP plasmid and applied a voltage step protocol from -80 mV with increments of +10 mV. At -50 mV, one can observe channel activation and the inward current of Ca^{2+} ions. The current flow lasts between 20 ms and 30 ms and the maximum peak is reached at around -300 pA (Figure 51 A). After clamping the membrane to +10 mV, no inward channel activity was present anymore. $Ca_v3.1$ is a relatively fast inactivating ion channel but compared to sodium

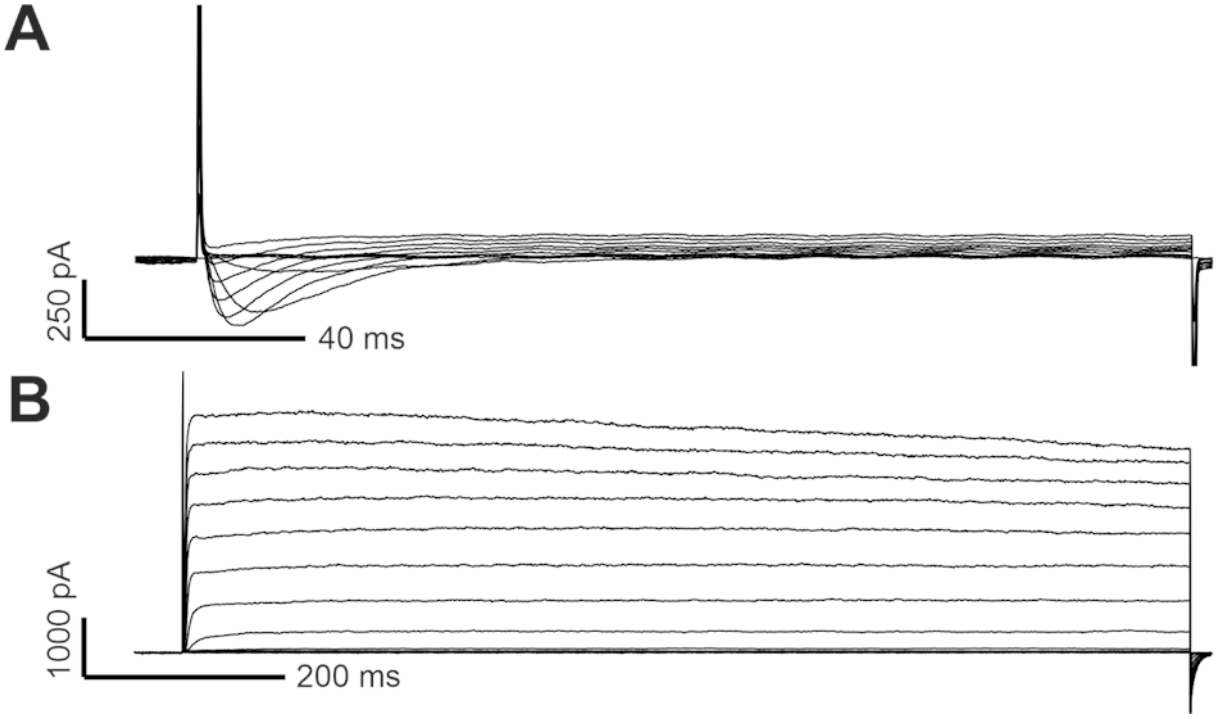

Figure 51 Current time courses of $Ca_v3.1$ and $K_v1.3$ ion channels. Representative traces of voltage clamp measurements with voltage steps in +10 mV increments of HEK293 cells on glass coverslips transiently transfected with (A) $Ca_v3.1$ starting at -80 mV and (B) Tag-RFP-$K_v1.3$ starting at -100 mV. All cells were clamped for 3 s at holding potential before each depolarization step for the reactivation of inactivated channels.

channels it has the advantage of a relatively longer lasting activation period. Unfortunately, for the purpose of light regulation, this activation is not constant enough or sustained over longer time periods.

Another tested ion channel was $K_v1.3$, a shaker-related subfamily voltage-gated potassium channel. It plays a role in the repolarization phase of APs since it is a delayed rectifier. For an initial test, HEK293 cells were transiently transfected with the genetic information of the ion channel. The potent channel inhibitor PAP-1 in the culture medium was removed 4 hours before measurements. A voltage step protocol was then applied starting from -100 mV with +10 mV steps. At -30 mV a strong outward current develops within 1.5 ms to 5 ms after the capacitive transient, indicating the K^+ ion flux out of the cell. Higher clamped membrane potentials resulted in even higher currents of a couple of nA that stay constant over the whole depolarization step or inactivate very slowly (Figure 51 B). HEK293 cells have a typical resting membrane potential of around -30 mV (±10 mV) which causes the cells to die within 12 h to 24 h when transfected with this ion channel due to a permanent channel activity during cell culture. Therefore, an excess of the inhibitor is necessary during selection and cultivation of cells that stably express $K_v1.3$. Further experiments indicated that the inhibitor PAP-1 (EC_{50} = 2 nM) cannot

washed out properly by changing the medium or through long-term perfusion with extracellular patch clamp solutions. Due to that, cells were given 4 h to biosynthesize new ion channels in a PAP-1$^-$ medium before using them in patch clamp experiments. This has also the effect that the recorded currents are comparable between single cells and experiments.

The K_v1.3 channel was selected to carry out further experiments for the characterization of the ion channel and experiments for light stimulation of cells on OEPCs. The ion channel activates within milliseconds quite fast but not too fast, allowing a better distinction between capacitive transients from the patch clamp electrode and the OEPC stimulation. The rather slow inactivation might further allow to test different light pulse lengths or their effect on currents while clamping the membrane to subthreshold potentials. The OEPC characterizations were mostly measured in current clamp in an electrolytic environment, but voltage clamp measurements of ion channels allow for a direct quantitative and qualitative evaluation of what is happening within the cell and on the cell membrane during OEPC stimulation.

Characterization of K_v1.3

An in-depth characterization of the ion channel allowed us to develop a Hidden Markov Modell to calculate opening and closing probabilities as well as to develop a computational model for the membrane depolarization (see discussion). These characterizations also allowed us to measure the reversal potential of K_v1.3 and to calculate the channel conductance. Therefore, a HEK293 cell line was established that stably integrated the Tag-RFP-K_v1.3 plasmid into the genomic DNA. Single clones were selected and characterized for the new cell line that functionally overexpresses the potassium channel in its membrane (stHEK293$_{Kv1.3}$).

First, I tested single cells with a step protocol in a whole cell voltage clamp configuration. Before each voltage step (+10 mV), a 3 s lasting holding potential of -100 mV was applied to reconstitute inactivated ion channels. The channel was observed to remain closed between command voltages of -100 mV and -40 mV. K_v1.3 starts to open at -30 mV, as shown by the developing outward currents (Figure 52 A). More depolarizing command voltages resulted in large activation currents of 15 nA (± 5 nA). These currents were even higher than the currents of the transiently expressed K_v1.3 channels. There was no inactivation of the channels after reaching the maximum current and within the 400 ms of the voltage step. All experiments and various measurements showed very similar results since we developed stHEK293$_{Kv1.3}$ from a single clone.

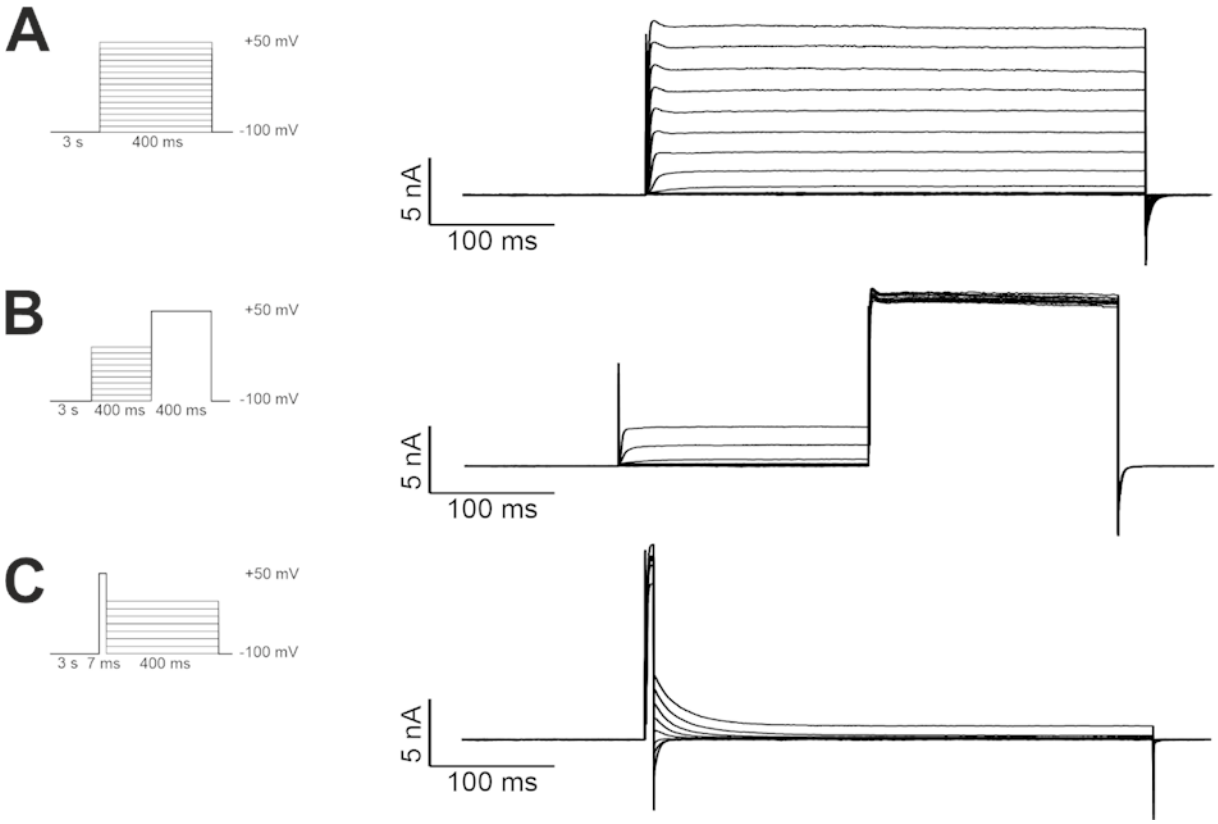

Figure 52 Characterization of K_v1.3 kinetics. Stimulation protocol (left) and representative trace (right) with each n = 23 in whole cell voltage clamp configuration. (A) Activation protocol. (B) Steady state inactivation protocol. (C) Deactivation protocol. Adapted and reproduced with permission from John Wiley and Sons: Advanced Materials Technologies, [20], under the terms of the Creative Commons CC BY license.

In the next step, different protocols (see insets) were used to determine the steady-state inactivation (Figure 52 B) and deactivation currents (Figure 52 C) of K_v1.3. No further inactivation was observed despite applying pre-depolarization pulses, indicating a negligible inactivation for further measurements with stHEK293$_{Kv1.3}$. The deactivation protocol was used to determine the reversal potential of K_v1.3. After the 7 ms depolarization pulse, another depolarization step was applied to obtain tail currents (Figure 52 C).

The measured tail currents from the previous experiment were plotted against the applied command voltage as shown as an I-V plot in Figure 53. With this information, the reversal potential of V_{rev} = -73 mV was obtained for K_v1.3. This potential describes the point where there is no net potassium flow across the membrane. The information of Figure 52 A and V_{ref} will later be used to calculate the conductance G of the ion channel.

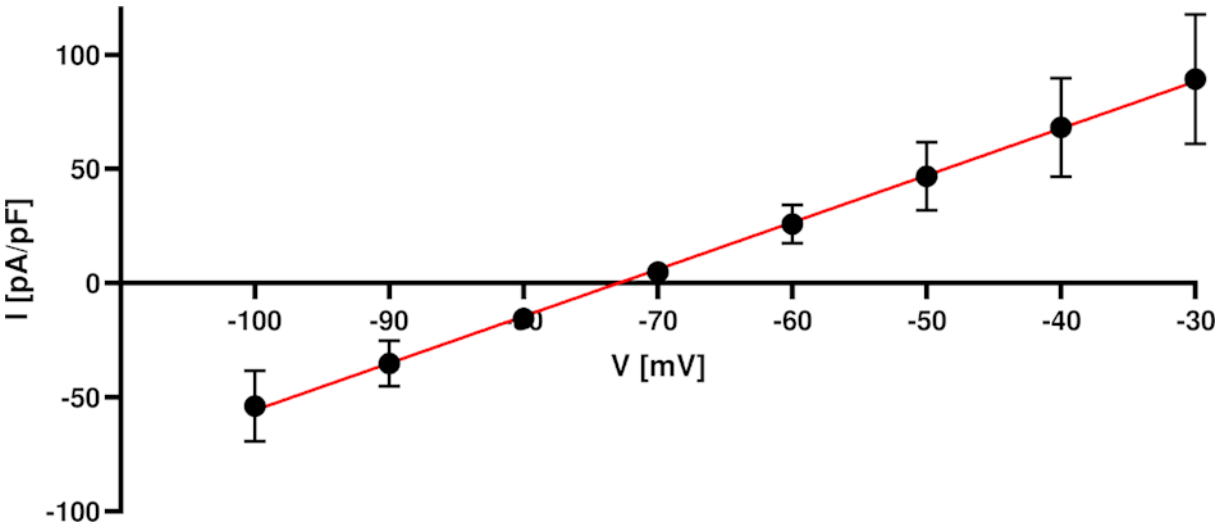

Figure 53 Reversal potential of K_v1.3. I-V Plot of tail currents plotted against the command voltage V_{rev} = -73 mV (n = 7). Adapted and reproduced with permission from John Wiley and Sons: Advanced Materials Technologies, [20], under the terms of the Creative Commons CC BY license.

K_v1.3 Gating During OEPC Stimulation

To understand the mechanism how OEPCs influence ion channel gating, one must be able to distinguish between capacitive transients caused by patch clamp amplifier, OEPC stimulation artifacts, ionic currents of endogen channels, and OEPC-induced currents of the voltage-gated ion channels. Therefore, current traces of wild-type HEK293 and K_v1.3 overexpressing cells were recorded on plain glass coverslips or attached to OEPCs (Figure 54) during light stimulation. The following experiments were conducted with OEPC devices that have a dropcasted PEDOT:PSS ring on the back electrode which improves the electrochemical capacitance and decreases the interfacial impedance of the device. A 10 W LED was used as light source and illumination was directed from the bottom.

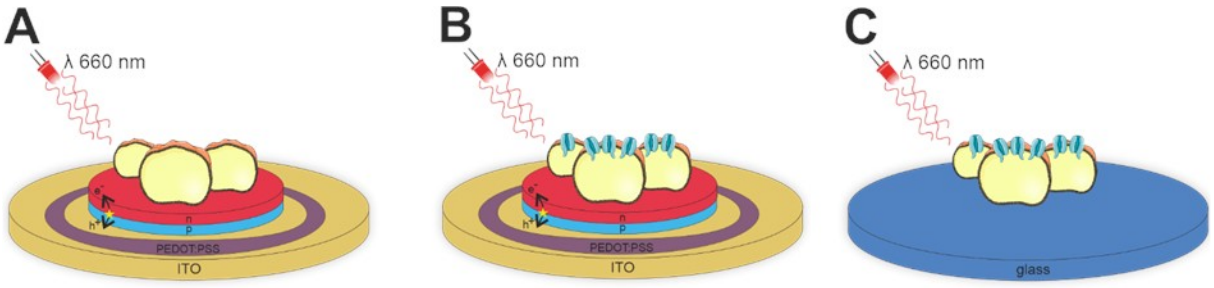

Figure 54 Experimental configuration of K_v1.3 gating through OEPC stimulation. (A) 30 mm OEPC device with dropcasted PEDOT:PSS and wtHEK293 cells. (B) 30 mm OEPC device with dropcasted PEDOT:PSS and stHEK293$_{Kv1.3}$ cells. (C) 30 mm glass coverslip and stHEK293$_{Kv1.3}$ cells. Illumination with a 10 W LED from bottom; cells not to scale.

In the following experiment, wtHEK293 cells were seeded on an OEPC device and current traces were recorded in the whole cell voltage clamp configuration (step protocol - Figure 55 A inset). The digitizer was programmed to control the LED driver via TTL logics. This allows for better reproducibility and comparison between experiments since there is a precise time control for light pulses. The first and last capacitive transients arise from the switch to the command voltages. As expected, we could not detect any significant current between the peaks (Figure 55 A). When applying a 5 ms light pulse within the voltage steps, the OEPC device charges and discharges, which appears as two additional capacitive transients at the beginning and the end of the pulse (Figure 55 B). The negative transient was clipped for better representation of the traces. A short negative current of around 7 pA/pF can be observed after turning on the light on. Whether this represents some ionic current flow across the cell membrane or whether this is an artifact caused by the OEPC stimulation was not further investigated. But overall, this experiment shows the effects of light on wild-type cells and membranes attached to OEPCs.

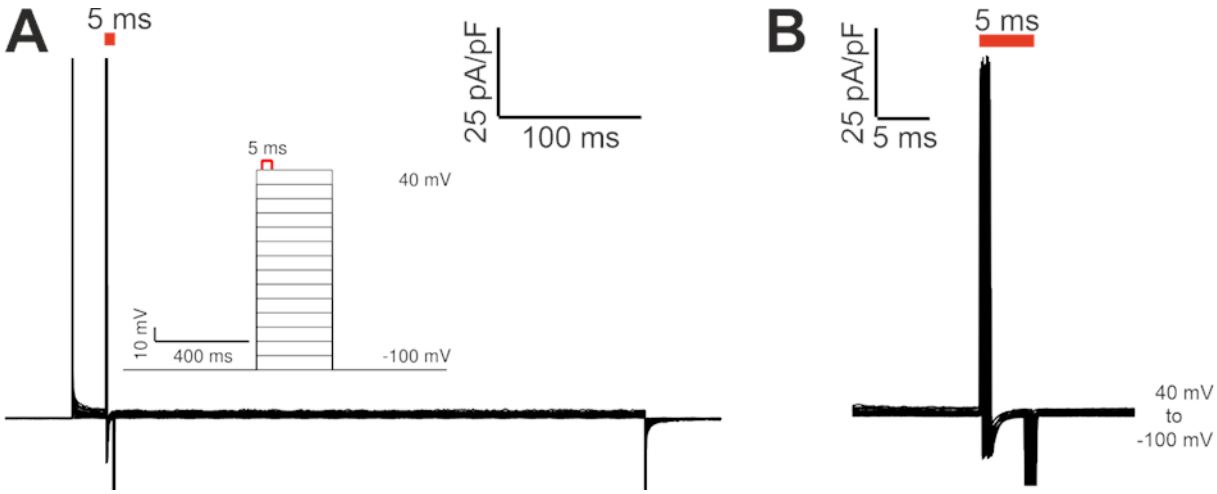

Figure 55 Stimulation of wtHEK293 cells on 30 mm OEPCs with a PEDOT:PSS ring. (A) Representative traces of a voltage clamp step protocol (inset) in whole cell configuration and a 5 ms LED pulse of 13 mW mm^{-2} at 660 nm. (B) Zoom into the capacitive transients evoked by the stimulation. Adapted and reproduced with permission from John Wiley and Sons: Advanced Materials Technologies, [20], under the terms of the Creative Commons CC BY license.

For the next experiment, st$HEK293_{Kv1.3}$ cells were seeded on the same type of OEPC devices and recorded with the same protocol. Clamped cells start to conduct at command voltages of -30 mV, as previously shown in transiently transfected cells. A strong outward current of potassium ions develops within the first 10 ms between -30 mV and +40 mV (40 – 50 pA/pF, Figure 56 A) that reaches a steady-state plateau and lasts the entire 400 ms of the activation protocol without any inactivation. The same

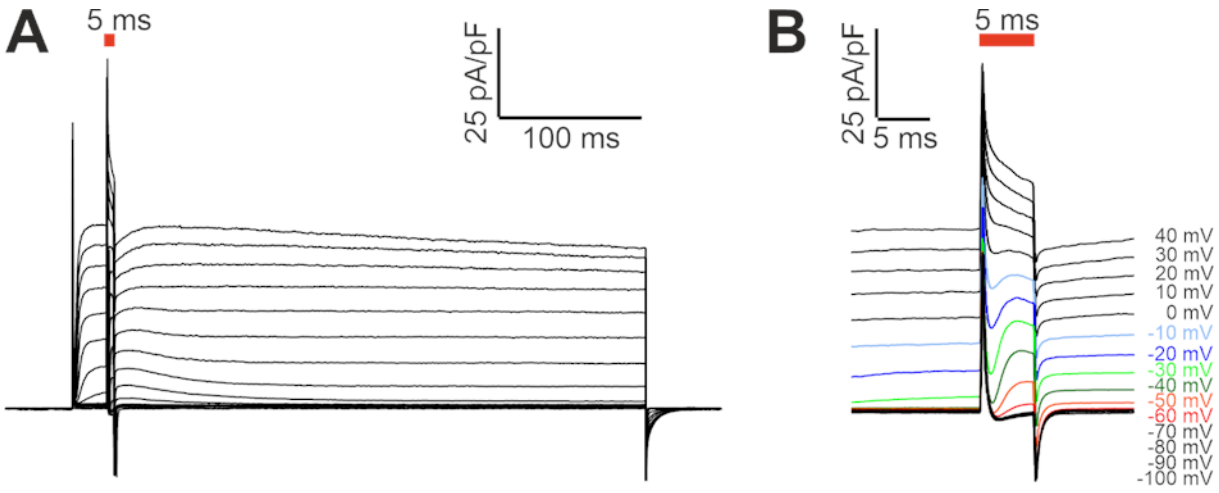

Figure 56 Stimulation of stHEK293$_{Kv1.3}$ cells on 30 mm OEPCs with a PEDOT:PSS ring. (A) Representative traces of K_v1.3 activation with a voltage clamp step protocol in whole cell configuration and a 5 ms LED pulse of 13 mW mm^{-2} at 660 nm. (B) Zoom into the capacitive transients and further ion channel activation evoked by the stimulation. Adapted and reproduced with permission from John Wiley and Sons: Advanced Materials Technologies, [20], under the terms of the Creative Commons CC BY license.

positive and negative light induced capacitive transients known from the previous experiment appear at the beginning and the end of the light pulse. Even when already activated by the clamp protocol, K_v1.3 ion channels show further gating and an additional ionic current during the light pulse (Figure 56 B).

The most important observation in this context is the conductivity of the ion channels during light stimulation at membrane potentials clamped to -60 to -40 mV where K_v1.3 channels would remain closed without light stimulation (Figure 56 B). This additional potassium efflux is caused by a pre-depolarization of the membrane due to the OEPC device acting as electrode. In addition, the time-courses of channel activation induced by clamping the cell with the patch amplifier at the beginning of the protocol (-30 mV to -10 mV) and induced by OEPC stimulation (-60 mV to -40 mV) during the light pulse are similar. They show the same delayed activation slopes that are characteristic for K_v1.3 gating (for more on that, see also the IV and GV characteristics below). K_v1.3 reaches maximum conductance at a membrane potential of around 0 mV or +10 mV. Light pulses or the patch clamp amplifier can not induce further currents at this point (see also the GV-plot). Further light stimulation beyond that induces only inactivation.

An interesting last observation is that OEPC devices induce not only a shift in ion channel gating when the light is turned on. One can also observe a conductance after the negative transient when the light is turned off (Figures 56 A and B). Like before, K_v1.3 should not be conductive between -60 and -40 mV

but turning the light off induces a current that decays to 0 pA/pF over time. Between -30 mV and 0 mV, the current decays to the steady-state plateau which is caused by the holding potential. High command voltages (+10 mV and more) also result in channel inactivation that recovers over time.

The light stimulus can activate ion channel gating in two different ways. Turning the light on will charge the OEPC and lead to a cathodic stimulation while turning the light off discharges the device which leads to an anodic event. The membrane of a cell further divides into two parts, an area that is attached to the photocapacitve stimulation electrode or a membrane patch that is in contact with the surrounding electrolyte.

During cathodic stimulation, capacitive cell coupling leads to depolarization of the attached membrane and to a slight hyperpolarization of the free membrane (see Introduction). The opposite occurs during the anodic phase, when the OEPC discharges and the free membrane depolarizes. However, the hyperpolarizing or depolarizing effect on the free membrane is in both mechanisms smaller because the membrane is farther away from the electrode (OEPC). But the free membrane also has more ion channels than the smaller patch of the attached membrane. When evaluating the $K_v1.3$ conductance that occurs when the light is turned off, one assumes that this is caused by the anodic phase and the depolarization of the large free membrane, but one should also remember that our cell model highly overexpresses the $K_v1.3$ ion channel. The produced currents and the lower potency of anodic cell depolarization might be negligible under physiological conditions.

As a control, stHEK293$_{Kv1.3}$ cells were also seeded on glass coverslips. The same protocol with light illumination as in the previous experiments (Figure 55 – inset) was applied. K_v1.3 showed the expected gating behavior with a strong outward current starting to conduct at -30 mV and a non-inactivating steady state plateau phase (Figure 57 A). However, the light pulse does not induce any additional current and the minor transients are negligible and probably the result of electric noise caused by the 10 W LED placed 2 cm below the OEPC device (Figure 57 B).

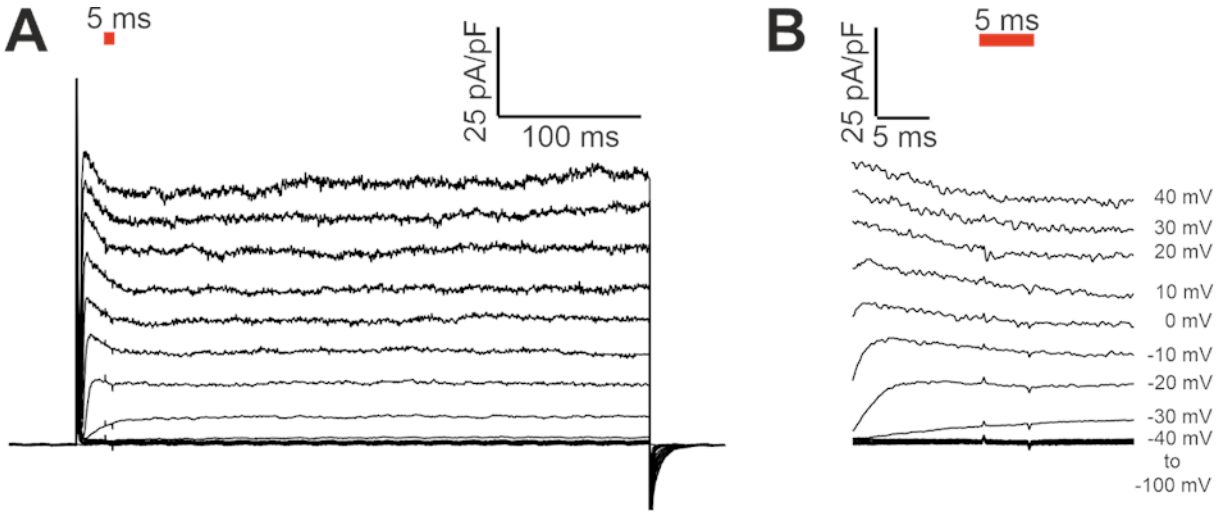

Figure 57 Stimulation of stHEK293$_{Kv1.3}$ cells on 30 mm glass coverslips. (A) Representative traces of K_v1.3 activation with a voltage clamp step protocol in whole cell configuration and a 5 ms LED pulse of 13 mW mm^{-2} at 660 nm. (B) Zoom into the area of the light pulse. Adapted and reproduced with permission from John Wiley and Sons: Advanced Materials Technologies, [20], under the terms of the Creative Commons CC BY license.

Returning to the experiments with stHEK293$_{Kv1.3}$ cells attached to OEPC devices, the next step was to evaluate the influence of different light intensities on ion channel gating. Therefore, the maxima of the measured ionic currents were plotted against the respective command voltages on an I/V-diagram (Figure 58) for three light conditions. K_v1.3 starts to conduct as expected exactly at -30 mV when no light was applied (black trace). Light pulses (5 ms) induced potassium efflux already at -60 mV with 13 mW mm^{-2} light intensity (red trace). Half maximal light intensity (7.5 mW mm^{-2} blue trace) induced channel gating between -50 mV and -40 mV. All traces converge at -20 mV at one point (160 pA/pF) where the gating behavior and current maxima are the same for all three light conditions.

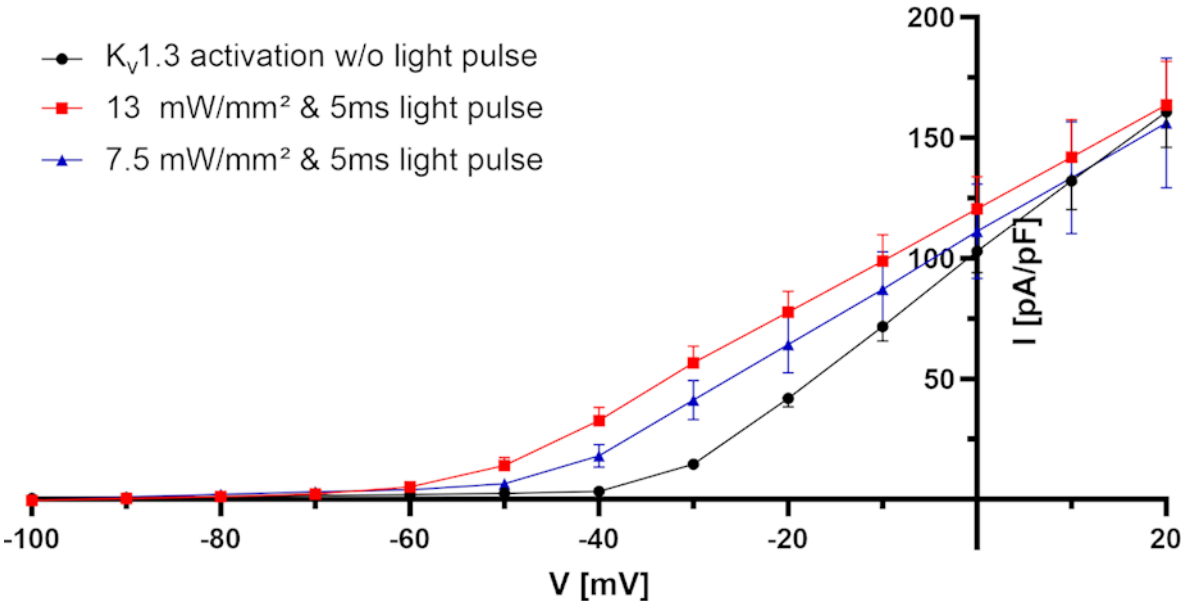

Figure 58 IV plot of stHEK293$_{Kv1.3}$ cells on 30 mm OEPCs with a PEDOT:PSS ring stimulated with different light intensities. Normalized peak currents derived from voltage clamp step protocol measurements in whole cell configuration with no light illumination (black – n = 17) or 5 ms LED pulses with 13 mW mm^{-2} (red – n = 17) or 7.5 mW mm^{-2} (blue – n = 10) at 660 nm. Adapted and reproduced with permission from John Wiley and Sons: Advanced Materials Technologies, [20], under the terms of the Creative Commons CC BY license.

The conductance of K_v1.3 channels was then calculated for four different light conditions. As the reversal potential was experimentally determined to be V_{rev} = -73 mV (see Figure 53), the conductance can be calculated with the measured maximal current I_{mem} and the respective membrane holding potential V_{mem}:

$$G = \frac{I_{mem}}{V_{mem} - V_{rev}} \tag{7}$$

The conductance G was then normalized and plotted against the command voltage (Figure 59 -GV-diagram). The half-maximal conductance G_{50} for K_v1.3 without light stimulation is reached at around -16 mV (black trace - Figure 59 A). Applying the brightest light intensity (13 mW mm^{-2}) results in a shift of G_{50} of about 27 mV towards a more negative potential (red – Figure 59 B). Half the light intensity (7.5 mW mm^{-2}) leads to a ΔG_{50} of around 15 mV (blue) and 1.6 mW mm^{-2} light pulses to a ΔG_{50} of around 10 mV. Although the conductance shift is not direct proportional to the light intensity, it was proven that OEPCs are able to shift the conductance 30 mV towards a more negative potential which allows to activate K_v1.3 already at a V_m of -60 mV instead of the normal -30 mV.

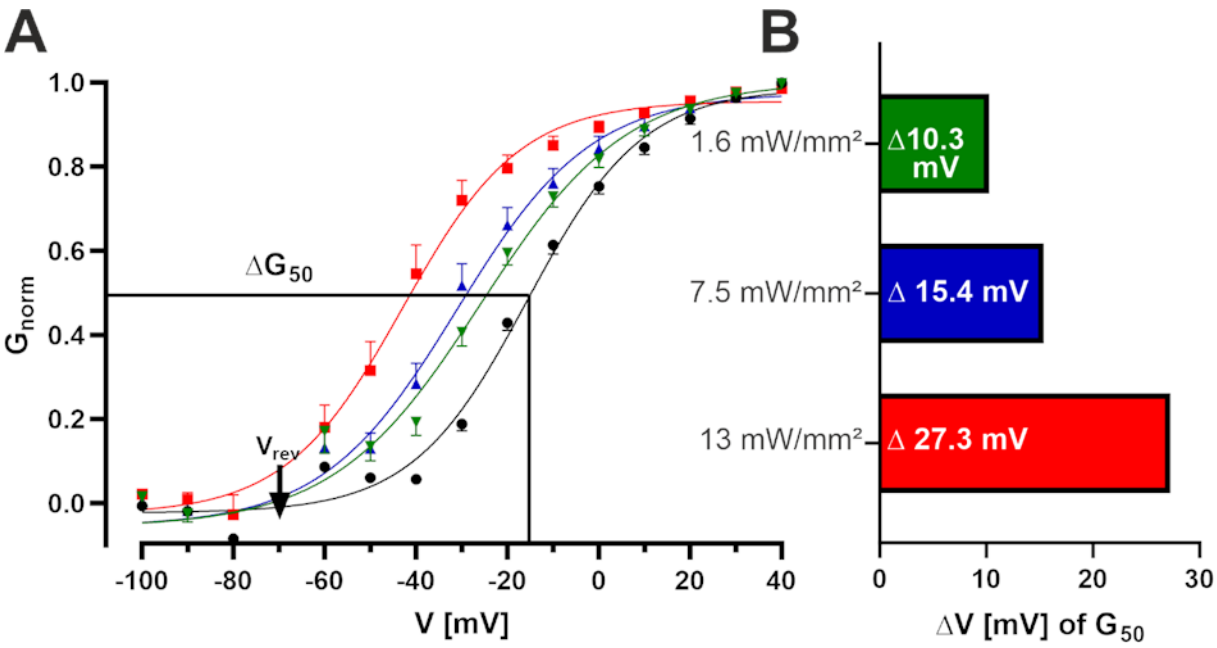

Figure 59 GV plot of stHEK293$_{Kv1.3}$ cells on 30 mm OEPCs with a PEDOT:PSS ring stimulated with different light intensities. (A) Normalized conductance with mean values (±SEM) for no light illumination (black – n = 17) or 5 ms LED pulses with 13 mW mm^{-2} (red – n = 17), 7.5 mW mm^{-2} (blue – n = 10) or 1.6 mW mm^{-2} (green – n = 9) at 660 nm. (B) Shift of the half maximal conductance ΔG_{50} derived from different light stimulations towards a more negative potential compared to non-light stimulated K_v1.3 conductance. Adapted and reproduced with permission from John Wiley and Sons: Advanced Materials Technologies, [20], under the terms of the Creative Commons CC BY license.

Ion Channel Conductivity in the Free and Attached Parts of the Membrane

The photocapacitive stimulation method affects mainly the cell membrane patch attached to the OEPC device, but many factors such as cell geometry or the cleft size between the electrode and the membrane could contribute important factors to it. Additionally, with the patch clamp technique one is limited to record the sum of all currents across a membrane. Measurement of distinct cell regions is not possible. In collaboration with Dr. Theresa Rienmüller, TU Graz and Professor Vedran Đerek, University of Zagreb, we wanted to simulate the effect of extracellular stimulation on cell membranes. Therefore, an HMM was established that simulates the channel gating of K_v1.3 in both membrane domains (attached and free) by dividing the cell into two distinct electrical circuits (Figure 60 A).

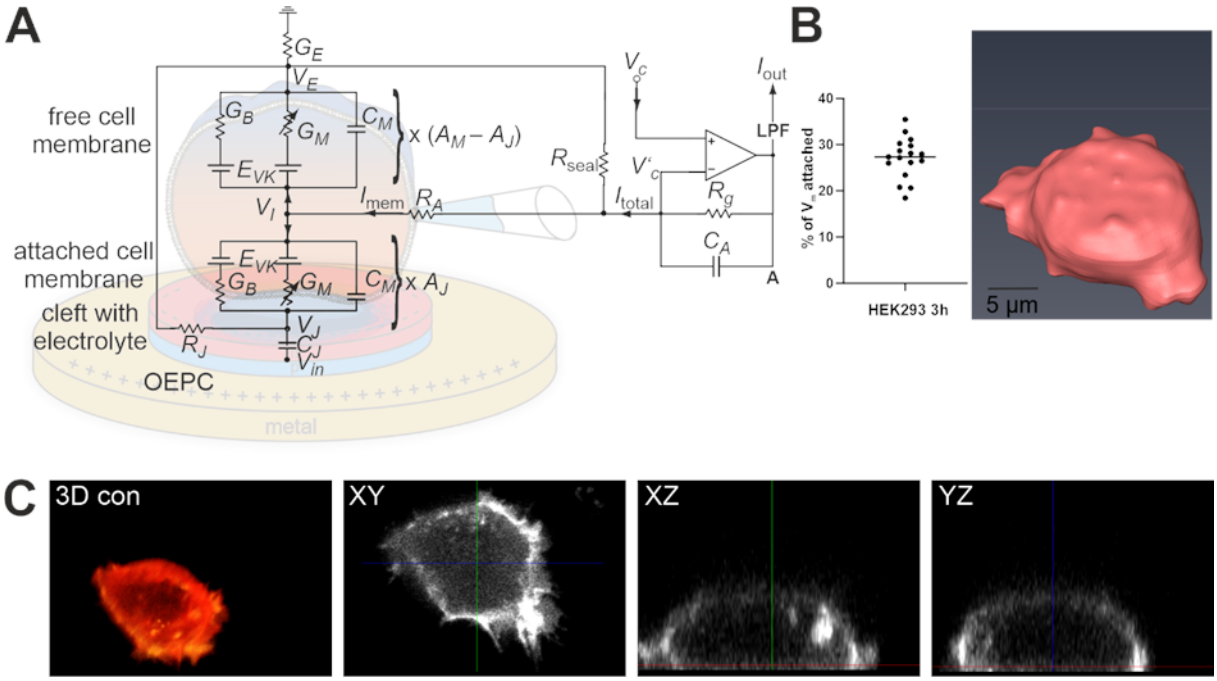

Figure 60 Comparison of the attached and the free membrane of HEK293 cells. (A) HMM of a HEK293 cell expressing $K_v1.3$, divided into two domains forming the attached and free part of a cell on a photocapacitve stimulation device. (B) 3D model of a representative HEK293 cell 3 h after seeding and the percentage $V_{m\_attached}$ on the surface area (n = 17, median 27 % with interquartile range from 24.7 % to 30.0 %). (C) 3D convolution and confocal microscopy Z-stack images of a HEK293 cell expressing Mem1-RFP. Adapted and reproduced with permission from John Wiley and Sons: Advanced Materials Technologies, [20], under the terms of the Creative Commons CC BY license.

The HMM requires several information. Channel kinetics and currents were derived from previous patch clamp measurements. Another important parameter is the size of the membrane areas that adhere to a surface or are free-floating. We used Z-stack images of HEK293 cells 3 h after seeding that expressed a fluorophore on the membrane surface (Figure 60 C). Afterwards, I created a polygon mesh and a 3D surface model via 3D convolution. On could then calculate the ratio of $V_{m\_attached}$ vs. V_{m_total}, which was determined to be 27 % (Figure 60 B). This observation is independent of the initial size of the cell and includes all filopodia. Patch clamp recording and membrane data allowed the HMM to determine channel conductances and membrane voltage time courses separated for both membrane domains during stimulation (see discussion and appendix).

K_v1.3 Gating Compared to Amplifier Stimulation

As mentioned above, OEPCs depolarize the attached membrane by cathodic leading stimulation and alter ion channels within this area. Another aspect to consider is that the whole surface of a small HEK293 cell is clamped when a command voltage is applied. In the last ion channel experiment, we wanted to compare the K_v1.3 activation induced by the light-mediated stimulation of the attached membrane to the patch clamp amplifier-induced depolarization of the whole cell.

The stimulation protocol was adapted and introduces now an additional depolarization step of Δ0 mV, Δ10 mV or Δ20 mV to the step protocol instead of a 5 ms light pulse (Figure 61 B). The conductances of all three conditions were calculated and plotted in a GV-diagram (Figure 61 A). As before, the half-maximal G_{50} for K_v1.3 is at -16 mV when no stimulation is applied. When clamping the cell for 5 ms to an additional +20 mV or +10 mV, one observes ΔG_{50} to shift 32 mV (orange) or 18 mV (yellow) respectively towards a more negative potential (Figure 61 B).

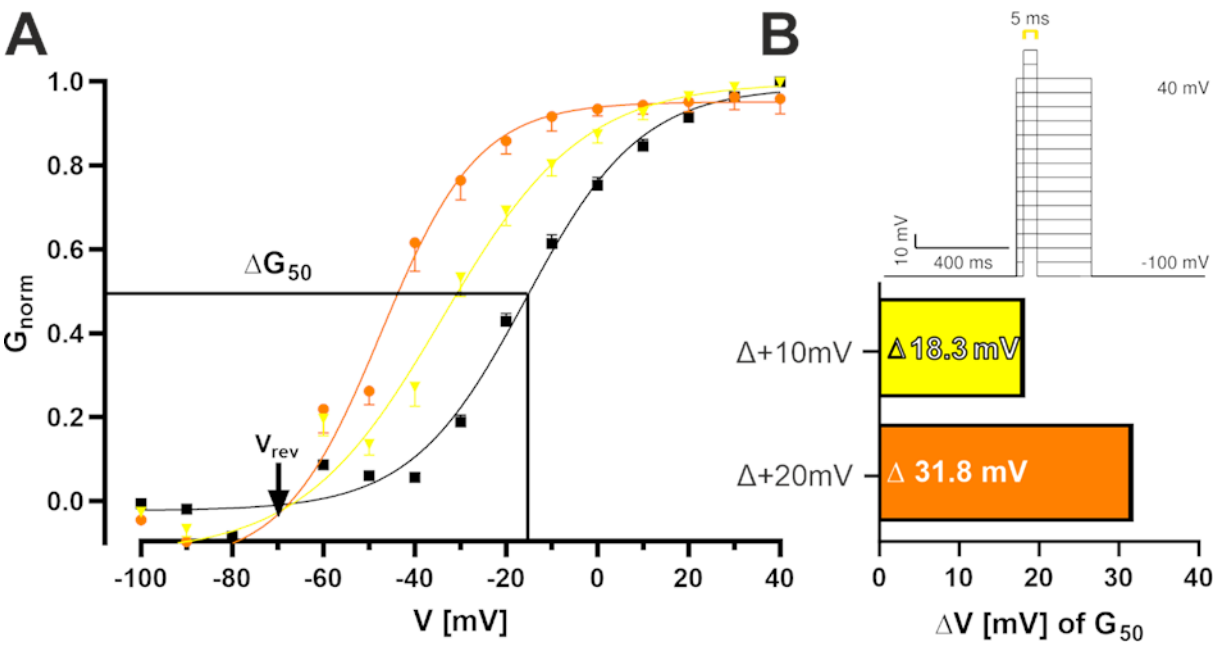

Figure 61 GV plot of stHEK293$_{Kv1.3}$ cells stimulated with different depolarization steps instead of light. (A) Normalized conductance with mean values (±SEM) for no light illumination (black – n = 17) or 5 ms additional depolarization steps with +20 mV (orange – n = 5) and + 10 mV (yellow – n = 5). (B) Inset of the step protocol and shift of the half maximal conductance ΔG_{50} derived from the additional depolarization steps towards a more negative potential compared to the K_v1.3 conductance.

When comparing the conductance shift of the +20 mV depolarization step with the effect of the OEPC-induced stimulation with full light intensity, one observes a similar shift of around 30 mV toward a more negative potential. In other words, photocapacitive OEPC depolarization is as effective as an additional +20 mV depolarization step with the patch clamp amplifier. However, one must consider that the OEPCs stimulate only a third of the membrane area, while the patch clamp amplifier stimulates the whole surface and all ion channels.

3.2.5 Effect of OEPCs on Neurostimulation

Ion channels are a well-understood and reliable system to investigate cell stimulation, channel gating, and membrane polarization, but neuronal cell cultures are more complex and offer the advantage of being closer to physiological *in vivo* conditions. Therefore, we decided to use a mixture of glial and neuronal cells (DIV14-21) derived from the hippocampus of *Rattus norvegicus* (P0-1) that easily form an interconnected neuronal network *in vitro*. We also introduce a further development of OEPCs that have the same basic architecture as the previous ones (30 mm ITO-glass and a 13 mm pixel with pn-layer) but the devices were modified with a thin layer of PEDOT:PSS covering the whole surface. This increases volumetric capacitance and allows for extended charging (Figure 63 A).

Classical Neurostimulation with an Amplifier

It is important to evaluate whether neurons are healthy and excitable. To verify this, we applied a ramp protocol (Figure 62 A) in voltage clamp and perforated patch configuration to all neurons before each experiment. The threshold potential can be calculated with the slope of the ramp (0.07 V s^{-1}) and the time point of the first AP (Figure 62 B – 487 ms ≙ -36mV). The current trace of the APs shows the characteristic inward current caused by the influx of Na^+ followed by an outward current of K^+ ions

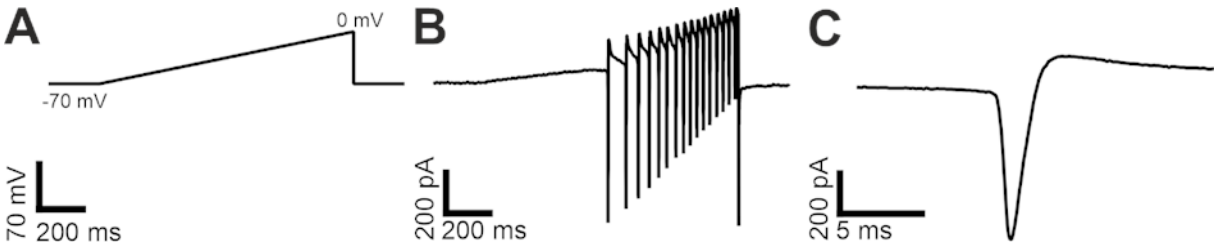

Figure 62 Validation of neuronal activity. (A) Ramp protocol for voltage clamp measurements with 0.07 V s^{-1}. (B) Representative current trace of a single neuron that fires an AP starting at 487 ms. (C) Zoom into the ionic currents evoked by an AP.

leaving the cell (Figure 62 C). Since we use a heterogeneous neuron population, parameter like the current amplitude can differ because neuronal cells such as pyramidal neurons or Purkinje cells also differ in size, ion channel composition, and spiking behavior. However, the overall shape of the excitatory currents remains the same.

After checking for responsiveness, neurons were voltage clamped with a depolarizing step protocol (Figure 63 B - inset). As expected, the neurons show no activity during the command voltages between -70 mV (Figure 63 C) and -40 mV. When clamped to the threshold potential at -35 mV, the first excitatory currents of an AP appear (Figure 63 B - orange trace and D). Succeeding depolarization steps lead to multiple APs.

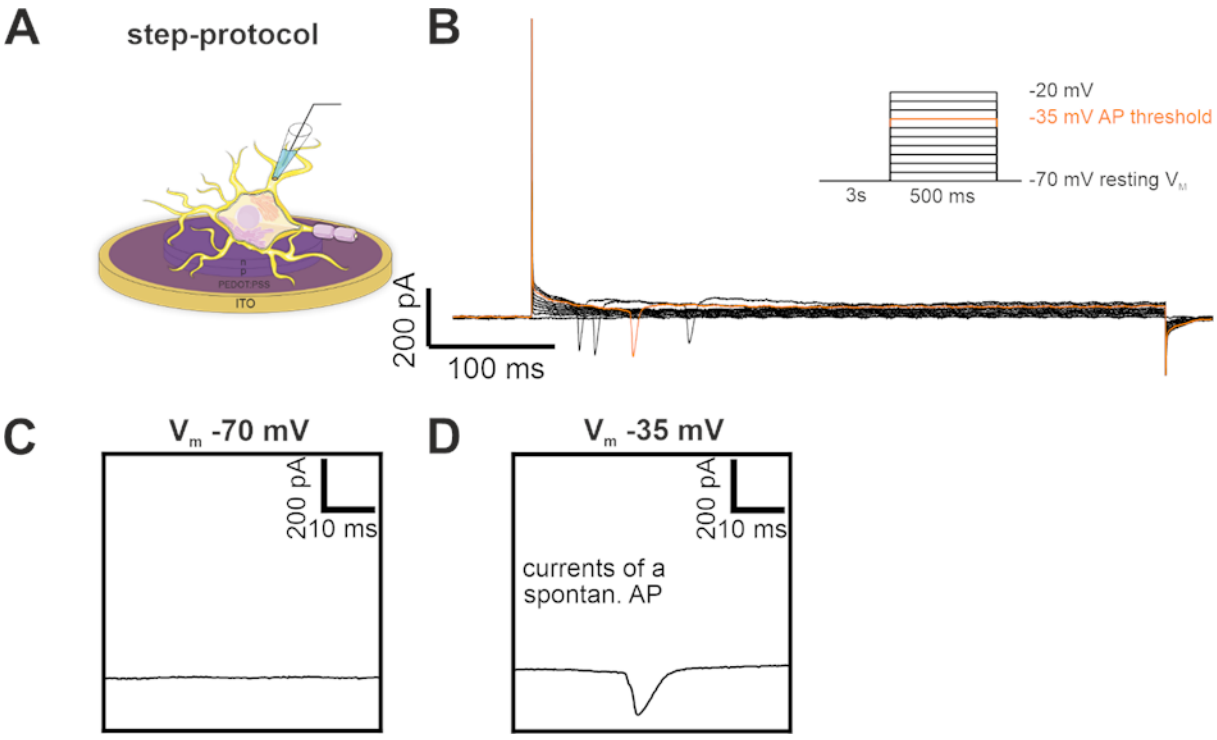

Figure 63 Step protocol stimulation for primary neurons. (A) Schematic experimental set-up with PEDOT:PSS spin-coated OEPCs and cells (not to scale). (B) Representative current traces for spontaneous APs (n = 17) and the protocol (inset). (C) Current at resting membrane potential. (D) Excitatory ionic currents at threshold potential. Adapted and reproduced with permission from John Wiley and Sons: Advanced Materials Technologies, [20], under the terms of the Creative Commons CC BY license.

Light Stimulation of OEPCs

In the next step, I wanted to induce the firing of APs by photocapacitive stimulation (Figure 64 A). The previous experiment was repeated with three additional 20 ms light pulses (26 mW mm^{-2}) at the beginning, in the middle and at the end of the voltage steps (Figure 64 B). The light pulses itself produce a positive and a negative transient when the light source is switched on and off (Figure 64 B). When zooming into the trace of the first light pulse, one can observe an elevated current flow that is interrupted by the excitatory current profile of an AP (Figure 64 C). AP firing was reliably induced at threshold potentials (n = 12), but more importantly, APs were also induced at any holding potential and throughout the whole step protocol at all three time points. AP currents at resting membrane potentials (-70 mV) appear in the middle of the light pulse, while currents in pre-depolarized protocol steps (-65 mV to -20 mV) have an earlier onset that is shifting closer to the positive transient because the effect of photocapacitive stimulation and the voltage clamp add up at the membrane.

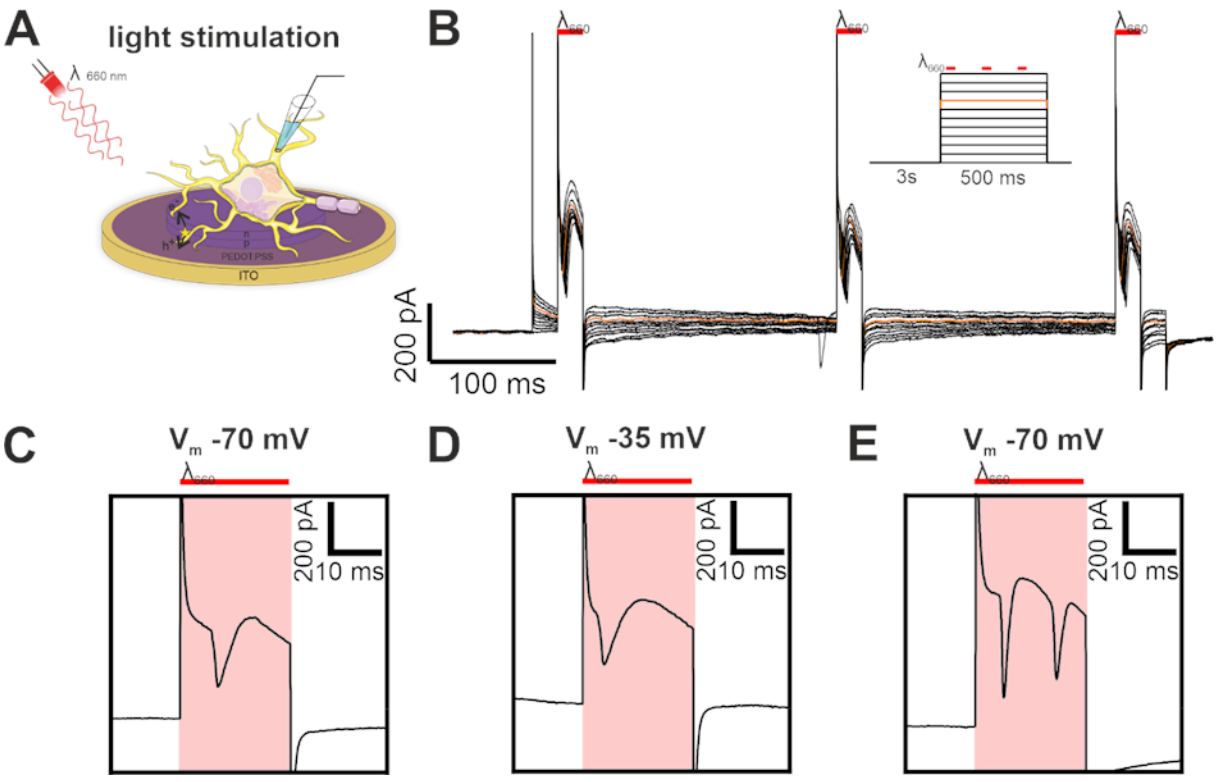

Figure 64 Light stimulation protocol for primary neurons. (A) Schematic experimental set-up with a 660 nm light source, PEDOT:PSS spin-coated OEPCs and cells (not to scale). (B) Representative current traces for light induced APs (n = 12) and the protocol (inset). (C) Ionic current of an AP at resting membrane potential with capacitive transients from the light stimulation (red). (D) Excitatory ionic currents at threshold potential. (E) Multiple APs at resting membrane potential. Adapted and reproduced with permission from John Wiley and Sons: Advanced Materials Technologies, [20], under the terms of the Creative Commons CC BY license.

Light-induced APs appeared between -70 mV and -40 mV only within the stimulus pulse whereas additional excitatory currents appeared next to the light pulse, when the cell membrane was clamped to threshold potentials (-35 mV) and higher (Figure 64 B). In some recordings we also observed multiple APs during the 20 ms light pulse (Figure 64 E) even at resting membrane potentials.

Many different ion channels activate during various phases of an AP. The following experiments are designed to prove that photocapacitive stimulation of APs is initiated by voltage-gated sodium channels and that the observed inward current within the light pulse is not caused by e.g. calcium flux. Therefore, neurons were perfused with tetrodotoxin (TTX), a potent sodium channel blocker (Figure 65 A). The applied step protocol and the light stimulation conditions (Figure 65 B) were the same as in previous experiments. No excitatory currents due to AP firing were observed, neither at the resting membrane (Figure 65 C) nor at the threshold potential (Figure 65 D) and not within the light pulse or next to it. The traces showed only capacitive transients caused by the light switch.

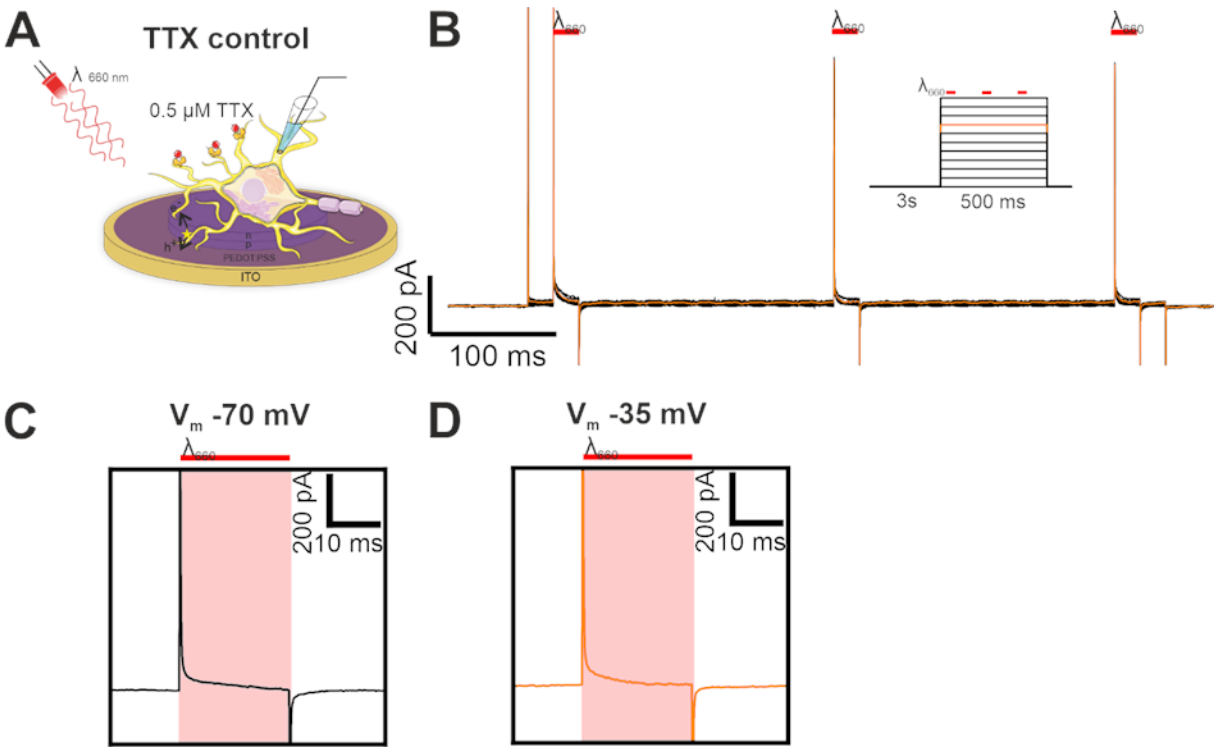

Figure 65 Light stimulation protocol for primary neurons blocked by TTX. (A) Schematic experimental set-up with a 660 nm light source, PEDOT:PSS spin-coated OEPCs and cells perfused in a 0.5 x 10^{-6} M TTX solution (not to scale). (B) Representative current traces for TTX blocked neurons (n = 8) and the protocol (inset). (C) Resting membrane potential with capacitive transients from the light stimulation (red). (D) Currents at threshold potential without ionic currents of an AP. Adapted and reproduced with permission from John Wiley and Sons: Advanced Materials Technologies, [20], under the terms of the Creative Commons CC BY license.

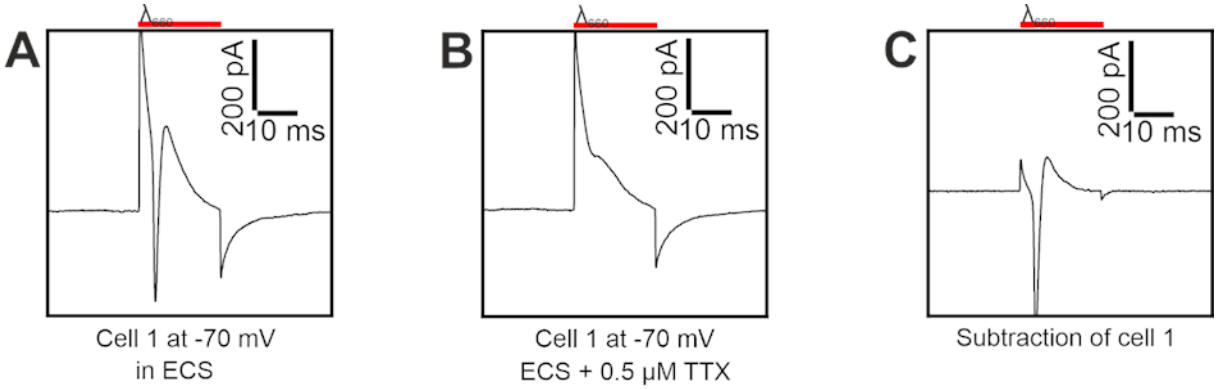

Figure 66 Subtraction of representative current traces recorded from primary neurons (A) before and (B) after the perfusion with 0.5 x 10^{-6} M TTX on PEDOT:PSS spin-coated OEPCs (C) Ionic current of an AP at resting membrane potential with the inward current of voltage-gated sodium channels and the outward current of voltage-gated potassium channels. Adapted and reproduced with permission from John Wiley and Sons: Advanced Materials Technologies, [20], under the terms of the Creative Commons CC BY license.

I first measured the current profile of a neuron before TTX perfusion (Figure 66 A) and subtracted than the current profile of the same cell after the addition of the sodium channel blocker (Figure 66 B). The hypothesis is that TTX blocks Na^+ channel gating and therefore AP initiation. The subtraction also allows to eliminate the capacitive currents and transients. The resulting subtracted traces showed minor capacitive transient artifacts. But more important, the experiment gives clear evidence that the inward current is an excitatory current caused by the sodium flux into the cell (Figure 66 C). Moreover, one can also observe an outward current that corresponds to the potassium efflux out of the cell that only emerges together with the opening of voltage-gated sodium channels.

Control Stimulations

Previous experiments have shown that OEPCs activate ion channel gating, depolarize cell membranes, and induce AP firing. Next, the depolarizing effect of photocapacitive stimulation was closely compared with the depolarizing holding potential that is artificially introduced by the patch clamp amplifier (Figure 67 A). As positive control, a step protocol was used that introduces an additional command voltage step to 0 mV of similar length instead of a 20 ms light pulse to generate an AP. Note that these experiments were carried out primarily with the same neurons as in Figure 65 but before TTX perfusion.

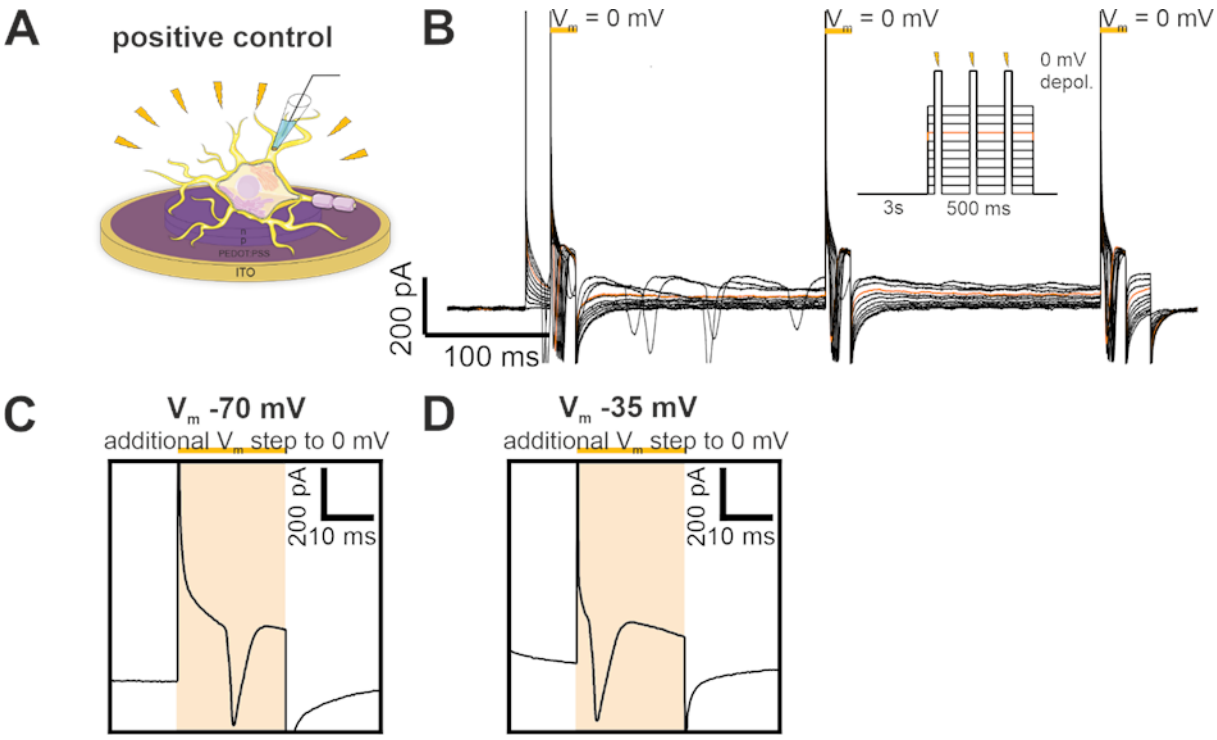

Figure 67 Control stimulation protocol for primary neurons. (A) Schematic experimental set-up with PEDOT:PSS spin-coated OEPCs and cells (not to scale). (B) Representative current traces for APs induced by an additional voltage step to 0 mV (n = 15) and the protocol (inset). (C) Ionic current of an AP at resting membrane potential with capacitive transients from the command voltage (red). (D) Excitatory ionic currents at threshold potential. Adapted and reproduced with permission from John Wiley and Sons: Advanced Materials Technologies, [20], under the terms of the Creative Commons CC BY license.

The switch of command voltages induces capacitive transients at the beginning and at the end of the depolarization pulses similar to the transients induced by the light switch. Furthermore, the stimulation pulse triggered, as expected, an AP at the resting membrane potential (-70 mV) (Figure 67 C) and all subsequent holding potentials (-65 mv to -20 mV) (Figure 67 D). Spontaneous APs rise outside of the pulse only at threshold potentials and above (Figure 67 B).

Since the positive controls result in traces that cannot be differentiated from those of the light stimulation, one can assume that OEPCs are at least as effective to activate voltage-gated ion channels in the attached membrane as the depolarization of the whole cell that is induced by the patch clamp amplifier.

Thermocapacitive effects on or photoporation of the cell membrane could potentially induce AP firing. To confirm the photocapacitve nature of OEPC stimulation and to rule out photothermal effects that might be caused by the light source, experiments were performed that use a modified nonfunctioning

device version. Instead of a photoactive pn-layer, a light absorbing layer of indigo, was deposited on the metal back electrode. This device contained, exactly as the working devices, a thin layer of spin coated PEDOT:PSS on the surface (Figure 68 A). Indigo was chosen as control pigment since it also has a good absorption in the wavelength spectrum of red light.

The step protocol shows no significant current flow and only little transient artifacts produced by the light source (Figure 68 B). One could not observe any AP currents during the stimulation regardless of the holding potential (Figures 68 C and D). At threshold potential, spontaneous AP arise but just besides the light pulses (Figure 68 E), which proves that the light itself has no influence on AP generation and a functioning OEPC device causes the stimulation.

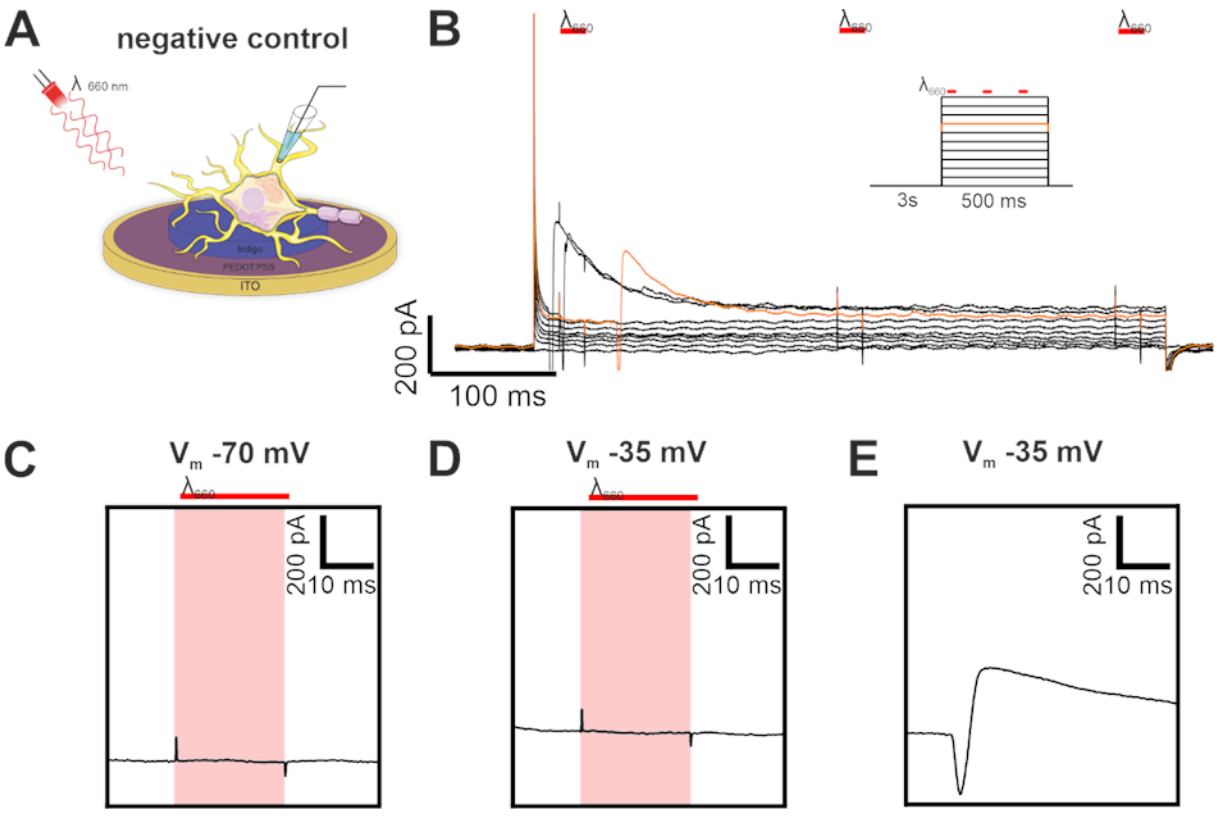

Figure 68 Influence of the light pulse on primary neuron stimulation. (A) Schematic experimental set-up with a 660 nm light source, a light absorbing indigo device with PEDOT:PSS spin-coating and cells (not to scale). (B) Representative current traces show no effect caused by light pulses (n = 6); stimulation protocol (inset). (C) Resting membrane potential with minor artifacts from the light pulse (red). (D) Currents at threshold potential during a pulse without APs and (E) besides a pulse with a spontaneous AP. Adapted and reproduced with permission from John Wiley and Sons: Advanced Materials Technologies, [20], under the terms of the Creative Commons CC BY license.

The Influence of Different Light Pulse Parameters on Neurostimulation

So far, I have investigated the influence of OEPC stimulation on neurostimulation. But changing stimulation parameter such as the pulse length or intensity also might affect the generation of APs. To characterize these parameters, we clamped cells in a perforated patch voltage clamp configuration. Without light stimulation, the voltage step protocol elicited spontaneous APs only at threshold potentials (-35 mV) or higher (Figure 69 A – yellow traces). When stimulating the OEPCs with an additional 20 ms light pulse (26 mW mm^{-2}), APs were induced at resting membrane potentials within

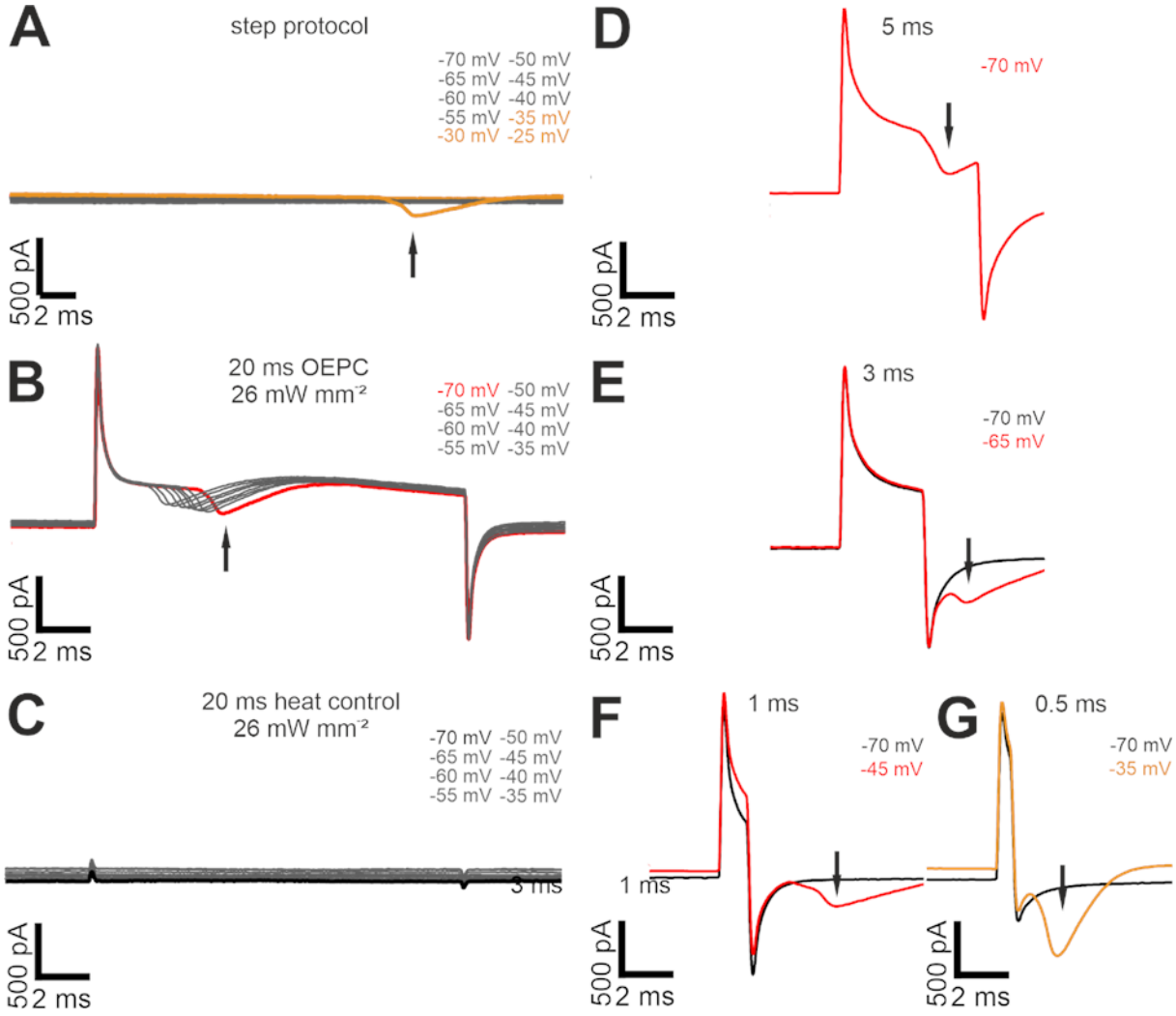

Figure 69 Comparison of light pulse lengths and the current time course in voltage clamp. Representative traces of (A) currents recorded from primary neurons during a step protocol without light stimulation (n = 12), (B) with a 20 ms of a 660 nm light pulse on an OEPC (n = 12) or (C) on an indigo heat control device (n = 6). (D – G) Different light pulse lengths tested on an OEPC (n = 12). The red trace represents the holding command voltage where the first light induced AP occurs (black arrow), the yellow traces show APs at threshold potentials. Adapted and reproduced with permission from John Wiley and Sons: Advanced Materials Technologies, [20], under the terms of the Creative Commons CC BY license.

the light pulse (-70 mV – red trace) and at all subsequent holding potentials (Figure 69 B – gray traces). The indigo heat control does not produce any APs under the same conditions (Figure 69 C).

Shorter 5 ms pulses were also able to reliably induce APs at resting membrane potentials (Figure 69 D - red trace) and higher (traces not shown). Figure 69 E shows a representative neuron that fails to reliably induce APs with 3 ms pulses at V_{rest} (black trace) but generates APs at a slightly predepolarized membrane potential of -65 mV (Figure 69 E – red trace) and subsequent higher holding potentials. The excitatory current of the AP is observed to rise after the light pulse (Figure 69 E - black arrow). However, the excitatory currents of longer lasting pulses (20 ms and 5 ms), were observed within the pulse time. Short 1 ms pulses also showed excitatory currents next to the pulse, but moreover, neurons needed to be predepolarized even further to -45 mV to induce firing (Figure 69 F). Submillisecond pulses showed that they are, in principle, capable of inducing APs at resting membrane potentials, but most neurons fail to do so and need a predepolarization close to the threshold potential to see a clear causal relationship between light pulse and neuronal stimulation (Figure 69 G – yellow trace).

Photocapacitive stimulation is a fast process and is the reason for OEPC induced AP firing. We also assume that the depolarization is caused by the cathodic phase. So, one might ask why APs are not always within the light pulses. APs last around 1-3 ms which makes them last longer than the stimulation pulse. However, it takes some time for the cell membrane to capacitively charge and to reach the depolarization threshold. This can be seen in Figure 69 B where the cell needs 3-5 ms to reach the threshold potential and to show excitatory currents, depending on the predepolarization of the cell membrane.

The previous results are summarized in Figure 70 and are complemented by data showing how the change in light intensity influences the induction of APs. Longer lasting pulses (20 ms and 5 ms) were found to reliably induce AP firing at resting membrane potentials for most neurons. Furthermore, lower intensities (21 and 10 mW mm^{-2} - 20 ms light pulses) also induced APs at V_{rest} and showed no significant difference compared to the maximum light condition (26 mW mm^{-2}).

Shorter light pulses also achieved AP firing at resting membrane potentials but there is a wider distribution of neurons that need to be predepolarized for successful neurostimulation. However, most neurons show spontaneous APs around threshold potentials, while the median activation potential for light-induced APs is significantly lower for all stimulation conditions. Furthermore, all APs correlate in a timely manner with OEPC stimulation.

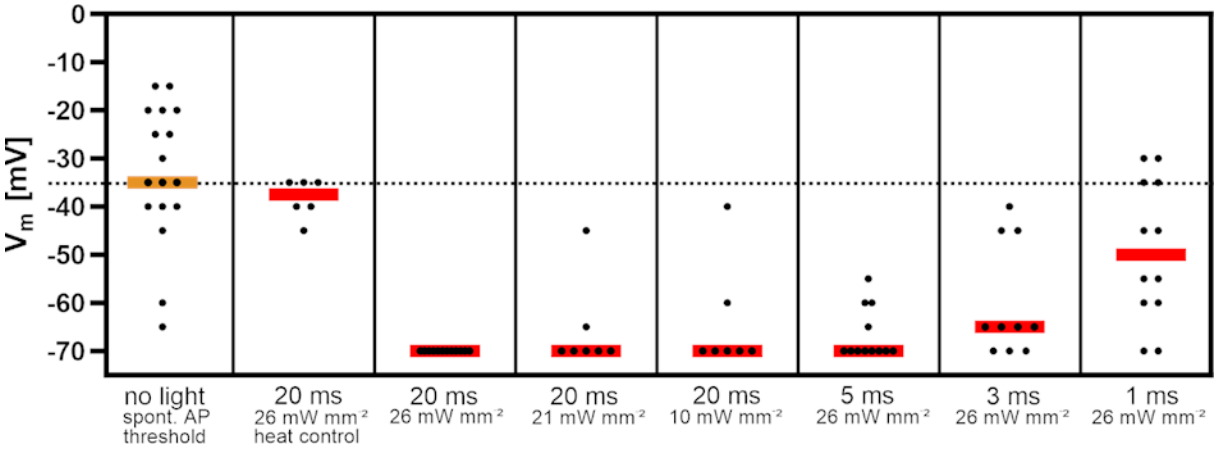

Figure 70 Overview of light pulse lengths or intensities and their influence on AP initiation. Single measurements on primary neurons (black dot) with the median (red line) of the clamped holding command voltage that is necessary for AP initiation on PEDOT:PSS spin-coated OEPCs with light. Adapted and reproduced with permission from John Wiley and Sons: Advanced Materials Technologies, [20], under the terms of the Creative Commons CC BY license.

Characterization of Light Induced Action Potentials

Voltage clamp measurements are an effective tool for the characterization of ion channel gating as well as for evaluating the potential of OEPCs to stimulate cells and to induce APs in neurons. Clamping the cell membrane to a specific potential might be useful for such comparison studies, but this might ignore the actual membrane potential or other cell properties such as cell size. Neuronal resting membrane potentials can vary slightly in *in vitro* cell cultures and clamping large cells might lead to space clamp issues. Not clamping a cell is more natural and closer to *in vivo* conditions. However, in current clamp mode, the actual membrane potential can be recorded without introducing errors when no current is injected into the cell (I = 0). Therefore, all the following experiments that characterize light stimulation were recorded in the perforated patch configuration and current clamp mode without current injection.

We used the same OEPC device design (ITO back electrode and a pn-photopixel with a spin coated PEDOT: PSS layer) and cultured on them for 2 – 3 weeks a mixture of glial and hippocampal neurons derived from rats. Healthy neurons have a typical resting membrane potential of around -70 mV ± 10 mV *in vitro*. To test the responsiveness of a neuron, a current can be injected so that the cell reaches threshold potentials.

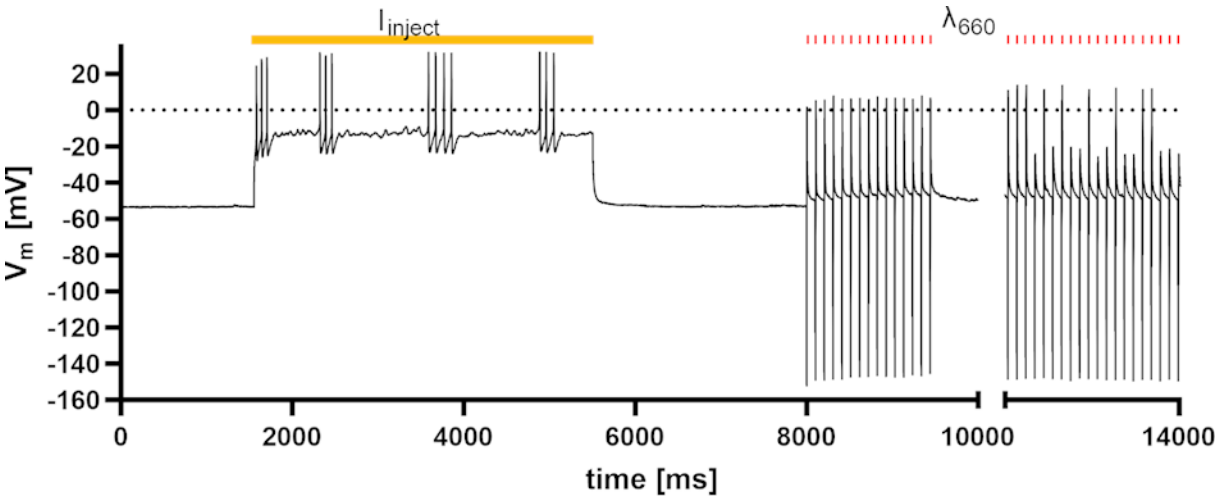

Figure 71 Stimulation protocol for primary neurons in current clamp. Representative time course of the recorded membrane potential with current injection (yellow) or 3 ms light pulses (red) on PEDOT:PSS spin-coated OEPCs. Adapted and reproduced with permission from John Wiley and Sons: Advanced Materials Technologies, [20], under the terms of the Creative Commons CC BY license.

Figure 71 shows trains of APs under current injection conditions (yellow bar) indicating that the patched neuron is healthy and excitable. The current injection was then set back to I = 0 and the OEPC was stimulated with 3 ms light pulses (Figure 71 – red bars). The neuron responded to the extracellular light stimulation with AP firing. The first sets of stimulation were able to induce APs with every single pulse (time-course between 8000 ms and 10,000 ms) but the neurons get exhausted over time and AP initiation starts to fail. This behavior is also observed with metal electrode stimulation. The negative ongoing potential is an artifact of cathodic stimulation (see below).

Recording membrane potential with an extracellular stimulation electrode has its own unique challenges. Different light intensities were tested on their effect on the light artifact and on the effect on neurostimulation (Figure 72). At very low intensities (0.4 mW mm^{-2}) the cathodic leading stimulation artifact starts to appear and increases with the intensity of the light pulses (4.6 mW mm^{-2}). The artifact reaches nominal values of up to 160 mV (26 mW mm^{-2}) but might change depending on the position of the reference electrode. However, this does not reflect the actual voltage time course of the membrane or indicate a hyperpolarization of the cell. The OEPC produces a cathodic leading current when the light is switched on. Thus, the negative voltage peak of the light artifact is the difference in the potential between the patch pipette and the reference electrode. It might be to debate whether the positive ongoing peak at 4.6 mW mm^{-2} is a graded potential of a failed AP or the counterbalancing anodic phase induced by switching the light off.

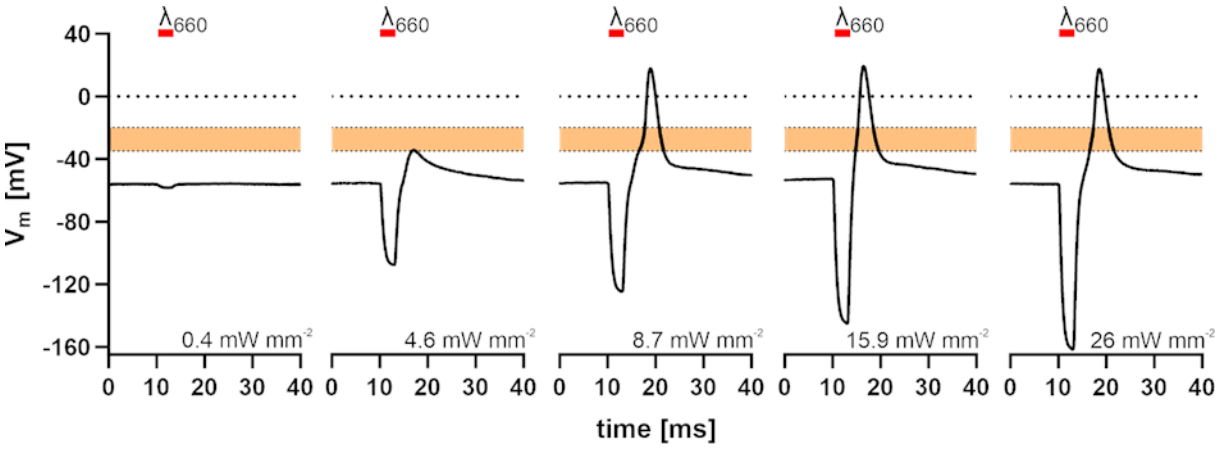

Figure 72 Light intensity comparison with 3 ms pulses and the effect on primary neurons in current clamp. Representative time course of the recorded potential on PEDOT:PSS spin-coated OEPCs with a cathodic stimulation artifact (negative ongoing) and the actual membrane potential including an AP. Adapted and reproduced with permission from John Wiley and Sons: Advanced Materials Technologies, [20], under the terms of the Creative Commons CC BY license.

However, one can observe the effect of the all-or-none law when neurons reach the threshold potential. The successful initiation of an AP always leads to the same voltage time-course and depolarization peaks. The cathodic stimulation artifact in contrast is strongly light dependent. OEPCs were able to induce reliable and repetitive APs at light intensities of around 9 mW mm^{-2}.

Next, I tested different light pulse lengths and evaluated whether this might influence AP generation. Figure 73 A shows a continuous recording of a neuron with short and long pulses. Two similar phenomena were observed that are related to previous voltage clamp experiments: Very short pulses (Figure 73 B – 1 ms) are able to successfully induce APs, but neurons have a higher tendency to fail AP initiation compared to longer pulses (3 ms – 50 ms) that always initiated APs. The second similar observation is that the AP occurs within the light pulse for long stimulations and next to the pulse for short ones. In case of the 5 ms pulse, one observes an overlap between the AP time-course and the time course of the stimulation artifact.

Some neurons failed the initial responsiveness test (see above) and current injection could not induce APs. Therefore, they also cannot produce APs during light-induced stimulation with an OEPC electrode. However, those neurons are convenient for isolating the stimulation artifact. Figure 74 shows the voltage time course of the cathodic leading stimulation artifact and the anodic counterparts. The traces illustrate that we measure indeed the overlap of the actual cell membrane potential and the stimulation artifact. However, AP initiation would not be possible at such hyperpolarized membrane potentials (-160 mV) anyhow.

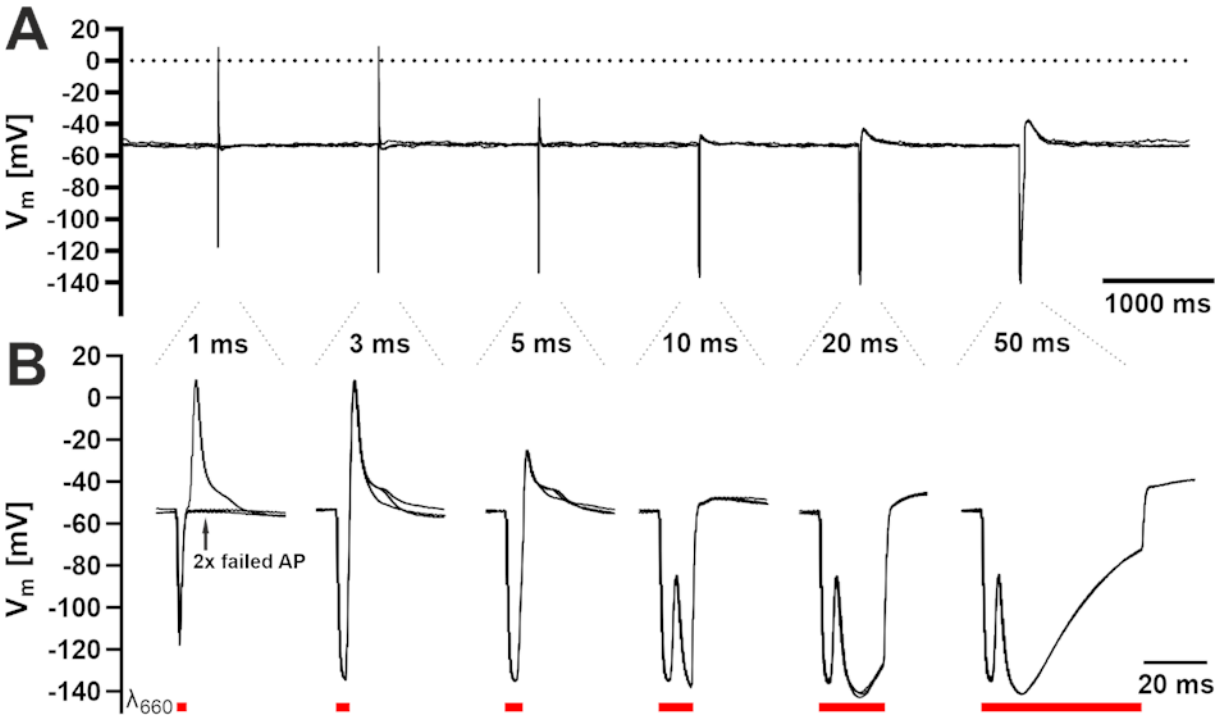

Figure 73 Light pulse length comparison and the effect on primary neurons in current clamp. (A) Representative time course of the recorded potential on PEDOT:PSS spin-coated OEPCs in a gap free recording and (B) a zoom into the different light pulse lengths with three overlaying sweeps. Adapted and reproduced with permission from John Wiley and Sons: Advanced Materials Technologies, [20], under the terms of the Creative Commons CC BY license.

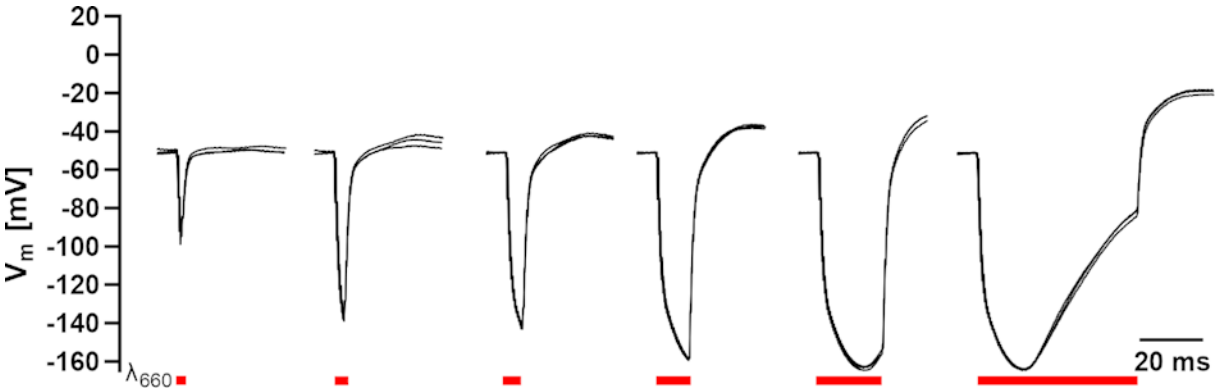

Figure 74 Light pulse length comparison and the cathodic stimulation artifact in current clamp. Zoom into the different light pulse lengths and a representative time course of the recorded potential of generally nonresponsive neurons. Overlay of three recordings of a cell on PEDOT:PSS spin-coated OEPCs in a gap free mode. Adapted and reproduced with permission from John Wiley and Sons: Advanced Materials Technologies, [20], under the terms of the Creative Commons CC BY license.

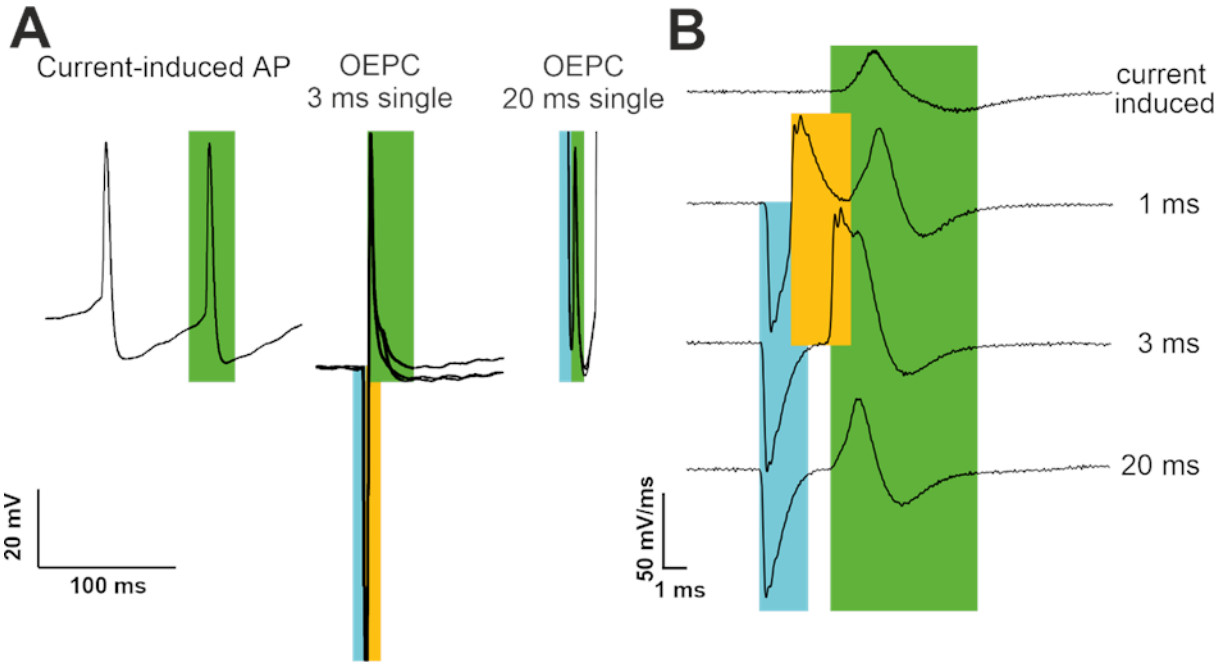

Figure 75 Comparison of the membrane potential time course and the slopes of APs. (A) Representative membrane potential of a current induced AP and two light induced APs of neurons on PEDOT:PSS spin-coated OEPCs with different pulse lengths. (B) Slopes of the rise and decay times of the time courses with the depolarization and repolarization phase (green), the negative ongoing of the cathodic stimulation artifact (blue) and the positive one (yellow). Adapted and reproduced with permission from John Wiley and Sons: Advanced Materials Technologies, [20], under the terms of the Creative Commons CC BY license.

Lastly, we compared the depolarization amplitude and the slopes of APs. Current-injected APs show all common characteristics of a regular AP with an initiation, depolarization, repolarization, and hyperpolarization phase (Figure 75 A). The amplitude of a light-induced AP is not different from the regular one despite the occurrence within the cathodic stimulation artifact (20 ms) or next to it (3 ms). All APs were found to have similar rise and decay times (Figure 75 B) for their depolarization and repolarization phases (green). To better differentiate between the slopes of the AP and the artifact, the negative ongoing of the stimulation artifact is highlighted in blue and the positive ongoing in yellow.

In the end, all experiments carried out within this part of the thesis could prove that OEPCs are free-standing extracellular stimulation electrodes that reliably induce physiological APs *in vitro* in mammalian cells with single light pulses and that this stimulation can be as effective as wired metal electrodes.

4 Summary and Discussion

Summary

In this thesis, I have demonstrated that novel organic bioelectronics can be wirelessly driven with light to polarize cell membranes and consequently to stimulate neuronal activity in mammalian cells *in vitro*. Epindolidione pigment 3D microstructures offer cell membranes and neuronal extensions such as axons or neurites a large and structured surface to attach to. Photothermocapacitive stimulation depolarized cell membranes but this might not be sufficient to excite neurons. However, planar photovoltaic electrodes with two semiconducting organic pigments have proven to actively influence ion channel gating in nonexcitable cells and to facilitate neurostimulation. The photocapacitive stimulation mechanism of thin-film OEPC devices mimics the mechanism of conventional wired extracellular stimulation metal electrodes. Light-induced charge separation within the device leads to a biphasic cathodic leading charge-balanced stimulation that is assumed to be the most gentle way to excite cells [98]. The effective and timely precise *in vitro* light stimulations presented in this thesis might inspire a wide variety of *in vivo* applications and are a promising starting point for future stimulation implants.

Bioelectronic Considerations to Photothermocapacitive Stimulation

Photothermal heating requires a transducer that absorbs light and generates a temperature change to heat its environment. The most simple transducer is water which causes tissue heating by absorbing infrared light and an increase of the electrical capacitance on the cell membrane [116]. Direct heating was successfully used for peripheral nerve stimulation [161], optical heart pacing [162], or laser stimulation of the auditory nerve [163]. The advent of inorganic transducers such as gold nanoparticles [141] or silicon-based materials [143, 164-166] facilitated this development but often lack biocompatibility or need to be assessed in long-term studies and *in vivo* [167, 168]. Planar organic polymers such as P3HT [142] and PCBM [169] were investigated for *in vitro* neurostimulation. Furthermore, 3D-shaped structures based on crystalline pigments [103] showed a close interface between cell membranes and biomolecules. In this thesis, epindolidione microstructures were shown to grow large crystalline pigment plates and needles that offer a large surface area for cell attachment. Cell membranes grow over the microstructures and even adapt their shape according to the pigment geometry. In addition, neurons were shown to include microstructures in their network formation by remodeling connections to and from the pigment surface. The strong bond to the pigment surface and the large interaction site with the cell membranes were an encouraging starting point for further

stimulation experiments. The epindolidione microstructures depolarized cell membranes with a median of 4.5 mV for 50 ms and 100 ms pulses but this could not excite neuronal membranes. Other groups achieved 0.6 mV with oocytes or 2.7 mV in HEK293 cells and water as transducer [116] or attempted to stimulate planar organic P3HT biopolymers resulting in even lower membrane polarizations of 0.4 mV to 1 mV with up to 57 mW mm^{-2} laser intensities [142]. The latter used planar structures that developed minor transients (less than 5 pA) when measuring the current across the membrane, while epindolidione microstructures developed photoinduced transients of more than 50 pA. A similar pigment, quinacridone, exhibited transients of up to 100 pA and induced a constant current flow in cells overexpressing TRPV1 [103]. The reasons why such pigments struggle to induce APs may be diverse but one key aspect is the rate of temperature change that increases cell capacitance when heating the membrane [115, 116]. Large surface areas facilitate a higher temperature change [103]. Epindolidione has a large interface with the membrane and absorbs the applied wavelength (450 nm) very well, but the light-induced rate of capacitance change might be too slow for neuro excitation. We used light pulses between 10 ms and 100 ms. However, computer simulations of transducer heating suggest that membranes require a temperature change of 3.7 K within 1 µs to 1 ms to successfully induce AP firing. Longer heating times just reached subthreshold depolarizations [151]. Another aspect is the difficulty of delivering light to photoactive transducers. Micro LEDs are often used [170, 171] for *in vivo* stimulation. Their successful application in optogenetic approaches is undisputed but whether those devices might deliver enough power to heat transducers remains elusive. We experienced problems with laser alignments and cell depolarization dramatically decreased when the laser spot was out of focus or not directly targeted to single epindolidione crystals. For experiments, only cells were selected that had one or two microstructures attached. A possibility to increase heat delivery could be a broader laser spot targeted at cells whose surface is covered with more microstructures. One should keep in mind that higher concentrations of photoactive nanoparticles have been reported to have negative effects on cell viability [168, 172-174]. Whether this applies to microstructures or to how stable epindolidione pigment platelets are under rapid thermal heating, remains elusive. The last aspect to consider is the general architecture of the device. Material compositions that form organic bulk heterojunctions [169] or inorganic pn junctions [164] have been reported to induce APs but the authors describe both stimulation mechanisms most likely to be faradaic in nature. Hence, the main focus of this thesis was shifted to explore the cell stimulation properties of another safer photocapacitive stimulation method.

Photocapacitive Activation and Gating of Ion Channels

Optical control of channel gating often refers to genetically modified [175, 176] and thermosensitive ion channels [177] or to thermogenetics that manipulate animal behavior with light [178]. However, nongenetic and nonphotothermal approaches face the problem of being hard to distinguish between photofaradaic mechanisms and other mechanisms, which requires careful device design and characterization. Thin-film OEPCs were extensively tested and found to be photocapacitve [138]. However, capacitive stimulation electrodes require a close contact with cell membranes to be effective. This thesis shows how mammalian cells and especially neurons attach to different OEPC surfaces, grow extensions such as filopodia or neurites to the crystalline pigments, or even penetrate the device. This indicates that OEPCs are more than just biocompatible, they also offer neurons a preferential adhesion surface compared to polished inorganic metal electrodes [109]. The rough pigment surface facilitates cell attachment and allows for close interactions with cell membranes. The cell membrane accommodates a wide variety of different ion channels. For neurons, most of the voltage-gated ion channels responsible for AP initiation are located in the proximal axon compartment called the AIS (axon initial segment). The main driving force for cell depolarization during APs are voltage-gated Na^+ channels that inactivate rather fast and are not conductive over a wide span of membrane potentials. This makes Na^+ channels inapplicable since a convenient cell model system has to account for experimental setting changes such as light pulses that might last longer than the channel gating or a wide span of holding potentials applied via the patch clamp pipette. Therefore, we developed and characterized [179] a cell line expressing the shaker-related voltage-gated K^+ channel that also allows to differentiate between gating currents and photocapacitive transients. $K_v1.3$ is a delayed rectifying ion channel that shows little inactivation and robust gating of ionic currents throughout voltage clamp measurements. Many delayed rectifying channels are involved in the repolarization phase of APs under regular neurophysiological conditions. This work has proven that light stimulation of OEPCs successfully polarizes membranes and shifts the conductance of voltage-gated channels toward more negative potentials, allowing an effective cell stimulation at resting membrane potentials. Heat-induced and faradaic stimulation mechanisms are well known to depolarize cells but there is little knowledge about capacitive stimulation. We hypothesized that the transient electric field created between the photopixel and the back electrode might influence the voltage sensor of voltage-gated ion channels that are close to the OEPC interface. However, the patch clamp technique allows only to record the current flow across the whole membrane. One can directly measure the influence of the light stimulation and the induced channel gating, but the patch clamp technique does not allow a distinction between gating events that happen at the attached membrane

or the free membrane. Therefore, we developed a computational model that simulated $K_v1.3$ ion channel gating based on the results of this thesis [20]. We could show that, in accordance with the two-domain model [109], both membrane patches polarize during and after light stimulation. The attached membrane experiences a strong depolarization when the light is switched on, which allows voltage-gated ion channels to open. The free membrane slightly hyperpolarizes and does not contribute to channel gating. Switching off the light reverses the polarity of both membranes. The simulations support experimental findings and the evidence for photocapacitive cell stimulation.

OEPC-induced Neurostimulation

Voltage clamp measurements of voltage-gated ion channels provide valuable insight in characterizing cell stimulation with OEPCs, but they also require a careful experimental design and adjustment of cell parameters such as ion channel composition and membrane potential. However, complex neuronal networks and the recording of membrane potentials in the current clamp (I = 0 mode) allow for a more physiological environment to investigate OEPC-mediated neuronal signaling. OEPC devises are designed in such a way that they provide a charge-balanced cathodic leading extracellular stimulation. Nevertheless, one might also use the discharging properties of OEPCs or an anodic-leading stimulation pulse generated by a positively charged surface in device designs that reverse the arrangement of the pn-layer. Both approaches might have the potential to induce AP firing, but cathodic-leading stimulation is more advantageous for several reasons, when using light as an energy source. Most ion channels are uniformly distributed within the cell membrane. As a target for membrane depolarization, the free membrane would allow for more ion channel gating. However, capacitive stimulation is a transient process that requires a close coupling between the membrane and the stimulation electrode. Creating an electric field that might affect the free membrane would require more powerful devices such as metal electrodes with an electrical connection to a power source. Light-driven OEPCs are thin film devices that enable the design of flexible and biocompatible implants for *in vitro* and *in vivo* use without the need for an external power supply. The cathodic activation of ion channels in the attached membrane is safer, mimics a more natural cell stimulation, and requires less energy because of the proximity to the electrode. Another major advantage of OEPC devices is the direct control of neuronal signaling. I could effectively and repetitively induce AP firing at resting membrane potentials with single light pulses ranging from 1 ms to 50 ms. Organic bulk heterojunctions with PTB7-Th, PC71BM or similar molecules required continuous trains of light pulses [180, 181] to achieve only single APs within stimulation periods that lasted up to 100 ms. Other attempts required pre-depolarized resting

membrane potentials to be effective. Also, capacitive metal electrodes relied on several pulses to gradually depolarize cell membranes and to activate Na^+ channels [140]. However, the photostimulation mechanism with P3HT surfaces [169, 182, 183] and an observed vision restoration in rats [184] remains unclear and subject to debate [20, 185]. Other stimulation approaches with silicon [186] or gold nanoparticles [141] might be non-faradaic, localized [141], and less invasive [143] but have also been reported to be thermocapacitive instead. The sum of the results within this thesis reveals how effective OEPCs are compared to other devices for light-mediated neurostimulation.

Biological Context and Application

The material properties of OEPC devices, as well as their charging and discharging behavior have been well characterized [136-138, 187]. In addition to ion channel gating, I could activate mammalian hippocampal neurons *in vitro* and induce AP firing at resting membrane potentials with light. However, the recorded membrane potential shows a negative potential during the light pulse. This stimulation artifact is caused by the patch clamp electrode, which measures the actual cell membrane potential and the overlapping potential drop between the extracellular stimulation electrode and the ground. Neurons would not generate APs when their membranes would actually feel such a hyperpolarization. However, this artifact and the hyperpolarization of the free membrane showed no limiting effects for *in vivo* experiments or for the here presented generation of neuronal APs. All mentioned mechanistic characterizations and neurophysiological insights led to the recent development of implants for the successful stimulation of the sciatic nerve [188], the somatosensory cortex [189], and deep brain stimulation of rodents [190]. In addition to controlling behavioral patterns, promising new developments further indicate that the OEPC technology also has the potential to influence gene expression through neurostimulation and to activate regenerative processes after neurotraumatic events.

5 Abbreviations and Definitions

AIS	axon initial segment	**Na^+**	sodium
AP	action potentials	**OEPC**	Organic Electrolytic Photocapacitor
AUC	area under the curve	**OTS**	octyltriethoxysilane
c	concentration	**P3HT**	poly(3-hexylthiophene-2,5-diyl)
Cl^-	chloride	**PAP-1**	(5-(4-Phenoxybutoxy)psoralen)
C_m	membrane capacitance	**PBS**	Phosphate Buffered Saline solution
DMEM	Dulbecco's Modified Eagle's Medium	**PC71BM**	(6,6)-Phenyl C71 butyric acid methyl ester, mixture of isomers
DMSO	dimethylsulfoxide	**PEDOT**	poly(3,4-ethylenedioxythiophene)
EGF	epidermal growth factor	**PSS**	polystyrene sulfonate
EGTA	(3,12-Bis(carboxymethyl)-6,9-dioxa-3,12-diazatetradecane-1,14-dioic acid)	**PTB7-Th**	Poly[4,8-bis(5-(2-ethylhexyl)thiophen-2-yl)benzo[1,2-b;4,5-b']dithiophene-2,6-diyl-alt-(4-(2-ethylhexyl)-3-fluorothieno[3,4-b]thiophene-)-2-carboxylate-2-6-diyl)]
E_{ion}	Nernst potential	**PTCDI**	N,N'-dimethyl perylene tetracarboxylicdiimide
EMF_{ion}	electromotive force	**PVD**	physical vapor deposition
ETL	electron transfer layer	**PVs**	photovoltaics
F	Faraday constant	**Q**	charge
FBS	Fetal Bovine Serum	**R**	gas constant
FGF	fibroblast growth factor	**R**	arginine
G	conductance	**R**	resistance
GABA	γ-aminobutyric acid	**T**	temperature
H_2Pc	metal free phthalocyanine	**TTX**	tetrodotoxin
HEK	human embryonic kidney	**V**	potential
HTL	hole transfer layer	**V_m**	membrane potential
ITO	indium tin oxide	**V_{rest}**	resting membrane potential
K	lysine	**V_s**	surface charge potential
K^+	potassium	**z_{ion}**	number of valence electrons

6 List of Figures

7 Bibliography

1. Rogan SC, Roth BL. Remote control of neuronal signaling. Pharmacological reviews. 2011;63(2):291-315.

2. Inayat S, Rountree CM, Troy JB, Saggere L. Chemical stimulation of rat retinal neurons: feasibility of an epiretinal neurotransmitter-based prosthesis. Journal of neural engineering. 2015;12(1):016010.

3. Cook-Snyder DR, Miller JR, Navarrete-Opazo AA, Callison JJ, Peterson RC, Hopp FA, et al. The contribution of endogenous glutamatergic input in the ventral respiratory column to respiratory rhythm. Respiratory Physiology & Neurobiology. 2019;260:37-52.

4. Negrini-Ferrari SE, Medeiros P, Malvestio RB, de Oliveira Silva M, Medeiros AC, Coimbra NC, et al. The primary motor cortex electrical and chemical stimulation attenuates the chronic neuropathic pain by activation of the periaqueductal grey matter: The role of NMDA receptors. Behavioural Brain Research. 2021;415:113522.

5. Mohrmann R, Lessmann V, Gottmann K. Developmental maturation of synaptic vesicle cycling as a distinctive feature of central glutamatergic synapses. Neuroscience. 2003;117(1):7-18.

6. Terrell ML, Kadekaro M, Freeman S, Eisenberg H. Effects of chemical stimulation of the subfornical organ on metabolic activity of the hypothalamo-neurohypophysial system in rats. Neuroscience Letters. 1991;134(1):122-6.

7. Lin MT, Ho MT, Young MS. Stimulation of the nigrostriatal dopamine system inhibits both heat production and heat loss mechanisms in rats. Naunyn-Schmiedeberg's archives of pharmacology. 1992;346(5):504-10.

8. Jones PD, Stelzle M. Can Nanofluidic Chemical Release Enable Fast, High Resolution Neurotransmitter-Based Neurostimulation? Frontiers in neuroscience. 2016;10:138.

9. Bouton CE, Shaikhouni A, Annetta NV, Bockbrader MA, Friedenberg DA, Nielson DM, et al. Restoring cortical control of functional movement in a human with quadriplegia. Nature. 2016;533(7602):247-50.

10. Davis TS, Wark HA, Hutchinson DT, Warren DJ, O'Neill K, Scheinblum T, et al. Restoring motor control and sensory feedback in people with upper extremity amputations using arrays of 96 microelectrodes implanted in the median and ulnar nerves. Journal of neural engineering. 2016;13(3):036001.

11. Hottowy P, Skoczeń A, Gunning DE, Kachiguine S, Mathieson K, Sher A, et al. Properties and application of a multichannel integrated circuit for low-artifact, patterned electrical stimulation of neural tissue. Journal of neural engineering. 2012;9(6):066005.

12. Baba T, Kameda M, Yasuhara T, Morimoto T, Kondo A, Shingo T, et al. Electrical stimulation of the cerebral cortex exerts antiapoptotic, angiogenic, and anti-inflammatory effects in ischemic stroke rats through phosphoinositide 3-kinase/Akt signaling pathway. Stroke. 2009;40(11):e598-605.

13. Jahanshahi A, Schonfeld L, Janssen ML, Hescham S, Kocabicak E, Steinbusch HW, et al. Electrical stimulation of the motor cortex enhances progenitor cell migration in the adult rat brain. Experimental brain research. 2013;231(2):165-77.

14. Brown JA, Lutsep HL, Weinand M, Cramer SC. Motor cortex stimulation for the enhancement of recovery from stroke: a prospective, multicenter safety study. Neurosurgery. 2006;58(3):464-73.

15. Nguyen JP, Lefaucheur JP, Decq P, Uchiyama T, Carpentier A, Fontaine D, et al. Chronic motor cortex stimulation in the treatment of central and neuropathic pain. Correlations between clinical, electrophysiological and anatomical data. Pain. 1999;82(3):245-51.

16. Bansal AK, Truccolo W, Vargas-Irwin CE, Donoghue JP. Decoding 3D reach and grasp from hybrid signals in motor and premotor cortices: spikes, multiunit activity, and local field potentials. Journal of neurophysiology. 2012;107(5):1337-55.

17. Chapin JK, Moxon KA, Markowitz RS, Nicolelis MA. Real-time control of a robot arm using simultaneously recorded neurons in the motor cortex. Nature neuroscience. 1999;2(7):664-70.

18. Hochberg LR, Serruya MD, Friehs GM, Mukand JA, Saleh M, Caplan AH, et al. Neuronal ensemble control of prosthetic devices by a human with tetraplegia. Nature. 2006;442(7099):164-71.

19. Velliste M, Perel S, Spalding MC, Whitford AS, Schwartz AB. Cortical control of a prosthetic arm for self-feeding. Nature. 2008;453(7198):1098-101.

20. Schmidt T, Jakešová M, Đerek V, Kornmueller K, Tiapko O, Bischof H, et al. Light Stimulation of Neurons on Organic Photocapacitors Induces Action Potentials with Millisecond Precision. Advanced Materials Technologies.n/a(n/a):2101159.

21. Velasco F, Jiménez F, Pérez ML, Carrillo-Ruiz JD, Velasco AL, Ceballos J, et al. Electrical stimulation of the prelemniscal radiation in the treatment of Parkinson's disease: an old target revised with new techniques. Neurosurgery. 2001;49(2):293-306; discussion -8.

22. Beitz JM. Parkinson's disease: a review. Frontiers in bioscience (Scholar edition). 2014;6(1):65-74.

23. Borgens RB, Roederer E, Cohen MJ. Enhanced spinal cord regeneration in lamprey by applied electric fields. Science (New York, NY). 1981;213(4508):611-7.

24. Asplund M, Nyberg T, Inganäs O. Electroactive polymers for neural interfaces. Polymer Chemistry. 2010;1(9):1374-91.

25. Klinke R, Kral A, Heid S, Tillein J, Hartmann R. Recruitment of the auditory cortex in congenitally deaf cats by long-term cochlear electrostimulation. Science (New York, NY). 1999;285(5434):1729-33.

26. Kral A, Sharma A. Developmental neuroplasticity after cochlear implantation. Trends in neurosciences. 2012;35(2):111-22.

27. Ghezzi D. Retinal prostheses: progress toward the next generation implants. Frontiers in neuroscience. 2015;9:290.

28. Zrenner E, Bartz-Schmidt KU, Benav H, Besch D, Bruckmann A, Gabel VP, et al. Subretinal electronic chips allow blind patients to read letters and combine them to words. Proceedings Biological sciences. 2011;278(1711):1489-97.

29. Humayun MS, Dorn JD, da Cruz L, Dagnelie G, Sahel JA, Stanga PE, et al. Interim results from the international trial of Second Sight's visual prosthesis. Ophthalmology. 2012;119(4):779-88.

30. Knutson JS, Naples GG, Peckham PH, Keith MW. Electrode fracture rates and occurrences of infection and granuloma associated with percutaneous intramuscular electrodes in upper-limb functional electrical stimulation applications. Journal of rehabilitation research and development. 2002;39(6):671-83.

31. Ilfeld BM, Gabriel RA, Saulino MF, Chae J, Peckham PH, Grant SA, et al. Infection Rates of Electrical Leads Used for Percutaneous Neurostimulation of the Peripheral Nervous System. Pain practice : the official journal of World Institute of Pain. 2017;17(6):753-62.

32. Maki DG, Kluger DM, Crnich CJ. The risk of bloodstream infection in adults with different intravascular devices: a systematic review of 200 published prospective studies. Mayo Clinic proceedings. 2006;81(9):1159-71.

33. Schaffrath K, Schellhase H, Walter P, Augustin A, Chizzolini M, Kirchhof B, et al. One-Year Safety and Performance Assessment of the Argus II Retinal Prosthesis: A Postapproval Study. JAMA Ophthalmology. 2019;137(8):896-902.

34. Delitto A, Strube MJ, Shulman AD, Minor SD. A study of discomfort with electrical stimulation. Physical therapy. 1992;72(6):410-21; discussion on 21-4.

35. Singer A, Dutta S, Lewis E, Chen Z, Chen JC, Verma N, et al. Magnetoelectric Materials for Miniature, Wireless Neural Stimulation at Therapeutic Frequencies. Neuron. 2020;107(4):631-43.e5.

36. Peng D, Tong W, Collins DJ, Ibbotson MR, Prawer S, Stamp M. Mechanisms and Applications of Neuromodulation Using Surface Acoustic Waves—A Mini-Review. Frontiers in neuroscience. 2021;15.

37. Berggren M, Głowacki ED, Simon DT, Stavrinidou E, Tybrandt K. In Vivo Organic Bioelectronics for Neuromodulation. Chemical reviews. 2022;122(4):4826-46.

38. Duck FA, Starritt HC, ter Haar GR, Lunt MJ. Surface heating of diagnostic ultrasound transducers. The British journal of radiology. 1989;62(743):1005-13.

39. Calvert J, Duck FA. Self-heating of Diagnostic Ultrasound Transducers in Air and in Contact with Tissue Mimics. Ultrasound. 2006;14:100 - 8.

40. Fenno L, Yizhar O, Deisseroth K. The Development and Application of Optogenetics. Annual Review of Neuroscience. 2011;34(1):389-412.

41. Hüll K, Morstein J, Trauner D. In Vivo Photopharmacology. Chemical reviews. 2018;118(21):10710-47.

42. Kumar NM, Gilula NB. The gap junction communication channel. Cell. 1996;84(3):381-8.

43. Arimura N, Kaibuchi K. Neuronal polarity: from extracellular signals to intracellular mechanisms. Nature reviews Neuroscience. 2007;8(3):194-205.

44. Faber DS, Pereda AE. Two Forms of Electrical Transmission Between Neurons. Frontiers in Molecular Neuroscience. 2018;11.

45. Krapf D. Compartmentalization of the plasma membrane. Current opinion in cell biology. 2018;53:15-21.

46. Spector AA, Yorek MA. Membrane lipid composition and cellular function. Journal of Lipid Research. 1985;26(9):1015-35.

47. Created with BioRender.com.

48. Sperber GO. Coacervate-like membrane structures and olfactory transduction. Acta physiologica Scandinavica. 1977;99(2):129-39.

49. Alberts B, Johnson A, Lewis J, Raff M, Roberts K, Walter P. Molecular biology of the cell, 4th ed. New York: Garland Science/Taylor & Francis LLC. 2002.

50. Goldstein SA, Bockenhauer D, O'Kelly I, Zilberberg N. Potassium leak channels and the KCNK family of two-P-domain subunits. Nature reviews Neuroscience. 2001;2(3):175-84.

51. Li S, Wong AHC, Liu F. Ligand-gated ion channel interacting proteins and their role in neuroprotection. Frontiers in Cellular Neuroscience. 2014;8.

52. Haswell ES, Phillips R, Rees DC. Mechanosensitive channels: what can they do and how do they do it? Structure (London, England : 1993). 2011;19(10):1356-69.

53. Ernstrom GG, Chalfie M. Genetics of sensory mechanotransduction. Annual review of genetics. 2002;36:411-53.

54. Bezanilla F. How membrane proteins sense voltage. Nature reviews Molecular cell biology. 2008;9(4):323-32.

55. Bezanilla F. The voltage sensor in voltage-dependent ion channels. Physiological reviews. 2000;80(2):555-92.

56. Catterall WA. Ion channel voltage sensors: structure, function, and pathophysiology. Neuron. 2010;67(6):915-28.

57. Borys P, Grzywna ZJ. On the role of ball and chain interactions in recovery from the inactivation of the shaker potassium channel. Cellular & molecular biology letters. 2008;13(4):526-34.

58. Armstrong CM, Bezanilla F. Inactivation of the sodium channel. II. Gating current experiments. The Journal of general physiology. 1977;70(5):567-90.

59. Hodgkin AL, Huxley AF. A quantitative description of membrane current and its application to conduction and excitation in nerve. The Journal of physiology. 1952;117(4):500-44.

60. Chrysafides SM, Bordes S, Sharma S. Physiology, Resting Potential. StatPearls. Treasure Island (FL): StatPearls Publishing

Copyright © 2022, StatPearls Publishing LLC.; 2022.

61. Wright SH. Generation of resting membrane potential. Advances in physiology education. 2004;28(1-4):139-42.

62. Castro D, Sharma S. Hypokalemia. StatPearls. Treasure Island (FL): StatPearls Publishing

Copyright © 2022, StatPearls Publishing LLC.; 2022.

63. Hopkins PM. Skeletal muscle physiology. Continuing Education in Anaesthesia Critical Care & Pain. 2006;6(1):1-6.

64. Lewis R, Asplin KE, Bruce G, Dart C, Mobasheri A, Barrett-Jolley R. The role of the membrane potential in chondrocyte volume regulation. Journal of cellular physiology. 2011;226(11):2979-86.

65. Bean BP. The action potential in mammalian central neurons. Nature reviews Neuroscience. 2007;8(6):451-65.

66. Neher E, Sakmann B. Single-channel currents recorded from membrane of denervated frog muscle fibres. Nature. 1976;260(5554):799-802.

67. Priel A, Gil Z, Moy VT, Magleby KL, Silberberg SD. Ionic Requirements for Membrane-Glass Adhesion and Giga Seal Formation in Patch-Clamp Recording. Biophysical Journal. 2007;92(11):3893-900.

68. Hill CL, Stephens GJ. An Introduction to Patch Clamp Recording. In: Dallas M, Bell D, editors. Patch Clamp Electrophysiology: Methods and Protocols. New York, NY: Springer US; 2021. p. 1-19.

69. Cahalan M, Neher E. Patch clamp techniques: an overview. Methods in enzymology. 1992;207:3-14.

70. Adapted from “Patch-Clamp Techniques” and reprinted from “Patch-Clamp Recording Principle”, by BioRender.com (2022). Retrieved from app.biorender.com/biorender-templates.

71. Hamill OP, Marty A, Neher E, Sakmann B, Sigworth FJ. Improved patch-clamp techniques for high-resolution current recording from cells and cell-free membrane patches. Pflugers Archiv : European journal of physiology. 1981;391(2):85-100.

72. Brackenbury WJ. “Patch Clamp Electrophysiology Methods and Protocols,” Editors Mark Dallas and Damian Bell: Bioelectricity. June 2021;3(2):154-5. doi: 10.1089/bioe.2021.0015. Epub 2021 Jun 16.

73. Pijuan J, Barceló C, Moreno DF, Maiques O, Sisó P, Marti RM, et al. In vitro Cell Migration, Invasion, and Adhesion Assays: From Cell Imaging to Data Analysis. Frontiers in cell and developmental biology. 2019;7:107.

74. Balster RL. Drugs as chemical stimuli. Psychopharmacology series. 1988;4:1-11.

75. Greenbaum E, Evans BR. Synthetic Chromophores and Neural Stimulation of the Visual System. In: Dagnelie G, editor. Visual Prosthetics: Physiology, Bioengineering, Rehabilitation. Boston, MA: Springer US; 2011. p. 193-206.

76. Brown TD. Techniques for mechanical stimulation of cells in vitro: a review. Journal of Biomechanics. 2000;33(1):3-14.

77. Somjen D, Binderman I, Berger E, Harell A. Bone remodelling induced by physical stress is prostaglandin E2 mediated. Biochimica et Biophysica Acta (BBA) - General Subjects. 1980;627(1):91-100.

78. He L, Si G, Huang J, Samuel ADT, Perrimon N. Mechanical regulation of stem-cell differentiation by the stretch-activated Piezo channel. Nature. 2018;555(7694):103-6.

79. Prabhakaran MP, Ghasemi-Mobarakeh L, Jin G, Ramakrishna S. Electrospun conducting polymer nanofibers and electrical stimulation of nerve stem cells. Journal of bioscience and bioengineering. 2011;112(5):501-7.

80. Huang CP, Chen XM, Chen ZQ. Osteocyte: The impresario in the electrical stimulation for bone fracture healing. Medical Hypotheses. 2008;70(2):287-90.

81. Ercan B, Webster TJ. The effect of biphasic electrical stimulation on osteoblast function at anodized nanotubular titanium surfaces. Biomaterials. 2010;31(13):3684-93.

82. Stewart E, Kobayashi NR, Higgins MJ, Quigley AF, Jamali S, Moulton SE, et al. Electrical stimulation using conductive polymer polypyrrole promotes differentiation of human neural stem

cells: a biocompatible platform for translational neural tissue engineering. Tissue engineering Part C, Methods. 2015;21(4):385-93.

83. Balint R, Cassidy NJ, Cartmell SH. Electrical stimulation: a novel tool for tissue engineering. Tissue engineering Part B, Reviews. 2013;19(1):48-57.

84. Chen C, Bai X, Ding Y, Lee IS. Electrical stimulation as a novel tool for regulating cell behavior in tissue engineering. Biomaterials research. 2019;23:25.

85. Colic M, Stamenkovic D, Anzel I, Lojen G, Rudolf R. The influence of the microstructure of high noble gold-platinum dental alloys on their corrosion and biocompatibility in vitro. Gold Bulletin. 2009;42(1):34-47.

86. Hu G, Guan K, Lu L, Zhang J, Lu N, Guan Y. Engineered Functional Surfaces by Laser Microprocessing for Biomedical Applications. Engineering. 2018;4(6):822-30.

87. Babb TL, Kupfer W. Phagocytic and metabolic reactions to chronically implanted metal brain electrodes. Experimental neurology. 1984;86(2):171-82.

88. Spadaro JA, Becker RO. Function of implanted cathodes in electrode-induced bone growth. Medical and Biological Engineering and Computing. 1979;17(6):769-75.

89. Kristensen BW, Noraberg J, Thiébaud P, Koudelka-Hep M, Zimmer J. Biocompatibility of silicon-based arrays of electrodes coupled to organotypic hippocampal brain slice cultures. Brain research. 2001;896(1-2):1-17.

90. Hoogerwerf AC, Wise KD. A three-dimensional microelectrode array for chronic neural recording. IEEE Transactions on Biomedical Engineering. 1994;41(12):1136-46.

91. Amdursky N, Głowacki ED, Meredith P. Macroscale Biomolecular Electronics and Ionics. Advanced materials (Deerfield Beach, Fla). 2019;31(3):e1802221.

92. Cui X, Martin DC. Electrochemical deposition and characterization of poly(3,4-ethylenedioxythiophene) on neural microelectrode arrays. Sensors and Actuators B: Chemical. 2003;89(1):92-102.

93. Dauzon E, Mansour AE, Niazi MR, Munir R, Smilgies D-M, Sallenave X, et al. Conducting and Stretchable PEDOT:PSS Electrodes: Role of Additives on Self-Assembly, Morphology, and Transport. ACS Applied Materials & Interfaces. 2019;11(19):17570-82.

94. Uehara K, Takagishi K, Tanaka M. The Al/Indigo/Au photovoltaic cell. Solar Cells. 1987;22(4):295-301.

95. Pina J, Sarmento D, Accoto M, Gentili PL, Vaccaro L, Galvão A, et al. Excited-State Proton Transfer in Indigo. The journal of physical chemistry B. 2017;121(10):2308-18.

96. Pina J, Alnady M, Eckert A, Scherf U, Seixas de Melo JS. Alternating donor–acceptor indigo-cyclopentadithiophene copolymers: competition between excited state conformational relaxation, energy transfer and excited state proton transfer. Materials Chemistry Frontiers. 2018;2(2):281-90.

97. Jakešová M, Apaydin DH, Sytnyk M, Oppelt K, Heiss W, Sariciftci NS, et al. Hydrogen-Bonded Organic Semiconductors as Stable Photoelectrocatalysts for Efficient Hydrogen Peroxide Photosynthesis. Advanced Functional Materials. 2016;26(29):5248-54.

98. Merrill DR, Bikson M, Jefferys JG. Electrical stimulation of excitable tissue: design of efficacious and safe protocols. Journal of neuroscience methods. 2005;141(2):171-98.

99. Brown B. 5.04 - Tissue Impedance Spectroscopy and Impedance Imaging. In: Brahme A, editor. Comprehensive Biomedical Physics. Oxford: Elsevier; 2014. p. 73-90.

100. Peckham PH, Ackermann DM, Moss CW. Chapter II.5.12 - The Role of Biomaterials in Stimulating Bioelectrodes. In: Ratner BD, Hoffman AS, Schoen FJ, Lemons JE, editors. Biomaterials Science (Third Edition): Academic Press; 2013. p. 981-96.

101. Novikov SV. Rough electrode surface: effect on charge carrier injection and transport in organic devices. Macromolecular Symposia. 2004;212(1):191-200.

102. Mohapatra D, Parida S, Singh BK, Sutar DS. Importance of microstructure and interface in designing metal oxide nanocomposites for supercapacitor electrodes. Journal of Electroanalytical Chemistry. 2017;803:30-9.

103. Sytnyk M, Jakešová M, Litviňuková M, Mashkov O, Kriegner D, Stangl J, et al. Cellular interfaces with hydrogen-bonded organic semiconductor hierarchical nanocrystals. Nature communications. 2017;8(1):91.

104. Berggren M, Crispin X, Fabiano S, Jonsson MP, Simon DT, Stavrinidou E, et al. Ion Electron–Coupled Functionality in Materials and Devices Based on Conjugated Polymers. Advanced Materials. 2019;31(22):1805813.

105. Bianchi M, Carli S, Di Lauro M, Prato M, Murgia M, Fadiga L, et al. Scaling of capacitance of PEDOT:PSS: volume vs. area. Journal of Materials Chemistry C. 2020;8(32):11252-62.

106. Volkov AV, Wijeratne K, Mitraka E, Ail U, Zhao D, Tybrandt K, et al. Understanding the Capacitance of PEDOT:PSS. Advanced Functional Materials. 2017;27(28):1700329.

107. Voigt MB, Kral A. Cathodic-leading pulses are more effective than anodic-leading pulses in intracortical microstimulation of the auditory cortex. Journal of neural engineering. 2019;16(3):036002.

108. Hughes ML, Goehring JL, Baudhuin JL. Effects of Stimulus Polarity and Artifact Reduction Method on the Electrically Evoked Compound Action Potential. Ear and hearing. 2017;38(3):332-43.

109. Schoen I, Fromherz P. The Mechanism of Extracellular Stimulation of Nerve Cells on an Electrolyte-Oxide-Semiconductor Capacitor. Biophysical Journal. 2007;92(3):1096-111.

110. Salatino JW, Ludwig KA, Kozai TDY, Purcell EK. Glial responses to implanted electrodes in the brain. Nature biomedical engineering. 2017;1(11):862-77.

111. Jeong JW, Shin G, Park SI, Yu KJ, Xu L, Rogers JA. Soft materials in neuroengineering for hard problems in neuroscience. Neuron. 2015;86(1):175-86.

112. Lacour SP, Courtine G, Guck JR. Materials and technologies for soft implantable neuroprostheses. Nature Reviews Materials. 2016;1:16063.

113. Grill WM, Norman SE, Bellamkonda RV. Implanted Neural Interfaces: Biochallenges and Engineered Solutions. Annual Review of Biomedical Engineering. 2009;11(1):1-24.

114. Tsai SR, Hamblin MR. Biological effects and medical applications of infrared radiation. Journal of photochemistry and photobiology B, Biology. 2017;170:197-207.

115. Yao J, Liu B, Qin F. Rapid Temperature Jump by Infrared Diode Laser Irradiation for Patch-Clamp Studies. Biophysical Journal. 2009;96(9):3611-9.

116. Shapiro MG, Homma K, Villarreal S, Richter C-P, Bezanilla F. Infrared light excites cells by changing their electrical capacitance. Nature communications. 2012;3(1):736.

117. Passarella S, Karu T. Absorption of monochromatic and narrow band radiation in the visible and near IR by both mitochondrial and non-mitochondrial photoacceptors results in photobiomodulation. Journal of photochemistry and photobiology B, Biology. 2014;140:344-58.

118. Deisseroth K. Optogenetics. Nature Methods. 2011;8(1):26-9.

119. Nagel G, Szellas T, Huhn W, Kateriya S, Adeishvili N, Berthold P, et al. Channelrhodopsin-2, a directly light-gated cation-selective membrane channel. Proceedings of the National Academy of Sciences of the United States of America. 2003;100(24):13940-5.

120. Boyden ES, Zhang F, Bamberg E, Nagel G, Deisseroth K. Millisecond-timescale, genetically targeted optical control of neural activity. Nature neuroscience. 2005;8(9):1263-8.

121. Velema WA, Szymanski W, Feringa BL. Photopharmacology: Beyond Proof of Principle. Journal of the American Chemical Society. 2014;136(6):2178-91.

122. Wöhrle D, Meissner D. Organic Solar Cells. Advanced Materials. 1991;3(3):129-38.

123. Hoppe H, Sariciftci NS. Organic solar cells: An overview. Journal of Materials Research. 2004;19(7):1924-45.

124. Peumans P, Yakimov A, Forrest SR. Small molecular weight organic thin-film photodetectors and solar cells. Journal of Applied Physics. 2003;93(7):3693-723.

125. Yu G, Heeger AJ. Charge separation and photovoltaic conversion in polymer composites with internal donor/acceptor heterojunctions. Journal of Applied Physics. 1995;78(7):4510-5.

126. Halls JJM, Walsh CA, Greenham NC, Marseglia EA, Friend RH, Moratti SC, et al. Efficient photodiodes from interpenetrating polymer networks. Nature. 1995;376(6540):498-500.

127. Granström M, Petritsch K, Arias AC, Lux A, Andersson MR, Friend RH. Laminated fabrication of polymeric photovoltaic diodes. Nature. 1998;395(6699):257-60.

128. Tang CW. Two-layer organic photovoltaic cell. Applied Physics Letters. 1986;48(2):183-5.

129. Masahiro H, Yasuhisa K, Masaaki Y. Doping Effect on the Two-layer Organic Solar Cell. Chemistry Letters. 1990;19(1):119-22.

130. Pfeiffer M, Beyer A, Plönnigs B, Nollau A, Fritz T, Leo K, et al. Controlled p-doping of pigment layers by cosublimation: Basic mechanisms and implications for their use in organic photovoltaic cells. Solar Energy Materials and Solar Cells. 2000;63(1):83-99.

131. Drechsel J, Männig B, Kozlowski F, Gebeyehu D, Werner A, Koch M, et al. High efficiency organic solar cells based on single or multiple PIN structures. Thin Solid Films. 2004;451-452:515-7.

132. Dimitrakopoulos CD, Mascaro DJ. Organic thin-film transistors: A review of recent advances. IBM Journal of Research and Development. 2001;45(1):11-27.

133. Kerp HR, Donker H, Koehorst RBM, Schaafsma TJ, van Faassen EE. Exciton transport in organic dye layers for photovoltaic applications. Chemical Physics Letters. 1998;298(4):302-8.

134. Haugeneder A, Neges M, Kallinger C, Spirkl W, Lemmer U, Feldmann J, et al. Exciton diffusion and dissociation in conjugated polymer/fullerene blends and heterostructures. Physical Review B. 1999;59(23):15346-51.

135. Gregg BA, Hanna MC. Comparing organic to inorganic photovoltaic cells: Theory, experiment, and simulation. Journal of Applied Physics. 2003;93(6):3605-14.

136. Rand D, Jakešová M, Lubin G, Vėbraitė I, David-Pur M, Đerek V, et al. Direct Electrical Neurostimulation with Organic Pigment Photocapacitors. Advanced Materials. 2018;30(25):1707292.

137. Jakešová M, Silverå Ejneby M, Đerek V, Schmidt T, Gryszel M, Brask J, et al. Optoelectronic control of single cells using organic photocapacitors. Science Advances. 2019;5(4):eaav5265.

138. Đerek V, Rand D, Migliaccio L, Hanein Y, Głowacki ED. Untangling Photofaradaic and Photocapacitive Effects in Organic Optoelectronic Stimulation Devices. Frontiers in bioengineering and biotechnology. 2020;8:284.

139. Schoen I, Fromherz P. Activation of Na+ channels in cell membrane by capacitive stimulation with silicon chip. Applied Physics Letters. 2005;87(19):193901.

140. Schoen I, Fromherz P. Extracellular stimulation of mammalian neurons through repetitive activation of Na+ channels by weak capacitive currents on a silicon chip. Journal of neurophysiology. 2008;100(1):346-57.

141. Carvalho-de-Souza JL, Treger JS, Dang B, Kent SB, Pepperberg DR, Bezanilla F. Photosensitivity of neurons enabled by cell-targeted gold nanoparticles. Neuron. 2015;86(1):207-17.

142. Martino N, Feyen P, Porro M, Bossio C, Zucchetti E, Ghezzi D, et al. Photothermal cellular stimulation in functional bio-polymer interfaces. Scientific reports. 2015;5:8911.

143. Jiang Y, Carvalho-de-Souza JL, Wong RCS, Luo Z, Isheim D, Zuo X, et al. Heterogeneous silicon mesostructures for lipid-supported bioelectric interfaces. Nature Materials. 2016;15(9):1023-30.

144. Pinto B, Bassetto Jr CAZ, Latorre R, Bezanilla F. Measuring Temperature Time Course using Membrane Capacitance. Biophysical Journal. 2021;120(3, Supplement 1):240a.

145. Taylor RE. Impedance of the squid axon membrane. Journal of Cellular and Comparative Physiology. 1965;66(S2):21-5.

146. Plaksin M, Kimmel E, Shoham S. Correspondence: Revisiting the theoretical cell membrane thermal capacitance response. Nature communications. 2017;8(1):1431.

147. Shapiro MG, Homma K, Villarreal S, Richter C-P, Bezanilla F. Correspondence: Reply to 'Revisiting the theoretical cell membrane thermal capacitance response'. Nature communications [Internet]. 2017 2017/11//; 8(1):[1432 p.].

148. Plaksin M, Shapira E, Kimmel E, Shoham S. Thermal Transients Excite Neurons through Universal Intramembrane Mechanoelectrical Effects. Physical Review X. 2018;8(1):011043.

149. Szekely P, Dvir T, Asor R, Resh R, Steiner A, Szekely O, et al. Effect of Temperature on the Structure of Charged Membranes. The Journal of Physical Chemistry B. 2011;115(49):14501-6.

150. Petrache HI, Dodd SW, Brown MF. Area per Lipid and Acyl Length Distributions in Fluid Phosphatidylcholines Determined by 2H NMR Spectroscopy. Biophysical Journal. 2000;79(6):3172-92.

151. Pinto BI, Bassetto CAZ, Jr., Bezanilla F. Optocapacitance: physical basis and its application. Biophysical reviews. 2022;14(2):569-77.

152. Maingret F, Lauritzen I, Patel AJ, Heurteaux C, Reyes R, Lesage F, et al. TREK-1 is a heat-activated background K+ channel. The EMBO Journal. 2000;19(11):2483-91.

153. Daleke DL, Huestis WH. Incorporation and translocation of aminophospholipids in human erythrocytes. Biochemistry. 1985;24(20):5406-16.

154. Seigneuret M, Devaux PF. ATP-dependent asymmetric distribution of spin-labeled phospholipids in the erythrocyte membrane: relation to shape changes. Proceedings of the National Academy of Sciences. 1984;81(12):3751-5.

155. Ma Y, Poole K, Goyette J, Gaus K. Introducing Membrane Charge and Membrane Potential to T Cell Signaling. Frontiers in immunology. 2017;8:1513.

156. Sytnyk M, Głowacki ED, Yakunin S, Voss G, Schöfberger W, Kriegner D, et al. Hydrogen-Bonded Organic Semiconductor Micro- And Nanocrystals: From Colloidal Syntheses to (Opto-)Electronic Devices. Journal of the American Chemical Society. 2014;136(47):16522-32.

157. Schindelin J, Arganda-Carreras I, Frise E, Kaynig V, Longair M, Pietzsch T, et al. Fiji: an open-source platform for biological-image analysis. Nature Methods. 2012;9(7):676-82.

158. Longair MH, Baker DA, Armstrong JD. Simple Neurite Tracer: open source software for reconstruction, visualization and analysis of neuronal processes. Bioinformatics. 2011;27(17):2453-4.

159. Stilianu C. Experimental Setup for Laser Induced Single Cell Electrophysiological Recordings with Organic Semiconductors. TUGraz DIGITAL Library. 2020(Master Thesis).

160. Tiapko O, Shrestha N, Lindinger S, Guedes de la Cruz G, Graziani A, Klec C, et al. Lipid-independent control of endothelial and neuronal TRPC3 channels by light. Chemical Science. 2019;10(9):2837-42.

161. Wells J, Kao C, Konrad P, Milner T, Kim J, Mahadevan-Jansen A, et al. Biophysical mechanisms of transient optical stimulation of peripheral nerve. Biophys J. 2007;93(7):2567-80.

162. Jenkins MW, Wang YT, Doughman YQ, Watanabe M, Cheng Y, Rollins AM. Optical pacing of the adult rabbit heart. Biomedical optics express. 2013;4(9):1626-35.

163. Izzo AD, Richter C-P, Jansen ED, Walsh Jr. JT. Laser stimulation of the auditory nerve. Lasers in Surgery and Medicine. 2006;38(8):745-53.

164. Parameswaran R, Carvalho-de-Souza JL, Jiang Y, Burke MJ, Zimmerman JF, Koehler K, et al. Photoelectrochemical modulation of neuronal activity with free-standing coaxial silicon nanowires. Nature nanotechnology. 2018;13(3):260-6.

165. Starovoytov A, Choi J, Seung HS. Light-directed electrical stimulation of neurons cultured on silicon wafers. Journal of neurophysiology. 2005;93(2):1090-8.

166. Goda Y, Colicos MA. Photoconductive stimulation of neurons cultured on silicon wafers. Nature protocols. 2006;1(1):461-7.

167. Wang Y, Garg R, Hartung JE, Goad A, Patel DA, Vitale F, et al. Ti3C2Tx MXene Flakes for Optical Control of Neuronal Electrical Activity. ACS Nano. 2021;15(9):14662-71.

168. Rastogi SK, Garg R, Scopelliti MG, Pinto BI, Hartung JE, Kim S, et al. Remote nongenetic optical modulation of neuronal activity using fuzzy graphene. Proceedings of the National Academy of Sciences. 2020;117(24):13339-49.

169. Ghezzi D, Antognazza MR, Dal Maschio M, Lanzarini E, Benfenati F, Lanzani G. A hybrid bioorganic interface for neuronal photoactivation. Nature communications. 2011;2(1):166.

170. Wu F, Stark E, Ku P-C, Wise Kensall D, Buzsáki G, Yoon E. Monolithically Integrated µLEDs on Silicon Neural Probes for High-Resolution Optogenetic Studies in Behaving Animals. Neuron. 2015;88(6):1136-48.

171. Gutruf P, Yin RT, Lee KB, Ausra J, Brennan JA, Qiao Y, et al. Wireless, battery-free, fully implantable multimodal and multisite pacemakers for applications in small animal models. Nature communications. 2019;10(1):5742.

172. Mullick Chowdhury S, Lalwani G, Zhang K, Yang JY, Neville K, Sitharaman B. Cell specific cytotoxicity and uptake of graphene nanoribbons. Biomaterials. 2013;34(1):283-93.

173. Li Z, Yang R, Yu M, Bai F, Li C, Wang ZL. Cellular Level Biocompatibility and Biosafety of ZnO Nanowires. The Journal of Physical Chemistry C. 2008;112(51):20114-7.

174. Talukdar Y, Rashkow J, Lalwani G, Kanakia S, Sitharaman B. The effects of graphene nanostructures on mesenchymal stem cells. Biomaterials. 2014;35(18):4863-77.

175. Zhang F, Wang LP, Brauner M, Liewald JF, Kay K, Watzke N, et al. Multimodal fast optical interrogation of neural circuitry. Nature. 2007;446(7136):633-9.

176. Klapoetke NC, Murata Y, Kim SS, Pulver SR, Birdsey-Benson A, Cho YK, et al. Independent optical excitation of distinct neural populations. Nat Methods. 2014;11(3):338-46.

177. Bernstein JG, Garrity PA, Boyden ES. Optogenetics and thermogenetics: technologies for controlling the activity of targeted cells within intact neural circuits. Current opinion in neurobiology. 2012;22(1):61-71.

178. Kitamoto T. Conditional modification of behavior in Drosophila by targeted expression of a temperature-sensitive shibire allele in defined neurons. Journal of neurobiology. 2001;47(2):81-92.

179. Bischof H, Burgstaller S, Springer A, Matt L, Rauter T, Bachkönig OA, et al. Potassium ions promote hexokinase-II dependent glycolysis. iScience. 2021;24(4):102346.

180. Srivastava SB, Melikov R, Yildiz E, Han M, Sahin A, Nizamoglu S. Efficient photocapacitors via ternary hybrid photovoltaic optimization for photostimulation of neurons. Biomedical optics express. 2020;11(9):5237-48.

181. Srivastava SB, Melikov R, Yildiz E, Dikbas UM, Sadeghi S, Kavakli IH, et al. Bulk-heterojunction photocapacitors with high open-circuit voltage for low light intensity photostimulation of neurons. Journal of Materials Chemistry C. 2021;9(5):1755-63.

182. Gautam V, Rand D, Hanein Y, Narayan KS. A polymer optoelectronic interface provides visual cues to a blind retina. Advanced materials (Deerfield Beach, Fla). 2014;26(11):1751-6.

183. Ghezzi D, Antognazza MR, Maccarone R, Bellani S, Lanzarini E, Martino N, et al. A polymer optoelectronic interface restores light sensitivity in blind rat retinas. Nature photonics. 2013;7(5):400-6.

184. Maya-Vetencourt JF, Manfredi G, Mete M, Colombo E, Bramini M, Di Marco S, et al. Subretinally injected semiconducting polymer nanoparticles rescue vision in a rat model of retinal dystrophy. Nature nanotechnology. 2020;15(8):698-708.

185. Palanker D, Głowacki ED, Ghezzi D. Questions about the role of P3HT nanoparticles in retinal stimulation. Nature nanotechnology. 2021;16(12):1330-2.

186. Jiang Y, Parameswaran R, Li X, Carvalho-de-Souza JL, Gao X, Meng L, et al. Nongenetic optical neuromodulation with silicon-based materials. Nature protocols. 2019;14(5):1339-76.

187. Paltrinieri T, Bondi L, Đerek V, Fraboni B, Głowacki ED, Cramer T. Understanding Photocapacitive and Photofaradaic Processes in Organic Semiconductor Photoelectrodes for Optobioelectronics. Advanced Functional Materials. 2021;31(16):2010116.

188. Silverå Ejneby M, Jakešová M, Ferrero JJ, Migliaccio L, Sahalianov I, Zhao Z, et al. Chronic electrical stimulation of peripheral nerves via deep-red light transduced by an implanted organic photocapacitor. Nature biomedical engineering. 2022;6(6):741-53.

189. Missey F, Botzanowski B, Migliaccio L, Acerbo E, Głowacki ED, Williamson A. Organic electrolytic photocapacitors for stimulation of the mouse somatosensory cortex. Journal of neural engineering. 2021;18(6).

190. Missey F, Donahue MJ, Weber P, Ngom I, Acerbo E, Botzanowski B, et al. Laser-Driven Wireless Deep Brain Stimulation using Temporal Interference and Organic Electrolytic Photocapacitors. Advanced Functional Materials.n/a(n/a):2200691.

8 Appendix

2022 **Light Stimulation of Neurons on Organic Photocapacitors Induces Action Potentials with Millisecond Precision**

Tony Schmidt[1,2], Marie Jakešová[3,4], Vedran Đerek[4,5], Karin Kornmueller[1,2], Oleksandra Tiapko[1], Helmut Bischof[6,7], Sandra Burgstaller[6,7,8], Linda Waldherr[1], Marta Nowakowska[9], Christian Baumgartner[2,10], Muammer Üçal[2,9], Gerd Leitinger[2,11], Susanne Scheruebel[1], Silke Patz[9], Roland Malli[2,6], Eric Daniel Głowacki[3,4]*, Theresa Rienmüller[2,10]*, Rainer Schindl[1,2]*

ADV MATER TECHNOL-US. 2022; 2101159 Doi: 10.1002/admt.202101159

[1] Gottfried Schatz Research Center, Chair of Biophysics, Medical University of Graz, Neue Stiftingtalstraße 6, 8010 Graz, Austria
[2] BioTechMed-Graz, Graz, Austria
[3] Bioelectronics Materials and Devices Laboratory, Central European Institute of Technology, Brno University of Technology, Purkyňova 123, 61200 Brno, Czech Republic
[4] Laboratory of Organic Electronics, ITN Campus Norrköping, Linköping University, SE-60174, Norrköping, Sweden
[5] Department of Physics, Faculty of Science, University of Zagreb, Bijenička c. 32, 10000 Zagreb, Croatia
[6] Gottfried Schatz Research Center, Molecular Biology and Biochemistry, Medical University of Graz, Neue Stiftingtalstraße 6/6, 8010 Graz, Austria
[7] Department of Pharmacology, Toxicology and Clinical Pharmacy, Institute of Pharmacy, University of Tuebingen, Auf der Morgenstelle 8, 72076 Tuebingen, Germany
[8] NMI Natural and Medical Sciences Institute at the University of Tuebingen, 72770 Reutlingen,
[9] Research Unit of Experimental Neurotraumatology, Department of Neurosurgery, Medical University Graz, Auenbruggerplatz 2.2, 8036, Graz, Austria
[10] Institute of Health Care Engineering with European Testing Center of Medical Devices, Graz University of Technology, Graz, Austria.
[11] Gottfried Schatz Research Center, Division of Cell Biology, Histology and Embryology, Medical University of Graz, Neue Stiftingtalstraße 6, 8010 Graz, Austria